UNIVERSITY OF CALIFORNIA, MERCED

SNOW DISTRIBUTION OVER AN ELEVATION GRADIENT AND FOREST SNOW HYDROLOGY OF THE SOUTHERN SIERRA NEVADA, CALIFORNIA

A dissertation submitted in partial fulfillment of the requirements
for the degree of Doctor of Philosophy

by

Peter Bernard Kirchner

in

Environmental Systems
School of Engineering

2013

Committee:
Professor Roger C. Bales, Chair
Professor Martha H. Conklin
Professor Michael L. Goulden
Professor Thomas C. Harmon

The Dissertation of Peter Bernard Kirchner is approved, and it is acceptable in quality and form for publication on microfilm and electronically:

_____

Roger C. Bales, Chair

_____

Martha H. Conklin

_____

Michael L. Goulden

_____

Thomas C. Harmon

University of California, Merced

2013

DEDICATION

This work is dedicated to my father Bernard Joseph Kirchner who deferred his dream of scholarship at Cal-Tech to stay home and help support his mother, father, sisters and brothers through difficult times.

ABSTRACT

The Mountain West region of the United States is highly dependent on the ecosystem services from the mountain snowpack, one of the most vulnerable components of earth's fresh water cycle. The growing demand for fresh water in a period of climatic non-stationarity requires new approaches to monitoring and prediction. We investigate snow distribution and its effect on subsurface water storage in the southern Sierra Nevada, California using the combination of in-situ measurements, airborne LiDAR-snow-depth altimetry, satellite snow-cover maps, and novel spatial analysis. Using these data and methods we address questions about the mountain snowpack pertaining to: i) broad-scale distribution of snow accumulation governed by elevation and topography, ii) the effects of forest canopy on snow accumulation and ablation, at multiple scales, and iii) the partitioning of water in the vadose zone after snowmelt. Our results show that snow depth as a function of elevation increased at a rate of approximately 15 cm 100 m^{-1} until reaching an elevation of 3300 m where depth sharply decreased at a rate of 48 cm 100 m^{-1}. Departures from this trend were mostly negative below 2050 m, mostly positive between 2050-3300 m and negative above 3300 m, and attributed to orographic processes, mean freezing level, slope, terrain orientation and wind redistribution. High point-density LiDAR measured 31-44 % of under-canopy area, where snow depth was12-24 % lower than in the open, depending on forest vegetation type. The metrics of mean canopy height, canopy-to-ground surface ratio, fractional canopy cover, and canopy-height standard deviation individually explained half 45-58 % of the storm accumulation variability. Sky view factor explained up to 87 % of the variability in snow ablation rates in the cloudiest snow-melt seasons and direct beam solar irradiance explained up to 58 % in the clearest. The timing of soil dry-down is relatively uniform, but due to the heterogeneity of snowmelt it's timing is offset by up to 4 weeks at the same elevation depending on location. Baseflow and evapotranspiration continue after soil dry down has reached a plateau, suggesting that water is drawn from soil saprolite and saprock at depths >1 m below the surface.

ACKNOWLEDGEMENTS

Research presented in this dissertation was supported by the National Science Foundation through the Southern Sierra Critical Zone Observatory grant (EAR-0725097) and grants (EAR-1141764, EAR-1032295, EAR 0922307), a fellowship from the Southern California Edison Company and a seed grant through the Lawrence Livermore National Laboratory (6766). Supplemental support was also provided through NASA (NNX-10A097G).

Comments from Noah Molotch, Qinghua Guo, Cliff Riebe, Juan Fernandez Diaz and Thomas Harmon have been very helpful in improving these manuscripts. I also wish to acknowledge the field and technical assistance from Matt Cooper, Robert Rice, Brandi McKuin, Xiande Meng, Josh O'Rourke, Ruth Xochihua, Stephane Tanverakul, Adrian Rojas, Sean Kelly, Matt Meadows, Keith Musselman, Ryan Lucas, Jacob Flanagan, Otto Alvarez and many other UC Merced students and staff that tirelessly participated in the construction maintenance and data collection associated with the Wolverton CZO.

I thank my advisor Roger Bales for his faith in my abilities, patience with my curiosity and providing his time and perseverance to guide me. I also gratefully acknowledge the time and diligence of my committee members: Thomas Harmon, Martha Conklin and Michael Goulden.

I am very thankful for the friendship, encouragement and guidance I have received from Thomas Painter, Sylvain Masclin, Glenn Shaw, Fengjing Liu, Anthony Westerling, Naoko Kada, Yihsu Chen, Ruby Chen, Jill Giles, Don Rubien, Brad Rassler, Tim Kirchner, Bob Rice, Sandra Villamizar, Henry Pai, Jim Roche, Max Vladymyrov, Sandra Steaples, Tatiana Stewart, Doug Stewart, Nancy Corzini, Katherine Allen, David Herbst and many others. Special thanks to: Philip Deutschle who, when I was 13, encouraged my interest in science and Jim Sickman for sharing his wisdom, knowledge, and kindness.

Most of all I wish to thank Elsita and Markus Kirchner, my loving family, whom I have depended upon for support, laughter and so much more.

CURRICULUM VITAE

Peter B. Kirchner
Research Associate
Joint Institute for Regional Earth System Science and Engineering
University of California, Los Angeles
Jet Propulsion Laboratory
4800 Oak Grove Drive, Pasadena California 91109
phone: (209) 834-7628 m
email: Peter.B.Kirchner@jpl.nasa.gov

EDUCATION

Ph.D.

Environmental Systems, School of Engineering, University of California, Merced, expected 2013, Advisor Roger Bales, Dissertation: Snow distribution over an elevation gradient and forest snow hydrology of the southern Sierra Nevada, California

M.S.

Geography, Mackay School of Earth Sciences and Engineering, University of Nevada, Reno, Advisor Franco Biondi, Thesis: Trace Metals in Tree-Rings of the Tahoe Basin

B.S.

Zoology, Foci: Ecology and Evolution, School of Agriculture and Environmental Sciences, University of California, Davis, Minor: Art Studio

RESEARCH INTERESTS

Bridging the spatial and temporal relationships between hydrologic, ecologic, and biogeochemical processes in mountain environments through the integration of in-situ and remote sensing observations.

PUBLICATIONS

Peer-reviewed

2013

A. Harpold, Q. Guo, N. Molotch, P. Brooks**,** R. Bales, J. Fernandez-Diaz, K. Musselman, T. Swetnam, **P. Kirchner,** M. Meadows, J. Flanagan, R. Lucas; *LiDAR Derived Snowpack Datasets From Mixed Conifer Forests Across the Western U.S.,* Water Resources Research (2013) *in review*

2012

K. Musselman, N. Molotch, S. Margulis, **P. Kirchner,** R. Bales; *Relationships between conifer forest structure and snowmelt dynamics inferred from in-situ observations, hemispherical photographs and canopy radiative transfer,* Agricultural and Forest Meteorology (2012) 161:46-56

2011

R. Bales, J. Hopmans, T. O'Geen, M. Meadows, P. Hartsough, **P. Kirchner,** C. Hunsaker, D. Beaudette; *Soil Moisture Response to Snowmelt and Rainfall in a Sierra Nevada Mixed-Conifer Forest* Vadose Zone Journal (2011) 10:786-799

2008

P. Kirchner, F. Biondi, J. McConnell, R. Edwards**;** *Variability of trace metal concentrations in Jeffrey pine (Pinus jeffreyi) tree rings from the Tahoe Basin, California, USA,* Journal of Forest Research (2008) 13:347–356

2006

M.S. Thesis **P. Kirchner,** *Tree Rings and Archived Trace Metals in the Tahoe Basin,* University of Nevada, Reno (2006) 131pp.

Manuscripts in preparation

P. Kirchner, R. Bales, N. Molotch, J. Flanagan, Q. Guo *Seasonal snow accumulation over an elevation gradient in the Southern Sierra Nevada, California*

A. Harpold, N. Molotch, K. Musselman, R. Bales, **P. Kirchner,** M. Litvak,and P. Brooks, *Snowmelt Infiltration in Mixed-Conifer Subalpine Forests*

P. Kirchner, R. Bales, K. Musselman, N. Molotch, *Under-canopy snow accumulation and melt in Sierra Nevada Forests*

P. Kirchner, J. Roche, T. Ghezzehei, R. Bales, *Rapid snowmelt in a subalpine catchment, using temperature as a tracer for flood response in mountain streams*

J. Blankinship, **P. Kirchner,** S. Hart, *Nitrogen cycling response to fine scale temperature and moisture gradients in sub-alpine forest ecosystems*

INVITED LECTURES

2013

Measuring Sierra Snow From the Air, Sequoia Speaks, United States National Park Service public lecture series, Visalia, California, February 23

2011

Resolving Snow Depth using Gridded LiDAR Data, Critical Zone Observatory LiDAR Acquisition Initiative and Workshop, Berkeley, California, December 4

Southern Sierra Nevada Mountain Front Precipitation Accumulation and Ablation Analyzed with Scanning LiDAR Snow Depth and In-Situ Instrumental Measurements, Yosemite Hydroclimate Meeting, California, October 6

Mountain catchments and Forest Snowcover: Measuring and Modeling Snowpack in the Southern Sierra Nevada, Sierra Nevada Research Institute Research Symposium, April 18

2008

Chemistry, discharge, and nutrient contribution of rock glaciers in the southern Sierra Nevada mountains of California, White Mountain Research Symposium, Climate Ecosystems and Resources in Eastern California, Bishop, California, November 5

SCIENTIFIC REVIEWS

Arctic Antarctic and Alpine Research, Fire Ecology

HONORS AND AWARDS

2010

- ○ Southern California Edison Fellowship for Mountain Hydrology Research
- ○ Thayer soil science scholarship
- ○ Nominated for full membership in Sigma Xi, The Scientific Research Society

2006

Outstanding Graduate Student of the Year, Department of Geography, Mackay School of Environmental Science and Engineering, University of Nevada, Reno

2004

Mountain Desert Research Scholarship, Department of Geography, University of Nevada, Reno

PROFESSIONAL ORGANIZATIONS

American Association for the Advancement of Science
American Association of Geographers
American Geophysical Union
Soil Science Society of America
Western Snow Conference

FOREIGN LANGUAGES

Spanish; proficient skill level in speaking, reading, and writing

SOFTWARE AND PROGRAMING

Statistical and analysis software; Arc GIS, R, Sigmaplot, Geo-Da, Golden Software Surfer Modeling software; Hydrus 1D, PHREQ, Mod-flow, ESAP, Net-Path Programming languages; Visual Basic, Python, R

SELECTED PROFESSIONAL EXPERIENCE

Research Scientist, Remote Sensing of Snow
Jan 2013-Present

Research associate, University of California, Los Angeles, Joint Institute for Regional Earth System Science and Engineering

- ○ Conducting calibration and validation of airborne light detection and ranging radar (LiDAR) and hyperspectral reflectance measurements of snow at the Jet Propulsion Laboratory for the Airborne Snow Observatory mission.

Field Research, Observatory Design and Construction
2006-2013

Graduate Research Scientist, University of California Merced, Sierra Nevada Research Institute, Critical Zone Observatory, NSF grant, P.I. Roger Bales

○ Facilitated construction of the Sequoia National Park Hydrologic Observatory and collection of continuous data from over 175 sensors deployed as an integrated network of sensors throughout a 7.5 km catchment
○ Assisted in the design, permitting and construction of additional SNRI Hydrologic Observatories and flux towers for the Critical Zone Observatory
○ Served as liaison between UC Merced, NPS, concessionaire, facilities personnel, researchers from other universities, and outside contractors on the use, operation, and maintenance of Sequoia Field Station.

2006

Research Associate, University of California Merced, Sierra Nevada Research Institute, Lawrence Livermore National Laboratory grant, P.I. Roger Bales
○ Began construction on prototype Hydrologic Observatory

2003-2006

Graduate Student Researcher Dendrolab, Department of Geography University of Nevada, Reno, Supervisor: Franco Biondi
○ Collected tree cores from remote locations of California and Nevada, for millennial time scale tree ring chronologies of the Great Basin and Sierra Nevada

2001-2002

Research Associate University of California, Davis, California and California Department of Fish and Game, Bishop, California, Supervisor: Curtis Milliron
○ Supervised two to four person field crews conducting amphibian monitoring and restoration in Sierra Nevada lakes and ponds

1995-2001

Research Assistant University of California, Santa Barbara, Institute for Computational Earth System Science and the Marine Sciences Institute, Eastern Sierra Natural Reserve System, worked on multiple grants, often concurrently, conducting scientific research with the following Principle Investigators: James Sickman, John Melack, Roland Knapp, Jeff Dozier, John Stoddard, Robert Jellison, Scott Cooper, Daniel Dawson, and David Herbst
○ Conducted remote sensing ground truth campaigns in the Sierra Nevada
○ Coordinated winter and spring snow hydrology field campaigns of snow and water isotope chemistry and geochemistry of high altitude lakes
○ Supervised field crews of two to eight individuals in remote locations, often days travel from the nearest road
○ Constructed, maintained remote weather stations, snow depth monitoring sensors, soil moisture sensors and hydrologic gauging stations
○ Regular snow and water sample collections from multiple locations
○ Planned logistics for multi-day field campaigns
○ Collected, identified, and analyzed population data for aquatic invertebrate and zooplankton of Sierra Nevada lakes and streams
○ Maintained Sierra Nevada Aquatic Research Laboratory meteorology data base
○ Captained research vessel for monthly limnology surveys of Mono Lake, California and research campaigns on Crowley Lake, California
○ Characterized soil types and plant communities in Sierra Nevada alpine ecosystems

Teaching

2003-2006

Graduate Student Instructor, Department of Geography, University of Nevada, Reno

Geography 103, ***Earth System Science*** (two semesters)

○ Lectured, taught laboratory sections and graded course assignments, anonymous teaching evaluation rating of 7.1/8, 40 students and 7.3/8, 30 students

Geography 418, ***Geographic Thought*** (upper division course, one semester)

○ Lectured, introduced assignments and graded course assignments, anonymous teaching evaluation rating of 6.9/8, 20 students

Geography 205, ***Geographic Information Systems*** (one semester)

○ Taught laboratory sections and graded course assignments, anonymous teaching evaluation rating of 6.9/8, 12 students

Leadership, Management, Project Planning

2009-2011

Representative, University of California, Merced Campus Budget Committee

○ Reviewed operational budgets of campus departments and units, created guidelines and made recommendations for distribution of annual funding

1990-2000

President, Birchim Community Services District, domestic water supply and fire protection services

○ Governed board of directors through monthly to biweekly public meetings

○ Planned, financed (USDA rural development) permitted (USDA Forest Service) and constructed community water distribution system

○ Created a long range financial and maintenance plan for water system

Instructor and Course Director, Pacific Crest and Loch Eil Outward Bound Schools, California, Oregon, Washington, Mexico and the United Kingdom

○ Taught wilderness based experiential education courses in the Western U.S. and abroad, focused on leadership, team building, and personal growth through community service projects and the mastery of outdoor pursuits (rock climbing, ice climbing, mountaineering, sea kayaking, wilderness first aid, and mountain, and desert backcountry travel)

○ Supervised two to four groups of two instructors with 10 students, established safety and course management policies and procedures, and contributed to writing course area guides for the Sequoia King's Canyon, Southern Yosemite region and Joshua Tree National Monument

Training Officer, Mono County Sheriff's Search and Rescue (SAR) Team, directed training and team preparation for professional and volunteer team members, and SAR volunteer

○ Coordinated training program and participated in > 70 search and rescue operations including: missing persons, high angle, swift water, downed aircraft, auto extraction in difficult terrain and winter SAR

○Participated in > 20 mutual aid agreement search and rescue flight operations with Air National Guard, California Highway Patrol, and Naval Air Station SAR

TABLE OF CONTENTS

TABLE OF CONTENTS

TABLE OF CONTENTS

TABLE OF CONTENTS

APPENDICES

LIST OF TABLES

LIST OF FIGURES

LIST OF FIGURES

LIST OF FIGURES

LIST OF FIGURES

LIST OF FIGURES

LIST OF FIGURES

CHAPTER 1

INTRODUCTION

1. Rationale

Mountain ecosystems provide much of the earth's usable fresh water and are important components of the regional water balance of mountain areas across the globe. These ecosystems face historic shifts in function due to the impacts of a warming climate combined with changes in land use patterns. Thus, knowledge of their function is critical. The Mountain West of the United States, and the Sierra Nevada in particular, has an emerging network of instrumental observatories and remote sensing platforms that, when combined, provide a unique opportunity for developing adaptive mitigation strategies to on-going shifts in ecosystem structure and hydrologic response.

Winter precipitation in the Mountain West predominantly falls as snow, and serves as a temporary storage reservoir of water and the main source of surface runoff and ground water recharge (Bales et al. 2006). In the Mediterranean, semi-arid climate of California's Sierra Nevada, wet winters are followed by a prolonged dry period, when the region is influenced by subtropical high pressure. Snow typically accumulates from November to March, followed by a one to three month snow-melt transition period that depends on altitude, snow water equivalent (SWE), and latitude (Peterson et al. 2008). Annual snowmelt meets approximately half of the regions fresh water demand, produces approximately half of the California's 37,000 gigawatt-hours of hydro-electricity, and sustains Sierra Nevada forests and downstream riparian ecosystems (Kattelmann et al. 1983, Guegan et al. 2012).

In forested ecosystems the effect of vegetation on the water cycle is significant and an important factor in the hydrology of the Sierra Nevada (Stephenson 1998). Trees in mountain environments mediate discharge and soil moisture by affecting the quantity and timing of snow that accumulates on the forest floor and the snowmelt infiltrating the soil. The dominant processes affecting snow accumulation in forests are interception,

sublimation, and alteration of the radiation budget of the snowpack by canopy (Hardy et al. 1997). In recent decades higher winter minimum temperatures have resulted in a one to four week shortening of the snowmelt period (Dettinger et al. 2004, Stewart et al. 2005). The resulting earlier runoff period and prolonged summer-dry-period of low soil moisture impact forest ecosystems through increased water stress. These changes in forest hydrology demonstrate the potential for irreversible changes in ecosystem structure and function (Trujillo et al. 2012, Diffenbaugh and Field 2013).

The Sierra Nevada is ideally oriented to intercept moisture-laden air masses coming from the Pacific Ocean. Orographic precipitation occurs through the fundamental principle of unsaturated air rising, expanding and cooling. As Pacific air masses move eastward, rise and become saturated as they ascend the west slopes of the Sierra Nevada precipitation increases with elevation (Roe 2005). The accumulating winter snowpack is further influenced by local topography and subsequently redistributed by wind and unequally ablated by radiative forcing and energy exchange with the atmosphere, ground and vegetation.

The effect of vegetation on snow accumulation is explained by:

$$SWE = SWE_o + \left(P_s - (I_s - U_l\right) + P_r - (I_r - R_d) - M)\, t \quad (1)$$

where, SWE at any point in time can be described by initial accumulation (SWE_o), precipitation from snow (P_s), and rain (P_r), minus net interception and melt (M) for a time-step (t) adapted from (Pomeroy et al. 2007, Ellis et al. 2010). Sublimation is snow that is intercepted minus unloaded or melted snow ($I_s - U_l$) and evaporation is intercepted rain minus rain that has dripped from the canopy ($I_r - R_d$). The efficiency with which snow is intercepted and subsequently lost through sublimation or evaporation is central to quantifying vegetation effects on the overall water balance in forested ecosystems (Pomeroy et al. 1998).

Snowmelt, soil moisture and surface discharge in the Sierra Nevada are tightly coupled temporally and spatially. In the spring, with increasing radiative energy, the snowpack becomes isothermal at 0° C and a diurnal cycle of melt-freeze ensues. Snow

melts through diel melt-freeze cycles of increasing frequency and duration until all of the snow is melted and has been partitioned to surface runoff or entered the subsurface through infiltration or macro-pore pathways. A change in the timing of the snowmelt has cascading effects on soil moisture, surface discharge and ecosystems processes at multiple time-scales (Weltzin et al. 2003).

Conceptually, the partitioning of snowmelt to soil water and vegetation are explained by:

$$\phi Z_R \frac{ds}{dt} = I_{swe} - ET - L - Q_s \tag{2}$$

where ϕ is effective soil porosity, Z_R is depth to regolith, I_{swe} is infiltration from snow melt, L is leakage through macropores, regolith or fractures, ET is a bulk term for evaporation and transpiration, Q_s is surface runoff, and s is soil-water storage (adapted from (Rodriguez-Iturbe 2000).

Snow distribution in the Sierra Nevada demonstrates variability at multiple scales. Scaling is intrinsically dependent on the phenomena we wish to observe and a central question in any discussion of temporal or spatial analysis (Kirchner 2006). If we wish to understand the hydrologic processes of a large watershed multiple methods and scaling are often required (Wilson and Guan 2004, Robinson et al. 2008). Emerging observation and instrumentation strategies now make it possible to investigate watershed hydrology at spatial and temporal scales appropriate to the focus of this research. The use of light detection and ranging radar (LiDAR) to measure ground snow and vegetation surfaces at centimeter accuracy provides direct observations for analysis from plot to watershed scales. Watershed observatories use strategically deployed instruments to study the links between landscape climate variability and water and material fluxes (Anderson et al. 2008). Current research using these methods include water-balance observations, manipulations and modeling to predict climate-change impacts and mitigation strategies for sustainable water yield (Bales et al. 2011, Lin et al. 2011).

2. Objectives

The purpose of this work is to address knowledge gaps in our understanding of Sierra Nevada snow cover in order to inform how we monitor and potentially mitigate climate-induced impacts on snow hydrology. Our current monitoring methods rely upon limited ground measurements, precipitation forecasts and statistically driven models that have limited predictive power in the increasingly common climatic extremes. There is an urgent need, and vast potential, for improvement in the monitoring and prediction of hydrologic conditions in the Sierra Nevada using the emerging tools and methods mentioned above. In the following chapters we use these tools to address three key questions:

1.) What is the broad-scale distribution of snow accumulation, as governed by the land-surface properties of elevation, azimuthal orientation, freezing level and prevailing winds in the southern Sierra Nevada? (Chapter 2 and appendices A and B).

2.) How does forest canopy mediate the processes of ablation and accumulation? (Chapter 3 and appendices C and D).

3.) How does snowmelt water delivery affect the shallow and deep vadose-zone processes of the forest hydrologic cycle? (Chapter 3 and appendices E and F)

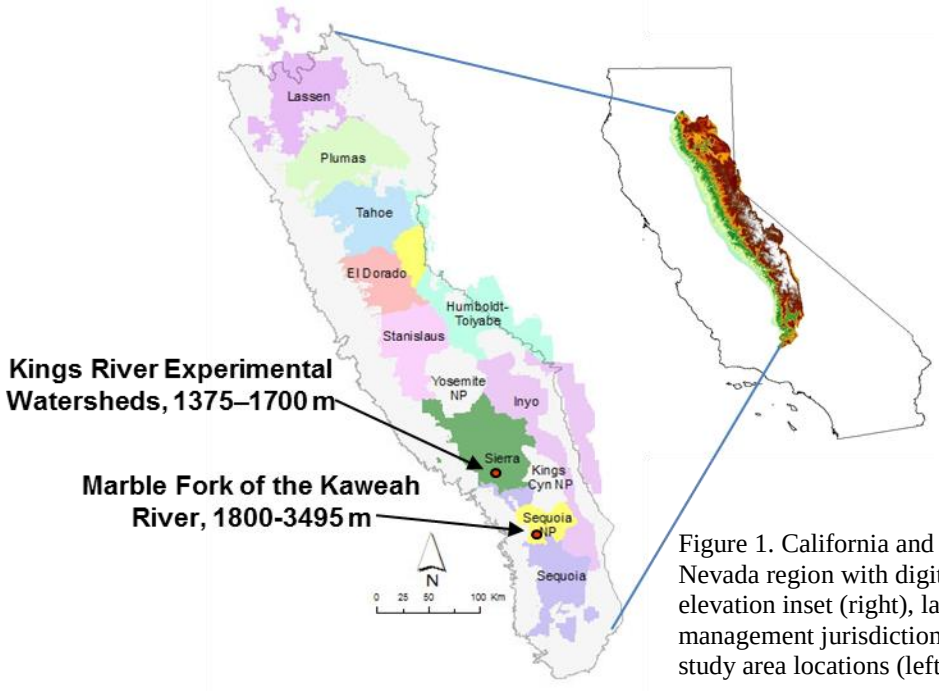

Figure 1. California and Sierra Nevada region with digital elevation inset (right), land management jurisdiction with study area locations (left).

3. Methods

Remote-sensing measurements of heterogeneous spatial features such as snow cover and forest canopy require calibration. Calibration at the appropriate density, granularity, and spatially appropriate distribution of measurements is a key problem (Blöschl 1999). Previous studies have successfully applied regression trees and geostatistical methods to define snow distribution variability by determining the spatial and temporal covariance (Jost et al. 2005, Molotch and Bales 2005). We approached this problem by blending physiographic data (e.g. LiDAR-generated digital surface models), large-scale surveys (e.g. vegetation maps), synoptic surveys and plot measurements. Our study areas are located in the southern Sierra Nevada, in the Marble Fork of the Kaweah River in Sequoia National Park and in the Kings River experimental watershed (Figure 1). Previous studies have successfully applied regression trees and geostatistical methods to define snow distribution variability by determining the spatial and temporal covariance

(Jost et al. 2005, Molotch and Bales 2005). To develop a process level understanding of snow accumulation and distribution we measured at the plot, catchment and watershed scales employing instrumental observations, models and two remote sensing platforms. We used the emerging field of LiDAR snow-depth retrievals to develop novel methods for evaluating snow accumulation under forest canopies and across an elevation gradient.

LiDAR data were collected, in the winter and summer of 2010, to determine snow depth across the study areas and these data were used to create 1-m grids of ground, canopy and snow surfaces that allowed an in depth spatial analysis. Synoptic surveys took place over a period of five years and measured snow depth, density and SWE each winter. Field locations were identified using a high-resolution global positioning system and entered into a geographic information system to facilitate spatial and temporal analysis (Schume et al. 2003, Jost et al. 2005). Study plots were selected by analyzing digital elevation models for representative areas of slope, aspect, vegetation type, proximity to existing instrumentation, and elevation. The sites represent slopes aspects and elevations where typical forest stand associations are found in the southern Sierra Nevada (Stephenson 1998) (appendix D).

Some of the instrument clusters installed and used for this study are part of the Critical Zone Observatory (CZO) and were located to capture the variability of the mesic, north, and xeric, south, aspects that represent the mean slope and aspect conditions of research catchments. CZO sites are instrumented to detect changes in snow depth and soil moisture in open areas and in relation to tree canopies (Anderson et al. 2008). Our instrumentation includes snow-depth sensors and time-domain-reflectometry to determine volumetric water content at up to four different depths in the soil profile (Allen et al. 2007, Flint et al. 2008, Robinson et al. 2008) (appendix F). The network also includes two meteorological stations recording temperature, relative humidity, wind speed and wind direction (appendix B). Continuous measurements for these data are collected using recording data loggers. These sites are also proximal to other monitoring networks that collect additional local long-term data from met stations, snow courses, snow pillows and depth sensors (Bales 2005, CDEC 2007). Long-term snow courses were also used to calibrate the data for the study period to the historical means.

References

Allen, M., V. Rodrigo, E. Grahm, W. Swensen, and M. Hamilton. 2007. Soil Sensor Technology Life Within a Pixel. Bio Science **57**.

Anderson, S. P., R. C. Bales, and C. J. Duffy. 2008. Critical Zone Observatories: Building a network to advance interdisciplinary study of Earth surface processes. Mineralogical Magazine **72**:7-10.

Bales, R., J. Battles, Y. Chen, M. H. Conklin, E. Holst, K. L. O'Hara, P. Saksa, and W. Stewart. 2011. Forests and Water in the Sierra Nevada: Sierra Nevada Watershed Ecosystem Enhancement Project. 11.1, Sierra Nevada Research Institute, Merced.

Bales, R. C. 2005. Integrated measurements and modeling of Sierra Nevada water budgets. Page 9. Funded proposal, Lawerance Livermore Laboratory.

Bales, R. C., N. P. Molotch, T. H. Painter, M. D. Dettinger, R. Rice, and J. Dozier. 2006. Mountain hydrology of the western United States. Water Resources Research **42**.

Blöschl, G. 1999. Scaling issues in snow hydrology. Hydrological Processes **13**:2149-2175.

CDEC. 2007. Historic snow sensor data. California Data Exchange Center.

Dettinger, M. D., D. R. Cayan, M. K. Meyer, and A. E. Jeton. 2004. Simulated hydrologic responses to climate variations and change in the Merced Carson and American River basins, Sierra Nevada, California, 1900-2099. Climatic Change **62**:1-35.

Diffenbaugh, N. S., and C. B. Field. 2013. Changes in Ecologically Critical Terrestrial Climate Conditions. Science **341**:486-492.

Ellis, C. R., J. W. Pomeroy, T. Brown, and J. MacDonald. 2010. Simulation of snow accumulation and melt in needleleaf forest environments. Hydrology and Earth System Sciences **14**:925-940.

Flint, A., L. Flint, and M. D. Dettinger. 2008. Modeling soil moisture processes and recharge under a melting snowpack. Vadose Zone Journal **7**: 251-266.

Guegan, M., K. Mandini, and C. Uvo. 2012. Climate Change Effects on the High-Elevation Hydropower System with Consideration of Warming Impacts on Electricity Demand and Pricing.

Hardy, J. P., R. E. Davis, R. Jordan, X. Li, C. Woodcock, W. Ni, and J. C. McKenzie. 1997. Snow ablation modeling at the stand scale in a boreal jack pine forest. Journal of Geophysical Research **102**:29397-29406.

Jost, G., G. B. M. Heuvelink, and A. Papritz. 2005. Analysing the space-time distribution of soil water storage of a forest ecosystem using spatio-temporal kriging. Geoderma **128**:258-273.

Kattelmann, R. C., N. H. Berg, and J. Rector. 1983. The potential for Increasing Streamflow from Sierra-Nevada Watersheds Water Resources Bulletin **19**:395-402.

Kirchner, J. W. 2006. Getting the right answers for the right reasons: Linking measurements, analyses, and models to advance the science of hydrology. Water Resources Research **42**.

Lin, H., J. W. Hopmans, and D. d. Richter. 2011. Interdisciplinary Sciences in a Global Network of Critical Zone Observatories. Vadose Zone Journal **10**:781-785.

Molotch, N. P., and R. C. Bales. 2005. Scaling snow observations from the point to the grid element: Implications for observation network design. Water Resources Research **41**.

Peterson, D., I. Stewart, and F. Murphy. 2008. Principle Hydrologic Responses to Climatic and Geologic Variability in the Sierra Nevada, California. San Francisco estuary & watershed science **6**.

Pomeroy, J. W., D. M. Gray, T. Brown, N. R. Hedstrom, W. L. Quinton, R. J. Granger, and S. K. Carey. 2007. The cold regions hydrological model: a platform for basing process representation and model structure on physical evidence. Hydrological Processes **21**:2650-2667.

Pomeroy, J. W., J. Parviainen, N. Hedstrom, and G. D. M. 1998. Coupled modelling of forest snow interception and sublimation. Hydrological Processes **12**:2317-2337.

Robinson, D. A., C. S. Campbell, J. W. Hopmans, B. K. Hornbuckle, S. B. Jones, R. Knight, F. Ogden, J. Selker, and O. Wendroth. 2008. Soil Moisture Measurement for Ecological and Hydrological Watershed-Scale Observatories: A Review. Vadose Zone Journal **7**:358-389.

Rodriguez-Iturbe, I. 2000. Ecohydrology: A hydrologic perspective of climate-soil-vegetation dynamics. Water Resources Research **36**:3-9.

Roe, G. H. 2005. Orographic precipitation. Pages 645-671 Annual Review of Earth and Planetary Sciences. Annual Reviews, Palo Alto.

Schume, H., G. Jost, and K. Katzensteiner. 2003. Spatio-temporal analysis of the soil water content in a mixed Norway spruce European beech stand. Geoderma **112**.

Stephenson, N. 1998. Actual evapotranspiration and deficit: biologically meaningful correlates of vegetation distribution across spatial scales. Journal of Biogeography **25**:855-870.

Stewart, I. T., D. R. Cayan, and M. D. Dettinger. 2005. Changes toward Earlier Stream flow Timing across Western North America. Journal of Climate **18**:1136-1155.

Trujillo, E., N. P. Molotch, M. L. Goulden, A. E. Kelly, and R. C. Bales. 2012. Elevation-dependent influence of snow accumulation on forest greening. Nature Geoscience **5**:705-709.

Weltzin, J. F., M. E. Loik, E. E. Small, and S. Schwinning. 2003. Assessing the Response of Terrestrial Ecosystems to Potential Changes in Precipitation. Bio Science **53**.

Wilson, J. L., and H. Guan. 2004. Mountain-Block Hydrology and Mountain-Front Recharge.*in* F. M. Phillips, J. Hogan, and B. Scanlon, editors. Groundwater Recharge in A Desert Environment: The Southwestern United States. American Geophysical Union, Washington DC

CHAPTER 2

SEASONAL SNOW ACCUMULATION OVER AN ELEVATION GRADIENT IN THE SOUTHERN SIERRA NEVADA, CALIFORNIA

Peter B. Kirchner, Sierra Nevada Research Institute, UC Merced, Merced, CA and Joint Institute for Regional Earth System Science and Engineering, UC Los Angeles, CA[a]

Roger C. Bales, Sierra Nevada Research Institute, UC Merced, Merced, CA

Jacob Flanagan, Sierra Nevada Research Institute, UC Merced, Merced, CA

Noah P. Molotch, Department of Geography and the Institute of Arctic and Alpine Research, University of Colorado at Boulder, Boulder, CO and Jet Propulsion Laboratory, California Institute of Technology, Pasadena, CA

Qinghua Guo, Sierra Nevada Research Institute, UC Merced, Merced, CA

[a]Contact information for corresponding author:
Peter B. Kirchner
Jet Propulsion Laboratory Pasadena, CA 95343
209-834-7628
Peter.B.Kirchner@jpl.nasa.gov
keywords: snow, LiDAR, SWE, hydrology, water resources, elevation gradient, Sierra Nevada

Abstract

We present results and analysis from snow on and snow off airborne scanning LiDAR measurements over a 53.1 km^2 area and 1850-3495 m elevation range in the southern Sierra Nevada. We found that snow depth as a function of elevation alone increased at a rate of approximately 15 cm 100 m^{-1}, with short length-scale departures, until reaching an elevation of 3300 m where depth sharply decreased at a rate of 48 cm 100 m^{-1}. Departures from the 15 cm 100 m^{-1} trend, based on one-meter elevation band means of regression residuals using a combined metric of slope and aspect, were mostly negative below 2050 m, +30 to -40 cm; mostly positive between 2050-3300 m, $\pm$30 cm; and negative above 3300 m, – 10 to -140 cm. Although the study area is partly forested, only measurements in open areas were used. At lower elevations ablation is the primary cause of departure from the orographic trend. Above this elevation, to 3300 m, greater snow depths than predicted were found on the steeper terrain of the northwest and the less-steep northeast, suggesting that ablation, terrain orientation, slope and wind redistribution from the west all play a role in local snow depth variability at these elevations. At elevations above 3300 m orographic processes mask the effect of wind deposition when averaging over large areas due to flatter terrain. This suggests a reduction in precipitation from upslope lifting, the exhaustion of precipitable water from ascending air masses, or both. Our results suggest a precipitation gradient for the 2100-3300 m range of about 5.7 cm 100 m^{-1} elevation, a higher gradient than the widely used PRISM precipitation products, and a lower gradient than results from reconstruction of snowmelt amounts based on daily satellite snowcover data.

1. Introduction

In mountain regions of the western United States snowmelt is a dominant contributor to surface runoff, water use by vegetation and groundwater recharge (Bales et al. 2006, Earman 2011). Because of this importance, and the vulnerability of the mountain snowpack to climate warming, recent research has focused on the impacts of a rising elevation of the rain-snow transition on the annual and multiyear mountain water cycle and mountain ecosystems (Peterson et al. 2000, Marks et al. 2001, Lundquist et al. 2005, Barnett et al. 2008, Maxwell and Kollet 2008, Anderson and Goulden 2011, Trujillo et al. 2012).

The distribution of mountain precipitation is poorly understood at multiple spatial scales because it is governed by processes that are either not well measured or accurately predicted. However, since a large majority of precipitation in the middle and upper elevations of the southern Sierra Nevada falls and accumulates as snow, with little ablation through much of the winter, we can examine snow accumulation to assess processes governing the distribution of precipitation.

Snow accumulation across the mountains is primarily influenced by orographic processes, involving feedbacks between atmospheric circulation, terrain and the geomorphic processes of mountain uplift, erosion and glaciation on the earth's surface (Roe 2005, Kessler et al. 2006, Roe and Baker 2006, Stolar et al. 2007, Pedersen et al. 2010). Orographic precipitation is well documented and central to determining the amount of snow water equivalent (SWE) in mountainous regions. The Sierra Nevada, a major barrier to land-falling storms from the Pacific, is ideally oriented to produce orographic precipitation and exerts a strong influence on the upslope amplification of precipitation and the regional water budget (Pandey et al. 1999). Despite this well-developed conceptual understanding, our ability to apply this knowledge at spatial and temporal scales relevant to questions of regional climate and local forecasting are limited primarily due to our lack of accurate precipitation measurements in mountainous locations (Viviroli et al. 2011). Additionally, long narrow land-falling bands of extra-tropical Pacific water vapor, referred to as atmospheric rivers, frequently deposit

large fluxes of orographic precipitation as they ascend over the Sierra Nevada (Neiman et al. 2008, Ralph and Dettinger 2011). In some years atmospheric rivers can deposit more than half of the winter precipitation in the Sierra Nevada and represent a major link between ocean-atmosphere interactions and snowfall in the Sierra Nevada (Dettinger et al. 2011, Guan et al. 2012).

Peak seasonal SWE in snow-dominated elevations was originally conceived as a resource-management concept, used for defining the peak seasonal accumulation of snowpack water storage at index sites and to force statistically based runoff-prediction models for the subsequent spring and summer. In the Sierra Nevada April 1st is operationally defined as an index date for peak accumulation, and is coincident with monthly cooperative snow surveys conducted for over a century at various locations in the Sierra Nevada (Church 1933). While this approach has provided operationally robust predictions in years near the long-term normal, snow accumulation varies from year to year, is associated with changes in long-term climatic conditions, and has in recent decades, trended outside the statistical normal (Milly et al. 2008). Hence, our current methods are becoming less reliable and accurate predictions require a more comprehensive approach to understanding the processes affecting precipitation and the probabilities of extremes (Rahmstorf and Coumou 2011). Thus, it is expected that a principal uncertainty in future forecasts of runoff, moisture stress and other water-cycle fluxes is accurately estimating the amount and distribution of SWE (Rice et al. 2011, Meromy et al. 2012).

Current mountain-basin operational SWE estimates are made with a limited set of synoptic surveys and continuous in-situ point measurements. Snow-covered area and reflectance properties from satellite at landscape scales, and experimental data from satellites and aircraft, are used in research, and to a very limited basis in experimental forecasts. In both cases these measurements can be blended using statistical or spatially explicit models to produce discharge forecasts (Fassnacht et al. 2003, Molotch et al. 2005, Bales et al. 2008, Rice et al. 2011, Kerkez et al. 2012). Current ground measurements are limited by scale and by the heterogeneity of snow-accumulation processes (Bales et al. 2006, Viviroli et al. 2011). In a given watershed, uncertainty in

SWE estimates include the lack of spatially representative ground-based measurements, especially at the rain-to-snow transition and at high elevations, and the lack of under-canopy snow measurements (Molotch and Margulis 2008). Additionally, increasing winter temperatures will impact the distribution of rain versus snow across elevation gradients (Cayan et al. 2001). Thus, the skill of models for forecasting stream discharge are hindered by our lack of data in critical elevation bands and our limited ability to link remote-sensing and atmospheric data to precipitation patterns.

Research reported in this paper was aimed at determining the influences of terrain and orographic precipitation on patterns of seasonal snow accumulation along a 1650-m elevation gradient in the southern Sierra Nevada. Three specific questions posed in this research were: i) what is the variability in snow accumulation along an elevation gradient, ii) what is the magnitude of the orographic snow-accumulation pattern and, iii) to what extent do local terrain and wind redistribution influence this pattern. It was also our aim to use these results to assess prior model-based estimates of accumulated SWE and total precipitation.

2. Methods

Our approach involved analysis of: i) two LiDAR acquisitions, one when the ground was snow free and one near peak snow accumulation, ii) continuous ground-based measurements of snow depth, SWE, wind speed and air temperature, plus operational bright-band radar observations, and iii) model estimates of SWE and precipitation. The LiDAR data were used to estimate snow depth across the study area at a 1-m spatial resolution in open areas without canopy cover. The ground measurements were used in interpreting the spatial patterns and in estimating snow water equivalent, and the bright-band radar in determining the rain-snow transition elevation for precipitation events.

2.1 Location

Our study area is centered at approximately 36.5° latitude, and includes the 53 km^2 area covered by the two LiDAR flights in the southeastern part of the 135 km^2

Marble Fork of the Kaweah River watershed, located in Sequoia National Park in the southern Sierra Nevada (Figure 1). Elevations were 1850-3494 m, going from a Giant Sequoia grove at the lowest elevation, through mixed-conifer forests, to Red fir forests, subalpine forests and the alpine zone at the highest elevations. Continuous ground measurements of snow depth (26 points), SWE and meteorological variables (6 stations) in and near the flight area, plus 16 operational snow-depth and SWE sensors within 95 km of the study area, and operational bright-band radar observations up to 100 km upstream in the San Joaquin Valley and on the California coast were used to interpret the LiDAR-measured snow depth.

2.2 LiDAR altimetry

For this study airborne-scanning LiDAR altimetry was collected by the National Center for Airborne Laser Mapping (NCALM) using an Optech Gemini® ALTM 1233 airborne-scanning laser (Zhang and Cui 2007). The two campaigns were conducted in the 2010 water year: March 21-22 for snow on, and August 15 for snow off (Appendix A). The instrument settings used for acquisition provided a high point density, average >10 m^{-2}, and fine-scale beam-sampling footprint of approximately 20 cm (Table 1). Ground points were classified by NCALM through iteratively building a triangulated surface model with discrete points classified as ground and non-ground, where last returns were only considered for identifying ground points (Shrestha et al. 2007, Slatton et al. 2007). The nominal horizontal and vertical accuracy for a single flight path are 0.11m and 0.75 m, respectively; but higher accuracy was likely achieved where flight paths overlapped.

A digital surface model (DSM) was created by using first-return points and discarding outliers >100 m (tallest trees are approximately 85 m) and returns below -0.1 m; where values in the range -0.1 to 0 m were classified as 0. A continuous-coverage bare-earth digital elevation model (DEM) was created through kriging of ground points using a linear variogram with a nugget of 15 cm, a sill of 10 m, a range of 100 m, and a search radius of 100 m, where the minimum number of points was 5 (Guo 2010). We used a 1-m gridded model for representing our data, as this is the smallest footprint that most closely matches the expected beam sampling footprint and uncertainty in horizontal

accuracy. After interpolation, digital models of mean elevation and point-return density grids were georegistered to a common grid for snow-on and snow-off flights. The average point-return densities were 8 m^{-2} for the surface model and 3 m^{-2} for the bare-earth model. Grids with no point returns in $1m^2$, primarily under forest canopy, were considered null thus minimizing interpolation errors.

The accuracy of the LiDAR altimetry was evaluated using 352 geo-registered 2.5×2.5 m grid samples of the point cloud along the paved highway in the western part of the domain; because the highway is plowed regularly surface heights do not change with snow accumulation. These samples had a bias of +0.05 m and a standard deviation of 0.07 m, which is below the estimated combined two-flight instrumental elevation error of 0.11 m (Zhang and Cui 2007, Xiaoye 2008). A possible explanation of the 0.05 m bias for the snow-on flight is that some sections of the road had a small amount of snow remaining after plowing (personal communication Juan Fernandez, NCALM).

A 1-m gridded digital surface model of the vegetation canopy, created by subtracting the DSM from the DEM, was used to create a layer of vegetation canopy ≥ 2 m. In order to accurately determine snow depth, snow-depth values were further classified into two groups, where snow depth was either greater or less than the coincident vegetation height. This allowed us to consider for further analysis only snow from open slopes or where it had accumulated in the gaps between vegetation, mainly between trees, or covered it completely, i.e. covered understory. To reduce the amount of error we eliminated locations with slope >55°, warranted by the high number of erroneous values and known issues of vertical inaccuracies due to slope angle (Schaer et al. 2007, Deems et al. 2013). Additionally, we eliminated areas with rapid annual vegetation growth that had negative snow-depth values (e.g. areas within a wet meadow); and lastly we filtered out areas with open water, buildings, and parking lots where returns were not representative of local snow accumulation. Mean snow depth for each 1-m elevation band, with areas ≥ 100 m^2, was computed from the snow-depth grid. Additionally a 5-m elevation model, aggregated from the 1-m bare-earth model, was produced to remove scaling biases in the analysis of slope and aspect (Kienzle 2004, Erskine et al. 2006).

2.3 Spatial analysis

To analyze possible correlations between terrain steepness and snow distribution we calculated the first derivative of slope and snow depth, over distances of 5-100 m, using the 1-m mean snow depths and the corresponding mean slope for each 1-m elevation band, computing the correlation at 5-100 m using 5-m steps. Using the derivatives identifies transition areas.

For quantifying the combined effect of slope and aspect on snow depth we indexed aspect on a scale of 1 to -1 using methods adapted from Roberts (1986):

$$V_A = cos\ (\ A - FA) \tag{1}$$

where V_A is the aspect value, A is the azimuth variable and FA the focal aspect, e.g. 45° for northeast. The aspect value was further scaled by the sine of the slope angle, yielding 0 in flat terrain and approaching 1 as the mean slope increases:

$$I_A = sin\ (S) \cdot\ V_A \tag{2}$$

where I_A is aspect intensity and S the slope angle. The method of scaling the cosine of aspect by sine of slope is referred to as "northness" (Molotch et al. 2004). In this paper we expand this concept to include other aspects as well by centering the maximum value of the cosine on the focal aspect.

2.4 Ground measurements

Meteorological data were obtained from six meteorological stations in the flight area for the period from the first significant snowfall on December 3, 2009 to the LiDAR acquisition date, henceforth referred to as the snow-accumulation period. At these stations temperature was measured using Vaisala HMP-35 and Campbell T-108 sensors, with wind speed and direction measured using RM Young 5103 sensors. All meteorological stations measure hourly average wind speed; and two stations, Wolverton

and Panther, recorded maximum wind gusts at 10-second scan intervals (Appendix B). The M3, Topaz, and Emerald Lake stations are managed by the University of California Santa Barbara, Giant Forest is operated by the California Air Resources Board (data from http://mesowest.utah.edu/) and Case Mountain is managed by the Bureau of Land Management (data from http://www.raws.dri.edu). The Giant Forest station is located on an exposed shrub-covered slope; the Case Mountain, Wolverton and Panther stations are in forest openings; Emerald Lake is an alpine cirque; and Topaz and M3 are in alpine fell fields.

Wind sensors are between 4.2 and 6.5 m above ground level, and wind speeds were scaled to 10 m using a logarithmic profile to estimate saltation thresholds:

$$V_{10} = V_z \left[\frac{ln \frac{z_x}{k}}{ln \frac{z_{10}}{k}} \right] \quad (3)$$

where V_{10} is wind velocity at 10 m, $V_z$is measured velocity, z is instrument height, and k the site specific roughness length. To identify periods with the greatest potential for wind redistribution of snow we screened for times when temperature was below 0°C and wind velocity above the minimum saltation threshold of 6.7 m sec^{-1} established by Li and Pomeroy (1997a).

Snow depth was measured continuously by 26 ultrasonic snow-depth sensors (Judd Communications) placed on various slopes, aspects and canopy covers within 300 m of the Panther and Wolverton meteorological stations. These snow-depth sensors have an effective beam width of 22°, and were mounted 4.6 m above the ground on a steel arm extending 0.9 m from a vertical steel pipe anchored to a U-channel post. This arrangement provided up to a 2.3 m^2 snow-depth observation area over flat bare ground, with sampling area decreasing as snow depth increases.

The LiDAR measurements, plus ground-based snow-density measurements, were used to develop estimates of SWE versus elevation. Paired snow-depth and snow-pillow SWE measurements were part of the California Cooperative Snow Survey network and data were acquired from the California Department of Water Resources

(http://cdec.water.ca.gov/) for all 16 operable stations on the western slope of the southern Sierra Nevada within 100 km north and 50 km south of the study area (Figure 1). One snow pillow (GNF) is located 2.5 km west-southwest of the LiDAR acquisition area. Daily snow densities were estimated by dividing the daily mean SWE from the snow pillows by snow depth from the collocated ultrasonic depth sensors. To minimize the error from intermittent noise associated with snow pillows we used the daily average SWE and did not consider measurements under a 20-cm SWE threshold, where complete snow coverage of the pillow is unlikely and the combined uncertainties of depth sensors and snow pillows can yield significant error in SWE and density (Johnson and Schaefer 2002). All instrumental data were formatted, calibrated and gap filled by interpolation or correlation with other sensors and aggregated to daily means prior to analysis (Moffat et al. 2007). Less than 1% of meteorologic data required filtering or gap filling, snow-pillow data required slightly more, <5%, and snow depth required up to 20%, where data exceeding error thresholds required gap filling or interpolation (Appendix A). Stations with data gaps >2 days with no nearby station for interpolation were not used in our analysis.

2.5 Bright-band radar

The atmospheric rain-snow, hydrometeor transition elevation was determined from Doppler-radar bright-band snow-level analysis (Ryzhkov and Zrnic 1998, White 2003, Lundquist et al. 2008, White et al. 2009). These data, from analyses done by National Weather Service scientists, resolved hourly freezing levels of precipitation events occurring over wind profilers upstream of the LiDAR-acquisition area. We present data compiled from observations collected over the 2010 water year snow-accumulation period from the three nearest upwind locations of Punta Piedras Blancas, Lost Hills, and Chowchilla, California (Figure 1).

2.6 Model reanalysis

We calculated spatial SWE from LiDAR snow-depth measurements using mean snow-density measurements from the 16 snow-pillow sites. These values were compared with two scales of the widely used PRISM precipitation estimates, plus SWE estimates reconstructed from daily satellite snowcover (Daly et al. 1994, Daly et al. 2008, Rice and Bales 2011, Rice et al. 2011). Using the available 4-km and 800-m PRISM model output we summed precipitation for the accumulation period at the spatial extent of the LiDAR acquisition. The 4-km data were for the 2010 water year and the 800-m data were 30-year means. For comparison, we then calculated the total seasonal precipitation for each 1-m elevation band across the elevation gradient of both data sets, and aggregated values to the resolution of the comparative data. Whereas the reconstruction data presented are the 2000-2009 accumulation-period means of the entire Kaweah River watershed based on 300-m elevation-bin averages of MODSCAG reconstructed SWE (Rice and Bales 2013).

3. Results

3.1 LiDAR-measured snow depth

Of the 53.1 km^2 planer footprint of the LiDAR survey, 0.8 km^2 were over water or in areas that exceeded filter thresholds of the DSM. An additional 0.01 km^2 of area with slope >55°, roads and buildings, and rapidly growing meadow vegetation were also excluded from the analysis. The total snow-covered area, where both LiDAR and ground returns were available at a density $\geq$1 m^{-2}, was 40.2 km^2 and of this area 5.0 km^2 was under tree canopies and also excluded from analysis. This left an area of 35.2 km^2 remaining and of this <0.2 km^2, mostly below 2300 m, was snow free. Mean snow depth of this area, measured by LiDAR, increased with altitude from 1850 to 3300 m elevation, with depths decreasing above 3300 m (Figure 2a). At elevations below 2050 m the linear slope of snow depth versus elevation is similar to that above with the exception of a short steep increase in snow depth at 2000-2050 m. Up to 3300 m, snow depth shows a strong correlation with elevation (R^2 = 0.974, $p < 0.001$), increasing at 15 cm per 100 m elevation. Above 3300 m, snow depth sharply decreased at a rate of -48 cm. The increase in snow depth with elevation up to 3300 m is accompanied by a decrease in canopy cover

with elevation. Canopy cover, based on the canopy-height model, is greater than 40% below 2600 m, and near zero above 3300 m (Figure 2b). Overall, the total area of canopy cover over 2 m in height is 11.9 km^2 and mostly below 2800 m in elevation.

3.2 Wind and topographic effects

Hourly average wind speed at the 6 meteorological stations showed that the highest potential for redistributing snow was from the westerly directions, with a few periods with strong winds from the northeast at Topaz (Figures 2f and 2g). We found the greatest potential for redistribution at the 3 stations above 2800 m and, to a lesser extent, at one lower elevation station, Giant Forest, which is located in an exposed area free of upwind vegetation. Only five instantaneous gusts over 6.7 m sec^{-1} were recorded at Panther during the snow-accumulation period, and one at Wolverton; and no hourly averages at these sites were over 6.7 m sec^{-1} (Appendix A).

Snow depths classified by aspect were lowest in the southwest and southeast quadrants, and highest in the northwest and northeast (Figure 2c). This pattern was most pronounced at elevations above 2400 m in all quadrants, and especially between 2300-2700 m in the southeast; although only a small percentage of area falls into the southeast classification at this elevation (Figure 2c). The aspect with the least overall area of representation is northeast and the greatest is the northwest.

A visual comparison of mean slope with mean snow depth suggests a secondary trend due to terrain slope (Figure 2d). The derivatives, or changes in mean snow depth and slope over 5-100 m averaging lengths show an (anti) correlation at 5 m of -0.16, which becomes most negative at 35 m (-0.36), and tapers to -0.16 at 120 m (Figure 2h). When plotted together the most rapid changes in slope show the greatest antithetical response in snow depth until reaching 3300 m, where they become more-positively correlated as the terrain becomes flatter (Figure 2e).

The combined effects of slope and aspect express the "aspect intensity" (I_A), where higher values represent more terrain at that aspect and/or greater slope angles (Figure 3a). This analysis reveals the terrain-feature space of the study area, where the predominant (half quadrant) aspects are north, southwest, west and northwest, which

have positive I_A values; and their less-represented respective reciprocals of south, northeast, east and southeast, which have negative values. At elevations <2000 m, moderate east and southeast slopes, indicated by the slightly negative I_A values, quickly rise to steeper north, northwest and west slopes, as indicated by the higher and positive I_A values (Figure 3a). Near 2400 m, southwest aspects become more predominant than north, as indicated by the crossover in I_A values, and at higher elevations aspect becomes equally represented by west, southwest and northwest, with some southerly aspects (negative north I_A values) above 2800 m (Figure 3a).

To evaluate the terrain effects secondary to elevation we applied a regression to all snow depths as a function of elevation using the slope and intercepts for 1850-3300 m (Table 2). The residuals from this regression were then correlated with I_A. The I_A profiles most highly correlated with residuals were southwest at the lowest (1850-2051 m) and highest (3300-3494 m) elevations, and northwest at the mid elevations (2051-3301 m) (Table 2). Relatively high correlations where also found with north at 1850-2050 m, though of opposite sign, and west at 2051–3300 and 3301-3494 m, of the same sign.

3.3 Bright - band radar

The radar sounding data include 8287 hourly observations (353 missing), with freezing levels ranging from 200 to 2700 m (Figure 4). The greatest variability and highest mean freezing level occurred at the coastal station of Punta Piedras and the lowest at the furthest inland station of Chowchilla. This decline in mean and freezing levels, going from the coast inland, suggests that the snow level drops as the air mass moves inland. The freezing level of the farthest inland station, Chowchilla, is 2263 m; this closely tracks the break in the coefficient of variation and correlation between snow depth and elevation observed from LiDAR at 2050 m (Figure 2a).

3.4 Ground measurements

The LiDAR flights were 17 days after peak depth and three weeks before peak SWE (Figures 5a, 5b).The mean and standard deviation of snow depth during LiDAR acquisition, recorded by the 42 depth sensors, was 210 $\pm$38 cm. This was 19% less than

the mean peak depth of 266 ±44 cm recorded on March 4th. However, the mean SWE recorded by the 16 snow pillows during LiDAR acquisition was 82 ±16 cm, 2% less than the mean peak SWE of 83 ±20 on April 14. Two snow pillows, the lowest, Giant Forest (GNF) at 2027 m, and the most southerly, Quaking Aspen (QUA) at 2195 m, reached peak SWE one week before acquisition, on March 15th, and had ablated 9% and 7 % SWE, respectively, prior to the time of the LiDAR acquisition (Figure 5b). All other snow pillows either gained SWE or ablated <5 % in the period prior to the snow LiDAR acquisition. Snow depths measured at the snow-pillow sites on the days of the LiDAR flights failed to show the elevation patterns apparent in the LiDAR depths (Figure 6).

Daily density values calculated for the 16 snow-pillow locations for Feb 1 to Apr 30 indicate a general trend of increasing density and consistent intra-site patterns of accumulation and densification corresponding with stormy and clear conditions (Figure 5). Over the 3-month period, density decreased with each accumulation event and increased through densification as the snowpack settled, metamorphosed and integrated free water from melt or rain. At the time of the LiDAR flights the mean density was 384 kg m^{-3}, with a range of ±83 kg m^{-3} and standard deviation of 42 kg m^{-3} across the 1036-m elevation range represented in these data. The combined measurement error of snow-pillow and depth-sensor instruments used in the density calculation can be greater than the range of variability reported here (Johnson and Schaefer 2002). We found low spatial variability in density that showed no significant relationship with elevation at our sites. This observation concurs with other studies of mountain snowpacks finding spatial consistency in the density of mountain snowpacks (Mizukami and Perica 2008, Jonas et al. 2009). Making these assumptions we estimated the SWE for each elevation band over our measurement domain to be the product of mean density and snow depth as represented in (Figure 4c).

3.*5 Model reanalysis*

The 4-km resolution PRISIM data were comprised of 7 grid elements in the study domain, whereas the 800-m product had approximately 4225 grid elements. The snowmelt and PRISM data show a positive correlation between precipitation and

elevation up to ~3300 m and a reversal of this trend at the higher elevations, as do the LiDAR data; but they differ markedly in their slopes and intercepts (Figure 7). The 4-km and 800-m PRISM data demonstrate similar magnitudes of increase in precipitation with elevation, 3.3 and 2.3 cm 100 m^{-1} respectively. The LiDAR SWE and reconstructed snowmelt both have slopes of 6 cm 100 m^{-1}. However, the SWE estimates from reconstructed snowmelt are offset 0.2-0.4 cm from the LiDAR estimates. Because of the shallow slope of the precipitation versus elevation line, the PRISM estimates diverge from the LiDAR values below about 2800 m.

4. Discussion

The patterns of snow depth on Figure 2 represent the interplay of orographic, physiographic, and climatic influences on precipitation and snowmelt. Local departures from the orographic/climatic pattern at finer scales may reflect the influence of physiographic variability in slope and aspect on snow accumulation.

Early in the year, before high solar zenith angles accelerate spring snow ablation, orographic deposition, vegetation and wind are the dominant influences on snow distribution. While interannual snow depth varies significantly, these factors should produce spatial patterns of snow accumulation that are somewhat stationary from year to year, e.g. deep or shallow snow will be found in the same locations. This stationarity has been observed in environments as diverse as the Arctic and Rocky Mountains (Erickson et al. 2005, Deems et al. 2008, Sturm et al. 2010). The overall increase in snow depth with elevation in the current domain is consistent with the orographic effect of mountains on precipitation (Roe 2005, Roe and Baker 2006). At lower elevations, e.g. below 2050 m, a mix of rain and snow precipitation appears to influence the amount of seasonal snow accumulation. Above 3300 m, the reduced lift over flatter terrain and an exhaustion of precipitable water as storms rise less steeply result in declining snow depths at the higher-elevations (Houze 2012).

4.1 Rain-snow transition

Seasonal snow accumulation at the lowest elevations and on south-facing slopes is “warmer” than snow from higher elevations and on north-facing slopes that has fallen at colder temperatures, accumulated to greater depths and kept cold for longer periods of time. Hence, locations with less snow, greater positive net energy exchange (from radiation or condensation), and a larger fraction of liquid precipitation, are most susceptible to melt during the accumulation period. The impact of a warming climate is most evident at these elevations due to the increase in minimum winter air temperatures and liquid precipitation from tropical storms; and both affect the amount of snow covered area on mountain slopes (Aguado 1990, Cayan 1996, Cayan et al. 2001, Dettinger et al. 2004).

Below 2050 m we find a consistently high coefficient of variation in depth, and a steep increase in snow depth vs. elevation between 2000 and 2050 m (Figure 2a). This elevation range tracks very closely with the seasonal-aggregate hourly freezing-level consensus resolved with bright-band reflectance data collected from upwind profiler stations on the California Coast and Central Valley (Figures 1 and 4). The hourly consensus of bright-band freezing levels over wind profilers represent the transition elevation where hydrometeors turn from frozen to liquid, and our instrumental data frequently show a concurrent reduction in snow depth with bright-band freezing levels. However, as other researchers have noted, it is difficult to identify the effects of specific storms on snowpack ablation due to the variability of atmospheric conditions close to the earth’s surface (Ryzhkov and Zrnic 1998, Lundquist et al. 2008). Local SWE measurements are only available at one location below 2050 m (GNF); and this station does show a loss of SWE in mid-February as a result of a rain-on-snow event (Figure 5). SWE, stream discharge or soil-moisture measurements may help resolve the impact of individual rain events and identify the elevations where this transition occurs. Nevertheless, given the expected large storm-to-storm variation in freezing level, the relatively sharp transition in slope of snow accumulation at about 2050 m does suggest that in the winter 2010, most precipitation above this elevation fell as snow and winter melt was of secondary importance.

4.2. Terrain slope, wind redistribution and aspect intensity

The profiles of snow depth and slope (Figures 2a and 2d) suggest an inverse relationship. This is seen most clearly at an averaging window of 35 m, as indicated by the correlation between the change in slope and the change in snow depth (Figures 2e and 2h). These results indicate that greater snow depths will be found in locations of decreasing slope, e.g. the toe of slopes and valley bottoms, suggesting the role of wind redistribution in these less-turbulent and gravitationally favorable locations. In concurrence with our wind observations, snow-depth profiles by aspect also show more accumulation on the northeast slopes and less on the southwest; however, in our domain, northeast has the least total area of all aspect quadrants (Figure 2c).

Our results suggest that wind patterns from a single station may be a poor indicator of the wind fields influencing snow redistribution across the entire domain. We attribute the inconsistent wind direction between stations to terrain capable of modifying the turbulence of the free atmosphere upwind of the stations. The M3 and Emerald Lake sites have upwind obstacles, and the Wolverton and Panther stations have low wind speeds, reflecting the muting effect of tall forest cover on wind speed and consequently snow redistribution. Topaz Lake is located in smooth terrain with limited upwind influence; and for this reason the Topaz Lake station may best represent the wind patterns of the free atmosphere and predominant southwest storm winds. We expected snow transport by wind to be coarsely defined by the consensus of the station data, with a strong potential for anisotropic deposition, favoring primarily northeast and secondarily southeast slopes. We see this pattern reflected when considering snow depths classified only by aspect as in Figure 2c, and to a limited extent the distribution of residuals to the southeast below 3300 m (Figure 3c).

The residuals plotted with I_A indicate that snow depths on the steeper, northwest-facing slopes at the mid elevations and northerly slopes at the lowest elevations show the greatest positive departures from depth predicted by elevation alone (Figure 3c). The most-negative departures are found at the highest elevations, trending from the southwest to northeast on the shallow slopes of the flatter terrain. However, the correlation of snow depth residuals with I_A does not emphasize greater snow depths in the limited area of

low-gradient easterly aspects, where wind deposition is most likely to occur (Figures 3a and 3c). These findings suggest that small-scale departures from the overall orographic trend can be observed in the elevation profile, but require a localized approach such as classification to identify relevant spatial patterns on the landscape. This approach has been effective in the case of localized wind deposition, offering a deterministic explanation for spatial stationarity in snow-patch development and persistence (Winstral et al. 2002, Schirmer et al. 2011). In our domain it is possible that wind effects are masked when considering topography as an elevation-band mean due to the limited easterly aspects in the predominantly northwest-facing basin. It is also possible that there is limited utility in considering prevailing winds when predicting localized effects of wind on snow redistribution, where the roughness length exceeds the scale of interest. Research into the relationship between slope, aspect and wind has found small-scale slope breaks and surface roughness, dynamic in a snow-covered environment, having the most significant effects on where snow accumulates (Li and Pomeroy 1997b, Pomeroy and Li 2000, Winstral et al. 2002, Fang and Pomeroy 2009).

Aspect intensity provides a method for characterizing the combined influence of slope and aspect and its effect on physical or ecological processes. It can serve as a proxy for several processes affecting snow depth, radiation, upslope deposition and potentially wind and gravitational redistribution. The radiation influence arises because aspect and slope greatly enhance or reduce incoming and reflected radiation in relationship to the ray path from the sun. Upslope deposition is important because precipitation amounts are highly correlated with the steepness of the terrain and winds that are orthogonal to the slope (White et al. 2003). The processes of wind saltation and turbulent redistribution, farther from the ground surface, favor deposition on leeward aspects but not on the steepest slopes. For this reason I_A, which is amplified by slope, does not have a linear relationship with wind deposition; likewise for gravitational redistribution. However, by using classification methods and further analysis, beyond the scope of this paper, I_A will likely be an effective tool for this as well.

4.3. Depth-density relationship

Time-series data in and around our measurement domain suggest that melt and sublimation are limited during the accumulation period, and snow density is relatively consistent between measurement sites (Figures 5 and 6). Measurements of SWE from 16 snow pillows over 1300 m of elevation show snowmelt losses ranging from about 10 cm at GNF to zero at KSP, with most sites showing less than 3 cm loss in SWE over the entire accumulation period (Figure 5b). In dry intercontinental locations the sublimation plus evaporation rates can be in excess of 50%, but are much lower in the maritime climate of the Sierra Nevada and lowest during the accumulation period (Essery and Pomeroy 2001, Ellis et al. 2010b). Studies conducted at 2800 and 3100 m in the Emerald Lake basin, located in the center of our measurement domain, found net losses due to evaporation and sublimation of <10% for the period between December 1st and April 1st (Marks and Dozier 1992, Marks et al. 1992). In the 2010 water year we consider cumulative loss due to sublimation/evaporation and snowmelt to be minimal prior to the LiDAR acquisition at all elevation bands, with more melt occurring at the lowest elevations and on the southeast facing slopes as indicated by the loss of SWE measured at the low-elevation snow-pillow sites and reduced snow depths on the southeast mid-elevation slopes (Figure 3).

4.4 Model comparisons

Although orographic precipitation is a well-documented first-order process, in the Sierra Nevada it is not well described at the watershed to basin scale owing to the very limited availability of ground-based SWE and precipitation measurements. One set of measurements, described above, and two additional model data sets, which are based in part on measurements (mainly from lower elevations), are available for comparison with the current LiDAR snow-depth data: i) the point snow-pillow data, ii) the widely used, gridded PRISM precipitation estimates (Daly et al. 1994, Daly et al. 2008) and iii) seasonal snowmelt estimates reconstructed from daily satellite snowcover data (Rice and Bales 2011, Rice et al. 2011). Each set of measurements provides a different index of orographic response where i) LiDAR is a one-time snapshot of snow depth; ii)

reconstructed snowmelt is a retrospective SWE estimate, reflecting precipitation minus evaporation and sublimation; and iii) PRISM is a retrospective precipitation estimate, based largely on lower-elevation stations. Nevertheless, these models offer the best available spatially relevant indices of seasonally accumulated precipitation and incorporate in-situ measurements, remote-sensing observations or both.

As Figure 6 shows, snow depths from snow-pillow sites fail to capture the elevation patterns apparent in the LiDAR data. This pattern is also apparent in the SWE values from the same sites (Figure 5b). While the least depth is registered at the lowest elevation site (GNF, 2027 m), where a greater percentage of precipitation falls as rain, the other sites do not consistently increase with elevation; for this reason we chose to convert LiDAR snow depth to SWE using the mean of all available instrumental snow densities. PRISM data from the 4-km and 800-m PRISM models are calculated over the same area as the LiDAR data, whereas the retrospective-snowmelt model data are for the entire Kaweah River watershed (Figure 7). The snowmelt reconstruction and PRISM data both show a positive correlation between precipitation and elevation up to ~3300 m and a reversal of this trend at higher elevations, as do the LiDAR data, but they differ markedly in their slopes and intercepts (Table 2). The two PRISM profiles do not demonstrate the same magnitude of increase in precipitation with elevation that we see in the LiDAR or reconstructed SWE. We believe this is due to a combination of three factors. First, the limited number of stations used to calculate the PRISM trends, the lack of mountain stations in particular; second, the fraction of total precipitation contributed by rain; and third, SWE loss from ablation due to melt, sublimation and evaporation, mostly at lower elevations in the SWE reconstruction and LiDAR. While these effects are most important below 2050 m, they can have a small influence, on the order of about 10%, above that elevation.

SWE from reconstructed snowmelt and LiDAR SWE have very similar slopes, but the reconstruction has less SWE, particularly at the lower elevations. The reduced lower-elevation SWE in the reconstruction is expected because: i) as seen in Figure 3 the LiDAR domain encompasses more northerly, less-ablation-prone slopes than the more-evenly split watershed, ii) there is a decreased contribution of under-canopy SWE due to

lower-elevation forest cover, which was filtered from LiDAR measurements, and iii) there was 90% of average precipitation in the 2000-2009 snowmelt reconstruction period versus a 106% seasonal average when the 2010 LiDAR data were collected. Also, the offset in the reconstructed SWE estimates may reflect a bias in snow-covered area estimates, which have a 500-m spatial resolution and are heavily influenced by canopy (Rice et al., 2011). That is, the LiDAR data represent open areas, and the reconstructed SWE values represent the full domain, but empirically corrected for canopy. Further, these reconstructed SWE estimates are based on a temperature-index calculation, versus a full energy-balance approach. Regardless of these differences, the reduction in snow depth we observe at the highest elevations is captured by the two PRISM models and the snowmelt reconstruction. The latter also closely follows the pattern of precipitation found by our measurements, albeit at a much courser scale and larger domain. These results emphasize the need for instrumental data assimilation across the entire elevation gradient for accurate estimates of SWE.

5. Conclusions

The current results show elevation as the primary determinant of snow depth near the time of peak accumulation over 1650 m of the west slope of the southern Sierra Nevada, which drop-off near the crest. This profile shows large- and small-scale trends from orographic processes, mean freezing level, slope, terrain orientation and wind redistribution. Snow depth increased approximately 15 cm per 100 m elevation from snow line to about 3300 m and, when scaled using mean regional snow density on the acquisition dates (384 kg m^{-3}), equals approximately 6 cm per 100 m elevation SWE. This rate is nearly equal to SWE reconstructions but much higher than the widely used PRISM precipitation data. Localized departures from this trend of +30 to -140 cm from the km-scale pattern of linear increase with elevation are seen in an elevation profile of 1-m elevation bands. From 3300 m to our highest measurements at 3494 m, snow depth decreases approximately 48 cm per 100 m elevation. Both PRISM and SWE reconstructions show reductions at higher elevations as well.

The spatial coverage of LiDAR-derived snow depth demonstrated here provides an effective bridge between space-borne observing platforms, point-scale measurements and models to resolve persistent patterns of snow accumulation. LiDAR-derived snow-depth measurements obtained at peak accumulation provide a scalable template for identifying the spatial variability of seasonally integrated snow-depth and SWE within a domain. LiDAR estimates of snow accumulation in open areas with limited canopy influence provide a much-needed "ground truth" estimate of precipitation free of canopy influence.

These scalable results of snow elevation gradients and finer-scale patterns of deposition and melt provide a basis for developing accurate representations of snow depth of local to regional relevance for snow researchers, the remote-sensing community and water-resource managers. As this body of data grows from research initiatives to operationally useful assessments of seasonal water storage, discharge and flood potential, so too should our understanding of ecohydrologic responses to short- and long-term perturbations. Catalogs of repeat snow-depth measurements will further constrain estimates of SWE in specific watersheds with respect to elevation, the persistent seasonal effects of wind, topography and the impact of anomalous climate patterns.

Acknowledgements

Research was supported by the National Science Foundation (NSF), through the Southern Sierra Critical Zone Observatory (EAR-0725097) and NSF grants (EAR 1141764, EAR 1032295, EAR 0922307), a fellowship for the first author from the Southern California Edison Company and a seed grant through Lawrence Livermore National Laboratory (6766). Supplemental support was also provided by T. Painter at the Jet Propulsion Laboratory. We acknowledge the comments from J. Fernandez Diaz, R. Rice, C. Riebe T. Harmon, M. Conklin, and M. Goulden and thank Jim Sickman and John Melack for providing meteorological data.

References

Aguado, E. 1990. Elevational and latitudinal patterns of snow accumulation departures from normal in the Sierra Nevada Theoretical and Applied Climatology **42**:177-185.

Anderson, R. G., and M. L. Goulden. 2011. Relationships between climate, vegetation, and energy exchange across a montane gradient. Journal of Geophysical Research-Biogeosciences **116**.

Bales, R. C., K. A. Dressler, B. Imam, S. R. Fassnacht, and D. Lampkin. 2008. Fractional snow cover in the Colorado and Rio Grande basins, 1995-2002. Water Resources Research **44**.

Bales, R. C., N. P. Molotch, T. H. Painter, M. D. Dettinger, R. Rice, and J. Dozier. 2006. Mountain hydrology of the western United States. Water Resources Research **42**.

Barnett, T. P., D. W. Pierce, H. G. Hidalgo, C. Bonfils, B. D. Santer, T. Das, G. Bala, A. W. Wood, T. Nozawa, A. A. Mirin, D. R. Cayan, and M. D. Dettinger. 2008. Human-induced changes in the hydrology of the western United States. Science **319**:1080-1083.

Cayan, D. R. 1996. Interannual climate variability and snowpack in the western United States. Journal of Climate **9**:928-948.

Cayan, D. R., S. A. Kammerdiener, M. D. Dettinger, J. M. Caprio, and D. H. Peterson. 2001. Changes in the onset of spring in the western United States. Bulletin of the American Meteorological Society **82**:399-415.

Church, J. E. 1933. Snow surveying: its principles and possibilities. Geographical Review **23**: 529 - 563.

Daly, C., M. Halbleib, J. I. Smith, W. P. Gibson, M. K. Doggett, G. H. Taylor, J. Curtis, and P. P. Pasteris. 2008. Physiographically sensitive mapping of climatological temperature and precipitation across the conterminous United States. International Journal of Climatology **28**:2031-2064.

Daly, C., R. P. Neilson, and D. L. Phillips. 1994. A statistical topographic model for mapping climatolological precipitation over mountainous terrain. Journal of Applied Meteorology **33**:140-158.

Deems, J. S., S. R. Fassnacht, and K. J. Elder. 2008. Interannual Consistency in Fractal Snow Depth Patterns at Two Colorado Mountain Sites. Journal of Hydrometeorology **9**:977-988.

Deems, J. S., T. H. Painter, and D. C. Finnegan. 2013. Lidar measurement of snow depth: a review. Journal of Glaciology **59**:467.

Dettinger, M., K. Redmond, and D. Cayan. 2004. Winter orographic precipitation ratios in the Sierra Nevada - Large-scale atmospheric circulations and hydrologic consequences. Journal of Hydrometeorology **5**:1102-1116.

Dettinger, M. D., F. M. Ralph, T. Das, P. J. Neiman, and D. R. Cayan. 2011. Atmospheric Rivers, Floods and the Water Resources of California. Water **3**:445-478.

Earman, S., Dettinger, M. 2011. Potential impacts of climate change on groundwater resources – a global review. Journal of Water and Climate Change **2**:213 - 229.

Ellis, C. R., J. W. Pomeroy, T. Brown, and J. MacDonald. 2010. Simulation of snow accumulation and melt in needleleaf forest environments. Hydrology and Earth System Sciences **14**:925-940.

Erickson, T. A., M. W. Williams, and A. Winstral. 2005. Persistence of topographic controls on the spatial distribution of snow in rugged mountain terrain, Colorado, United States. Water Resour. Res. **41**:W04014.

Erskine, R. H., T. R. Green, J. A. Ramirez, and L. H. MacDonald. 2006. Comparison of grid-based algorithms for computing upslope contributing area. Water Resources Research **42**:9.

Essery, R., and J. Pomeroy. 2001. Sublimation of snow intercepted by coniferous forest canopies in a climate model. Pages 343-347 Soil-Vegetation-Atmosphere Transfer Schemes and Large-Scale Hydrological Models.

Fang, X., and J. W. Pomeroy. 2009. Modelling blowing snow redistribution to prairie wetlands. Hydrological Processes **23**:2557-2569.

Fassnacht, S. R., K. A. Dressler, and R. C. Bales. 2003. Snow water equivalent interpolation for the Colorado River Basin from snow telemetry (SNOTEL) data. Water Resources Research **39**:1208, doi: 1210.1029/2002WR001512.

Guan, B., D. E. Waliser, N. P. Molotch, E. J. Fetzer, and P. J. Neiman. 2012. Does the Madden-Julian Oscillation Influence Wintertime Atmospheric Rivers and Snowpack in the Sierra Nevada? Monthly Weather Review **140**:325-342.

Guo, Q., Li, W., Yu, H., Alvarez, O. 2010. Effects of Topographic Variability and Lidar Sampling Density on Several DEM Interpolation Methods. Photogrammetric Engineering & Remote Sensing **76**.

Houze, R. A., Jr. 2012. Orographic effects on precipitating clouds. Rev. Geophys. **50**:RG1001.

Johnson, J. B., and G. L. Schaefer. 2002. The influence of thermal, hydrologic, and snow deformation mechanisms on snow water equivalent pressure sensor accuracy. Hydrological Processes **16**:3529-3542.

Jonas, T., C. Marty, and J. Magnusson. 2009. Estimating the snow water equivalent from snow depth measurements in the Swiss Alps. Journal of Hydrology **378**:161-167.

Kerkez, B., S. D. Glaser, R. C. Bales, and M. W. Meadows. 2012. Design and performance of a wireless sensor network for catchment-scale snow and soil moisture measurements. Water Resources Research **48**.

Kessler, M. A., R. S. Anderson, and G. M. Stock. 2006. Modeling topographic and climatic control of east-west asymmetry in Sierra Nevada glacier length during the Last Glacial Maximum. Journal of Geophysical Research-Earth Surface **111**.

Kienzle, S. 2004. The Effect of DEM Raster Resolution on First Order, Second Order and Compound Terrain Derivatives. Transactions in GIS **8**:83-111.

Li, L., and J. W. Pomeroy. 1997a. Estimates of threshold wind speeds for snow transport using meteorological data. Journal of Applied Meteorology **36**:205-213.

Li, L., and J. W. Pomeroy. 1997b. Probability of occurrence of blowing snow. Journal of Geophysical Research-Atmospheres **102**:21955-21964.

Lundquist, J. D., M. D. Dettinger, and D. R. Cayan. 2005. Snow-fed streamflow timing at different basin scales: Case study of the Tuolumne River above Hetch Hetchy, Yosemite, California. Water Resources Research **41**.

Lundquist, J. D., P. J. Neiman, B. Martner, A. B. White, D. J. Gottas, and F. M. Ralph. 2008. Rain versus snow in the Sierra Nevada, California: Comparing Doppler profiling radar and surface observations of melting level. Journal of Hydrometeorology **9**:194-211.

Marks, D., and J. Dozier. 1992. Climate and Energy Exchange at the Snow Surface in the Alpine Region of the Sierra-Nevada .2. Snow Cover Energy-Balance. Water Resources Research **28**:3043-3054.

Marks, D., J. Dozier, and R. E. Davis. 1992. Climate and Energy Exchange at the Snow Surface in the Alpine Region of the Sierra-Nevada .1. Metrological Measurements and Monitoring. Water Resources Research **28**:3029-3042.

Marks, D., T. Link, A. Winstral, and D. Garen. 2001. Simulating snowmelt processes during rain-on-snow over a semi-arid mountain basin. Pages 195-202 *in* K. Hutter, editor. Annals of Glaciology, Vol 32, 2001.

Maxwell, R. M., and S. J. Kollet. 2008. Interdependence of groundwater dynamics and land-energy feedbacks under climate change. Nature Geoscience **1**:665-669.

Meromy, L., N. P. Molotch, T. E. Link, S. R. Fassnacht, and R. Rice. 2012. Subgrid variability of snow water equivalent at operational snow stations in the western USA. Hydrological Processes:n/a-n/a.

Milly, P. C. D., J. Betancourt, M. Falkenmark, R. M. Hirsch, Z. W. Kundzewicz, D. P. Lettenmaier, and R. J. Stouffer. 2008. Climate Change: Stationarity Is Dead: Whither Water Management? Science **319**:573-574.

Mizukami, N., and S. Perica. 2008. Spatiotemporal Characteristics of Snowpack Density in the Mountainous Regions of the Western United States. Journal of Hydrometeorology **9**:1416-1426.

Moffat, A. M., D. Papale, M. Reichstein, D. Y. Hollinger, A. D. Richardson, A. G. Barr, C. Beckstein, B. H. Braswell, G. Churkina, A. R. Desai, E. Falge, J. H. Gove, M. Heimann, D. Hui, A. J. Jarvis, J. Kattge, A. Noormets, and V. J. Stauch. 2007. Comprehensive comparison of gap-filling techniques for eddy covariance net carbon fluxes. Agricultural and Forest Meteorology **147**:209-232.

Molotch, N. P., M. T. Colee, R. C. Bales, and J. Dozier. 2005. Estimating the spatial distribution of snow water equivalent in an alpine basin using binary regression tree models: the impact of digital elevation data and independent variable selection. Pages 1459-1479.

Molotch, N. P., and S. A. Margulis. 2008. Estimating the distribution of snow water equivalent using remotely sensed snow cover data and a spatially distributed snowmelt model: A multi-resolution, multi-sensor comparison. Advances in Water Resources **31**:1503-1514.

Molotch, N. P., T. H. Painter, R. C. Bales, and J. Dozier. 2004. Incorporating remotely-sensed snow albedo into a spatially-distributed snowmelt model. Geophysical Research Letters **31**:L03501.

Neiman, P. J., F. M. Ralph, G. A. Wick, J. D. Lundquist, and M. D. Dettinger. 2008. Meteorological characteristics and overland precipitation impacts of atmospheric rivers affecting the West Coast of North America based on eight years of SSM/I satellite observations. Journal of Hydrometeorology **9**:22-47.

Pandey, G. R., D. R. Cayan, and K. P. Georgakakos. 1999. Precipitation structure in the Sierra Nevada of California during winter. Journal of Geophysical Research-Atmospheres **104**:12019-12030.

Pedersen, V. K., D. L. Egholm, and S. B. Nielsen. 2010. Alpine glacial topography and the rate of rock column uplift: a global perspective. Geomorphology **122**:129-139.

Peterson, D. H., R. E. Smith, M. D. Dettinger, D. R. Cayan, and L. Riddle. 2000. An organized signal in snowmelt runoff over the western United States. Journal of the American Water Resources Association **36**:421-432.

Pomeroy, J. W., and L. Li. 2000. Prairie and arctic areal snow cover mass balance using a blowing snow model. Journal of Geophysical Research-Atmospheres **105**:26619-26634.

Rahmstorf, S., and D. Coumou. 2011. Increase of extreme events in a warming world. Proceedings of the National Academy of Sciences.

Ralph, F. M., and M. D. Dettinger. 2011. Storms, floods, and the science of atmospheric rivers. Eos Trans. AGU **92**.

Rice, R., and R. Bales. 2013. Water Qauntity: rain, snow, and temperature. Natural Resource Report. NPS/SEKI/NRR-2013/665.7a. National Park Service, Fort Collins, Colorado.

Rice, R., and R. C. Bales. 2011. An Assessment of Snowcover in 6 Major River Basins of Sierra Nevada and Potential Approaches for Long-term Monitoring.*in* Fall Meeting, AGU, San Francisco, Calif.

Rice, R., R. C. Bales, T. H. Painter, and J. Dozier. 2011. Snow water equivalent along elevation gradients in the Merced and Tuolumne River basins of the Sierra Nevada. Water Resources Research **47**:11.

Roberts, D. W. 1986. Ordination on the basis of fuzzy set theory. Vegetatio **66**:123-131.

Roe, G. H. 2005. Orographic precipitation. Pages 645-671 Annual Review of Earth and Planetary Sciences. Annual Reviews, Palo Alto.

Roe, G. H., and M. B. Baker. 2006. Microphysical and geometrical controls on the pattern of orographic precipitation. Journal of the Atmospheric Sciences **63**:861-880.

Ryzhkov, A. V., and D. S. Zrnic. 1998. Discrimination between rain and snow with a polarimetric radar. Journal of Applied Meteorology **37**:1228-1240.

Schaer, P., J. Skaloud, S. Landtwing, and K. Legat. 2007. Accuracy Estimation for Laser Point Cloud Including Scanning Geometry.

Schirmer, M., V. Wirz, A. Clifton, and M. Lehning. 2011. Persistence in intra-annual snow depth distribution:1 Measurements and topographic control. Water Resour. Res. **47**:W09516.

Shrestha, R., W. Carter, C. Slatton, and W. Dietrich. 2007. "Research-Quality" Airborne Laser Swath Mapping: The Defining Factors. The National Center for Airborne Laser Mapping.

Slatton, K. C., W. E. Carter, R. L. Shrestha, and W. Dietrich. 2007. Airborne Laser Swath Mapping: Achieving the resolution and accuracy required for geosurficial research. Geophysical Research Letters **34**:5.

Stolar, D., G. Roe, and S. Willett. 2007. Controls on the patterns of topography and erosion rate in a critical orogen. J. Geophys. Res. **112**:F04002.

Sturm, M., B. Taras, G. E. Liston, C. Derksen, T. Jonas, and J. Lea. 2010. Estimating Snow Water Equivalent Using Snow Depth Data and Climate Classes. Journal of Hydrometeorology **11**:1380-1394.

Trujillo, E., N. P. Molotch, M. L. Goulden, A. E. Kelly, and R. C. Bales. 2012. Elevation-dependent influence of snow accumulation on forest greening. Nature Geosci **5**:705-709.

Viviroli, D., D. R. Archer, W. Buytaert, H. J. Fowler, G. B. Greenwood, A. F. Hamlet, Y. Huang, G. Koboltschnig, M. I. Litaor, J. I. Lopez-Moreno, S. Lorentz, B. Schadler, H. Schreier, K. Schwaiger, M. Vuille, and R. Woods. 2011. Climate change and mountain water resources: overview and recommendations for research, management and policy. Hydrology and Earth System Sciences **15**:471-504.

White, A. B., D. J. Gottas, F. M. Ralph, and P. J. Neiman. 2003. Operational bright-band snow level detection using Doppler radar.*in* U. S. P. a. T. Office, editor.

White, A. B., D. J. Gottas, A. F. Henkel, P. J. Neiman, F. M. Ralph, and S. I. Gutman. 2009. Developing a Performance Measure for Snow-Level Forecasts. Journal of Hydrometeorology **11**:739-753.

White, A. B., P. J. Neiman, F. M. Ralph, D. E. Kingsmill, and P. O. G. Persson. 2003. Coastal orographic rainfall processes observed by radar during the California Land-Falling Jets Experiment. Journal of Hydrometeorology **4**:264-282.

Winstral, A., K. Elder, and R. E. Davis. 2002. Spatial snow modeling of wind-redistributed snow using terrain-based parameters. Journal of Hydrometeorology **3**:524-538.

Xiaoye, L. 2008. Airborne LiDAR for DEM generation: some critical issues. Progress in Physical Geography **32**:31-49.

Zhang, K., and Z. Cui. 2007. Airborne LiDAR data processing and analysis tools - ALDPAT 1.0. . International Hurricane Research Centre, Department of Environmental Studies, Florida International University, Miami, FL.

Table 1. Target parameters and attributes for LiDAR flights

Flight parameters		Instrument attributes	
altitude AGL	600 m	wavelength	1064 nm
flight speed	65 m sec^{-1}	beam divergence	0.25 mrad
swath width	233.62 m	laser PRF	100 kHz
swath overlap	50%	scan frequency	55 Hz
point density	10.27 m^{2}	scan angle	$\pm$ 14°
cross track res.	0.233 m	scan cutoff	3°
down track res.	0.418 m	scan offset	0°

Table 2. Regression of residuals with I_A

Elevation, m	r^2 /intercept/slope[a]			
	North	Northwest	Southwest	West
1850-2050	0.32/-23/124	0.22/-26.4/74.3	***0.34/2.0/-531.4***	0.14/-28/81
2051-3300	0.22/1/102	***0.42/-10/134***	0.00/3/10	0.37/-15/160
3301-3494	0/-68/-260	0.08/-72/594	***0.32/-105/1625***	0.25/-91/1028

[a]All $p < 0.001$, with exception of north at 3301-3494 m and southwest at 2051-3300 m.

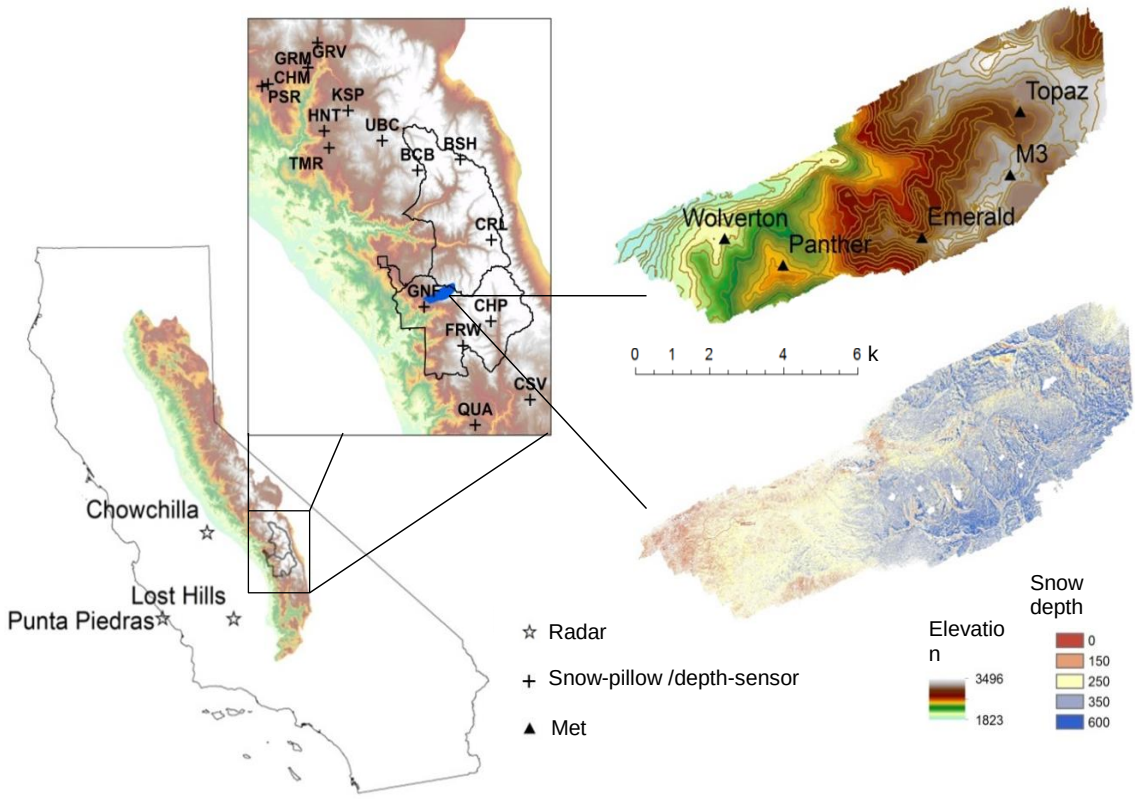

Figure 1. Study area, instrument locations and snow depth. Lower left shows California with Sierra Nevada, outline of Sequoia and Kings Canyon National Parks and location of radar stations. Inset shows LiDAR footprint and location of snow-depth sensors and snow pillows. Upper right shows elevation and 50-m contour map with locations of met stations (Case Mountain, 5 km southwest, and Giant Forest, 900 m southwest, not shown). Bottom right is LiDAR measured 1-m mean snow depth in areas free of vegetation; legend shows lower cut-off values. Snow-pillow sites shown are, from north to south: Graveyard Meadow (GRV), Green Mountain, Chilkoot Meadow (CHM), Poison Ridge (PSR), Kaiser Pass (KSP), Huntington Lake (HNT), Upper Burnt Corral (UBC), Tamarack Summit (TMR), Bishop Pass (BSH), Black Cap Basin (BCB), Charlotte Lake (CRL), Giant Forest (GNF), Chagoopa Plateau (CHP), Farewell Gap (FRW), Casa Vieja (CSV), Quaking Aspen (QUA).

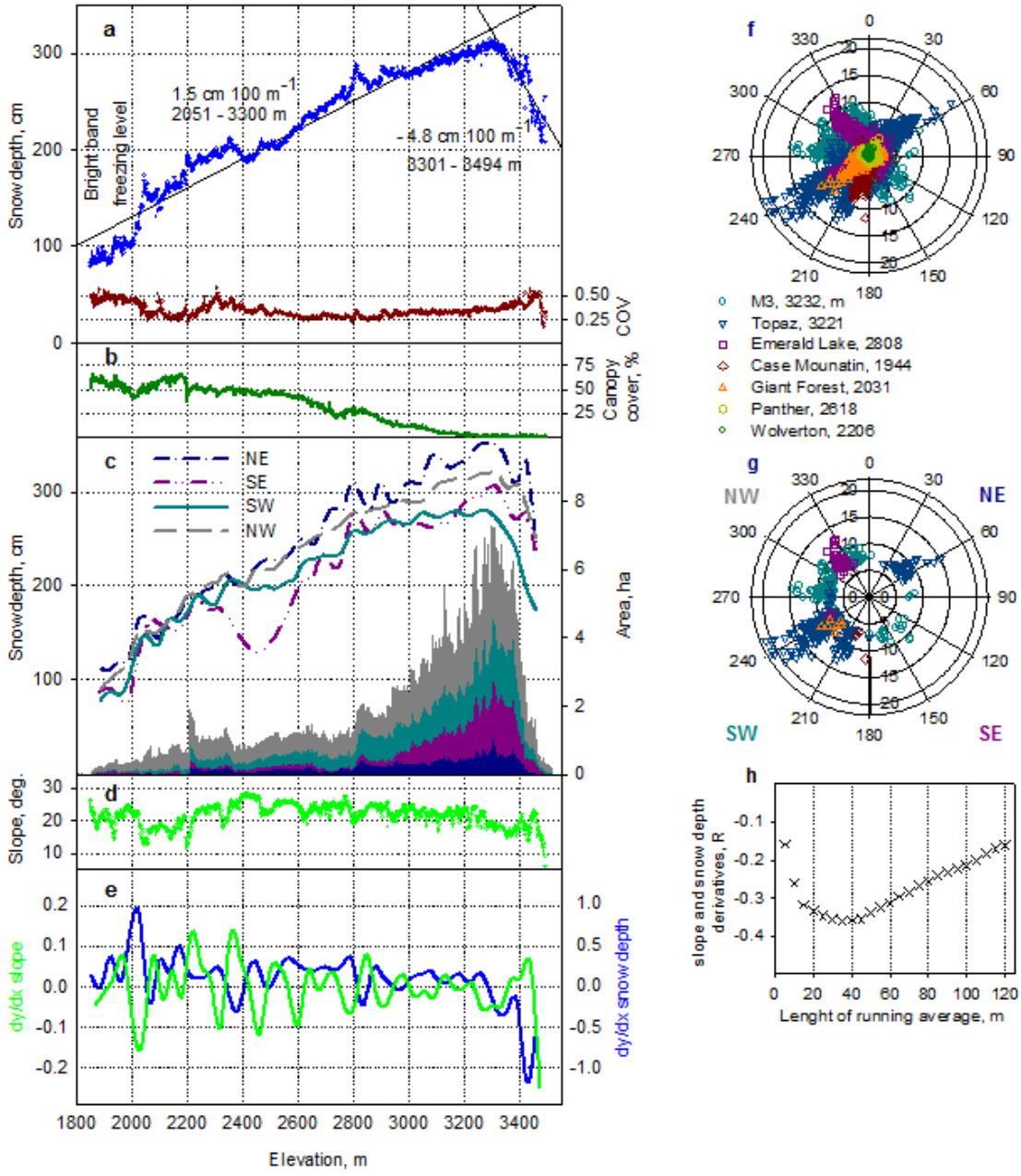

Figure 2. Left panel shows 1-m elevation band mean of: a) snow depth with regression lines with upper quartile of Chowchilla bright band radar freezing level at 2068 m, and snow depth coefficient of variation, b) percent canopy cover, c) 35-m running average of mean snow depth and stacked area by elevation for each 90^{o} quadrant, d) terrain slope, and e) first derivative of mean slope (green) and snow depth (blue) over 35-m running average. Right panel shows: f) hourly average wind speed and direction for accumulation period (top) and periods with highest probability of snow redistribution (bottom), with radius scale in m sec^{-1}, azimuth in degrees, and g) correlation coefficient between the first derivative of slope and the first derivative of snow depth for averaging intervals of 5-100 m of elevation all $p < 0.001$.

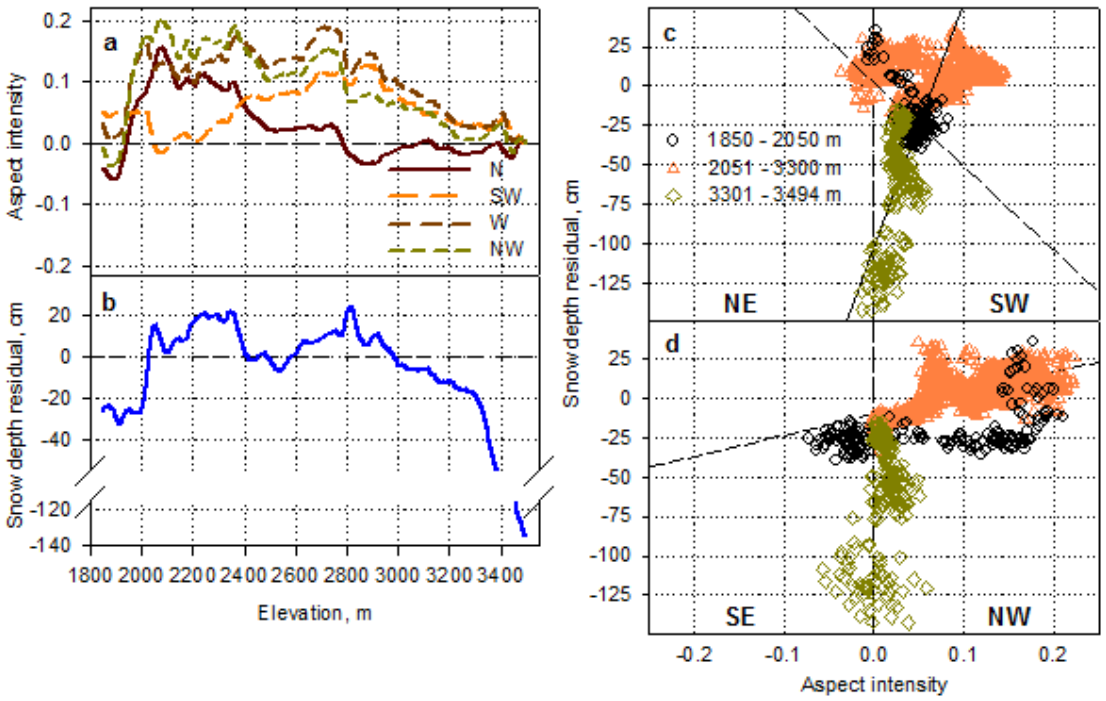

Figure 3. a) Aspect intensity, b) residuals of mean snow from 1850-3300 m regression line (from Figure 2a), and c) regression of residuals for lower middle and upper elevations showing aspect and slope dependent departures from elevation trend.

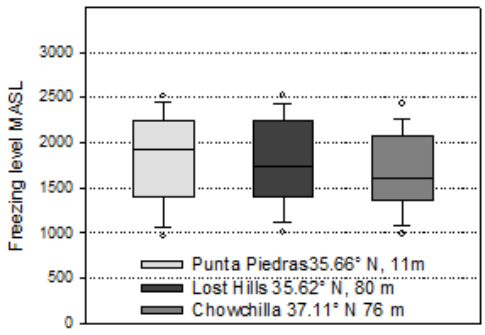

Figure 4. Data distribution for the seasonal-accumulation hourly bright-band freezing level recorded at three wind-profiler stations upwind of the study area, locations shown in Figure 1.

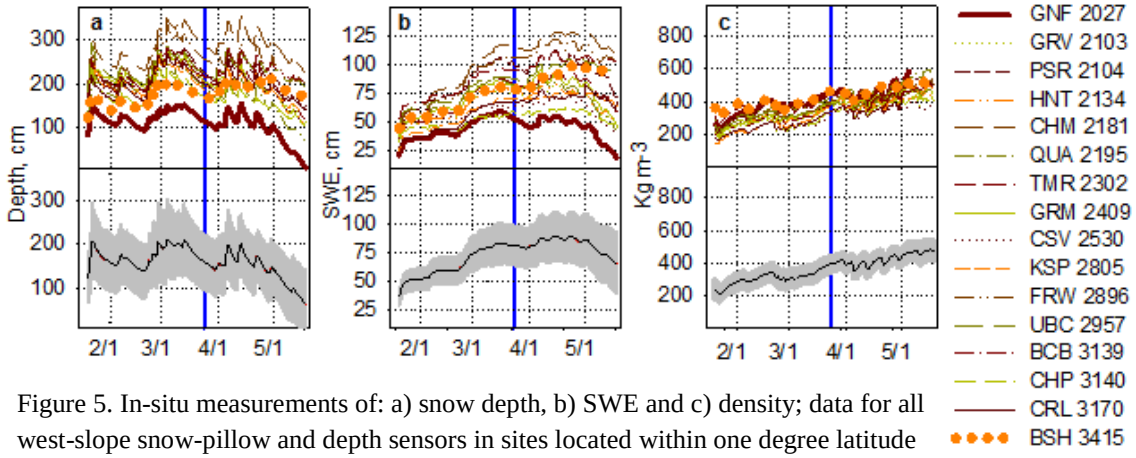

Figure 5. In-situ measurements of: a) snow depth, b) SWE and c) density; data for all west-slope snow-pillow and depth sensors in sites located within one degree latitude of study area. Upper panels show data for individual stations, with highest and lowest elevations plotted in bold. Lower panels show mean in black, with ±1 standard deviation shaded in grey; vertical blue line indicates LiDAR acquisition dates. Figure 1 shows station names and locations.

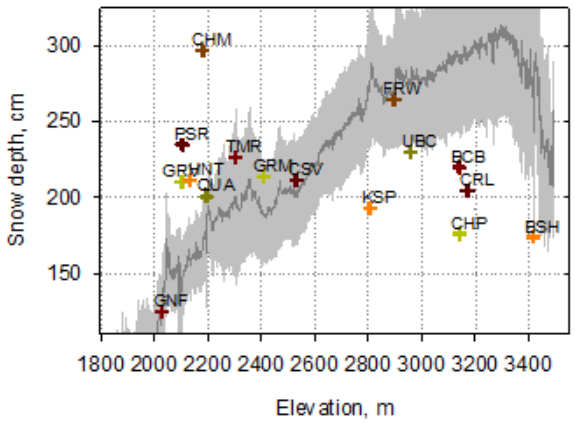

Figure 6. Snow depth on LiDAR acquisition date for all operational west-slope snow-pillow sites equipped with depth sensors, plotted with mean LiDAR snow depth (dark gray) and 1 standard deviation (light gray). Giant Forest (GNF), Farewell Gap (FRW), and Chagoopa Plateau (CHP) are within 21 km of the measurement domain. Chilkoot Meadow (CHM) and Poison Ridge (PSR) are the sites furthest to the northwest. Locations shown on figure 1.

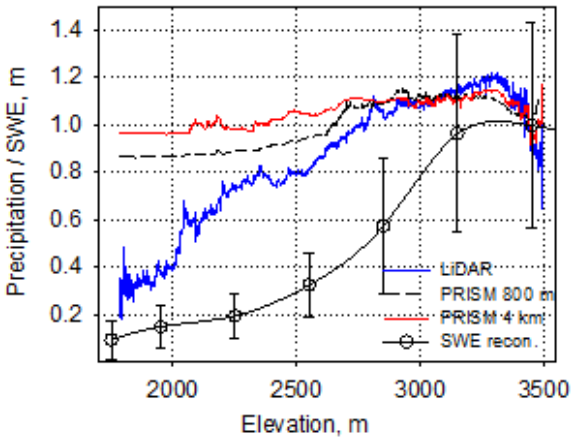

Figure 7. Precipitation and SWE estimates for the Kaweah River watershed, elevation trend for two scales of PRISM precipitation, LiDAR SWE estimate, and SWE reconstructed from daily total snowmelt estimates.

CHAPTER 3

FOREST CANOPY EFFECTS ON SNOW ACCUMULATION FROM LIDAR AND IN-SITU MEASUREMENTS, SIERRA NEVADA, CALIFORNIA

Peter B. Kirchner, Sierra Nevada Research Institute, UC Merced, CA and Joint Institute for Regional Earth System Science and Engineering, UC Los Angeles, CA[a]

Roger C. Bales, Sierra Nevada Research Institute, UC Merced, CA

Keith Musselman, Centre for Hydrology, University of Saskatchewan, SK

Noah P. Molotch, Department of Geography and the Institute of Arctic and Alpine Research, University of Colorado at Boulder, CO. and Jet Propulsion Laboratory, California Institute of Technology, CA

[a]Contact information for corresponding author:
Peter B. Kirchner
Joint Institute for Regional Earth System Science and Engineering
pkirchner@ucmerced.edu

keywords: hydrology, forest, snow, SWE, LiDAR, Sierra Nevada

Abstract

We estimated under-canopy snow depth across a 53-km^2 study area with a variety forest types using seven LiDAR derived and three in-situ canopy metrics. Snow-depth measurements were made with periodic synoptic surveys, continuous snow-depth sensors, and snow depth derived from LiDAR altimetry near the time of peak accumulation. At a resolution of 1 m^2, overall 31-44% of the under-canopy area was measured using the high-point-density LiDAR acquisition. Variability by dominant vegetation type showed 40-100 cm (12-24%) lower snow depth under-canopy versus in the open. The highest variability was in locations subjected to early season ablation or wind redistribution. The metrics of mean canopy height, canopy-to-ground surface ratio, fractional canopy cover, and canopy-height standard deviation individually explained up to half of the variability (R^2 of 0.45-0.58) and slightly more in combination. The under-canopy differences in snow water equivalent early in the snow season were partially offset by 8-15 kg m^{-3} (2-4%) higher snow density at under-canopy locations. However, under-canopy areas shifted to lower snow densities later during snowmelt with locations where radiative forcing is higher, such as south-facing slopes and the south azimuth of trees, having consistently higher snow densities. Although high-density LiDAR can directly measure approximately one third of the under-canopy area, the combination of in-situ measurements and LiDAR-derived canopy models proved effective for obtaining spatially explicit and scalable snow-depth information in Sierra Nevada conifer forests.

1. Introduction

Estimates of mountain snow accumulation are central to forecasting runoff across the Western United States. At present, most Sierra Nevada runoff predictions rely on snow measurements at long-established index sites, e.g. snow courses at mid elevations in openings with minimal forest cover, rather than spatially representative measurements (Rice and Bales 2010). Measurements made in the canopy openings have been found to be biased representations of the snow depth of surrounding forested areas, but serve as a widely used basis for forecasting because of their robust data record through a period of climatic stationarity (Rice et al. 2011, Meromy et al. 2012). However, these statistical forecasts perform better in years closer to the normal, or mean, of the historical record and poorly in years with extremes; and as we enter a period of greater climatic uncertainty we can expect worsening performance and thus greater use of spatially explicit models based on physical processes (Milly et al. 2008). This expected shift toward more process-based models requires improved descriptions of snow dynamics, including the effect of forest canopy (Bales et al. 2006).

Satellite remote-sensing observations can provide daily estimates of snow covered area, and together with spatially representative ground-based measurements, can serve as a basis for accurate forecasts snowmelt across a river basin (Bales et al. 2008). These observations are most reliable at high elevations with little or no forest cover, and with close-to-nadir view angles (Liu et al. 2008, Molotch and Margulis 2008). However, much of the Sierra Nevada's snow-covered area is found under forest canopy where few reliable measurements are made. Measurements are needed at multiple scales in snow-covered forests because there are significant differences in snow accumulation and melt between open and under-canopy locations, due to interception of falling snow by trees and the effect of canopy on the energy available for melting snow (Bales et al. 2011b). The effect of forest vegetation on snow accumulation, ablation and ultimately watershed discharge, has been the subject of research in the forests of the interior and Pacific Northwest of North America (Berris and Harr 1987, Pomeroy and Dion 1996, Hedstrom and Pomeroy 1998, Essery and Pomeroy 2001, Storck et al. 2002, Andreadis et al. 2009, Jost et al. 2009, Varhola et al. 2010, Molotch et al. 2011). However, these topics remain

largely unstudied in the extensive snow-covered forests of the Sierra Nevada. With growing pressures on land managers to address water-related ecosystem services, there is renewed interest in understanding the impacts of disturbance and forest management on snow and its subsequent contribution to water yield from forested landscapes (Westerling et al. 2006, Bales et al. 2011a, Boon 2011).

The relationship between forest gaps and snow accumulation was first recognized in the Sierra Nevada and published by Church (1912b) and the first comprehensive study on snow properties in Sierra forests was published by Kittredge (1953). Research on the potential of forests to attenuate melt and prolong discharge was later conducted by Anderson (1963) and more-recent research in the Sierra Nevada has addressed observations and modeling of the energetics of ablation (Musselman et al. 2012a, Musselman et al. 2012b, Yatheendradas et al. 2012).

While some measurements of interception have been made and reported in the literature, they have generally been limited to a single or small subset of trees (Lundberg and Halldin 2001, Storck et al. 2002, Essery et al. 2003, Floyd and Weiler 2008, Musselman et al. 2008). Up scaling of these measurements to forest stands or watersheds is generally done using indirect measurements of leaf area index. Now with increased availability of high-resolution LiDAR altimetry from snow-accumulating landscapes it is possible to evaluate direct measurements of forest-canopy metrics to predict the effect of canopy on snow accumulation. Researchers have begun to do this by building on the use of canopy closure measured in situ with hemispherical photographs and remote-sensing data from multiple platforms (Teti 2003, Varhola et al. 2010, Varhola et al. 2013).

In assessing snow accumulation, it is important to consider both snow depth and density measurements, given that both LiDAR and low-cost ground-based sensor networks that are being introduced measure snow depth rather than SWE (Welch et al., 2013). At the scale of river basins and operational forecasts, these types of spatially extensive measurements will continue to rely on less-extensive measurements of density at more-traditional, operational sites or through synoptic surveys. Research reported in this paper addresses the effects of canopy cover in Sierra Nevada conifer forests on snow depth and density, from plot to watershed scales. We addressed three specific questions.

First, what is the predictive capability of LiDAR-measured canopy characteristics for observed patterns of snow accumulation in mixed-conifer and sub alpine forests? Second, how does under-canopy snow density vary between open areas versus under the forest canopy? Third, how can we make accurate estimates of under-canopy SWE based on canopy metrics and density measurements made in various canopy conditions?

2. Methods

In this research we used multiple sets of measurements in a mountain study area including: i) a summer 2010 LiDAR flight for ground and canopy-surface altimetry, and an early spring 2010 LiDAR flight to estimate snow depth across the study domain, ii) continuous snow-depth, manual snow-density and continuous soil-moisture measurements at 26 nodes for water years 2008 through 2011, iii) LAI-2000, hemispherical photography and other ground measurements to characterize the forest canopy at these 26 nodes, iv) early April manual snow surveys for snow depth, density and water equivalent in 2007, 2008 and 2009 in the vicinity of these 26 nodes, and v) operational snow-course data.

2.1. Study area

Our study area is centered at approximately 36.5° latitude in the southeastern part of the 135 km^2 Marble Fork of the Kaweah River watershed in Sequoia National Park, and is defined by the extent of the two LiDAR flights (Figure 1). The approximately 53 km^2 area of the LiDAR flights covers Giant Sequoia groves at the lowest elevations, through mixed-conifer forest, to red-fir forest, subalpine forest and alpine peaks at the highest elevations (1850-3494 m elevation range). Areas of synoptic and instrumental surveys include the forested Wolverton watershed located in the lower half of the LiDAR extent (2150- 2900 m elevation). In this watershed there are four instrument clusters and two met stations stratified by aspect and elevation in addition to a grid of 600 × 600 m around an operational snow course where synoptic snow surveys were conducted (Figure 1).

2.2. LiDAR data

LiDAR altimetry, with return density of approximately 8 m^{-2}, was collected in March and August of WY 2010. We represented the bare earth, snow on and off, and canopy with a 1-m grid, as this is the smallest area that matches the beam sampling resolution and uncertainty in horizontal accuracy. The filtered mean values from the snow-on and snow-off acquisitions were subtracted to obtain snow depths from locations where returns for snow depth were ≥1 m^{-2}, as described in chapter 2. A 1-m gridded digital surface model of the vegetation canopy, created from the filtered first-return LiDAR point cloud, was used to create a layer of vegetation canopy ≥ 2 m. Under-canopy snow depths were distinguished from those in gaps by classifying the snow depths using this canopy-height model (Figure 2). The visible under-canopy area is defined here as locations with filtered LiDAR ground-return densities ≥1 m^{-2} for snow on and off thus, only grid points with filtered LiDAR returns for both flights are considered in our analysis.

Using the canopy-height model, for each snow-sensor node we calculated the percent canopy cover, and the maximum, mean, standard deviation and coefficient of variation of canopy height, for 2 to 40 m radii at 1-m intervals. Two meters was chosen as a starting radius because the maximum integrating area of our depth-sensor arrangement, described below, is greater than 1 m. The distance to the nearest canopy ≥2 m in height, subsequently referred to as minimum gap radius, was also determined from canopy-radius estimates generated in this step and represent the shortest distance to canopy ≥2 m at each node. In addition, a 1-m triangular irregular network of the canopy surface was calculated to estimate the canopy surface area for each radius of the calculation. Using the LiDAR-derived bare-earth digital-elevation model we derived the mean slope for the area defined by each radius, and the canopy-to-ground surface-area ratio:

$$CSR = {A_c}\Big/{\frac{A_g}{cos_{slp}}} \quad (1)$$

where A_c is the canopy surface area, A_g is the ground surface area and cos_{slp} is the cosine of the mean slope.

2.3. Other vegetation characteristics

We estimated canopy closure at each sensor node using hemispheric digital photographs taken with a high-resolution digital camera equipped with a ~170° view lens, henceforth referred to as hemiphotos. These images were processed using Gap Light Analyzer software following the methods described in Mussleman et al. (2012a) (Appendix C). The result is an integrated value of the Sky View Fraction (SVF), at 1° increments at each snow-depth sensor, 1.5 m above ground.

Effective Leaf Area Index (LAI^e) was estimated with two of the most-common methods, by measuring radiation transmittance from a fractional sky view. The first was estimated from hemiphotos, collected as described above, using the methods described by Norman and Campbell (1989) and accounting for a sloped surface as described by Schleppi et al. (2007). The second used an average of 8 measurements collected at each node with Licor LAI-2000 plant-canopy analyzer and processed using a radiative-transfer model based on uniform canopy assumptions, as described in Chen et al (1997).

Forest types were classified using vegetation maps prepared from photointerpretation of digital orthophotos and validated with extensive field data and based on the United States, National Vegetation Classification Standard (1994) (Appendix D). Forest types are reported here by common name of the dominant tree species in the associated floristic alliance described by this standard and documented by (USGS-NPS 2007). To estimate the non-accumulating area under the canopy occupied by the trunk or "stem" of these dominant species we compiled field measurements of canopy cover and basal-area estimates proximal to our study area (Table 1) (Rundel et al. 1977, Vankat and Major 1978, Battles et al. 2013). Measurements made in forest study plots and belt transects were assumed to be representative of forest types. The fraction of stem area for species is:

$$SA_x = \frac{\mu BA_x}{CC} \tag{2}$$

where μBA is the mean basal area, measured as diameter at breast height, of species x and CC is fractional canopy cover. Where belt transect surveys reported canopy cover >1 due to crown overlap, CC was set to 1 (Table 1).

2.4. In-situ snow measurements

Synoptic snow surveys in a 600 × 600 m area were conducted within 4 days of April 1 in 3 years, 2007-2009, using a federal snow sampler. Depth and density were measured under tree canopies at 36 grid points, four individual measurements, one for each cardinal direction, 1 m from the nearest tree trunk >30 cm diameter at breast height and 3-4 times in the closest forest-gap >2 m from overhead canopy. Additionally, snow depth, SWE and density were measured 6-8 times in March-June 2010 and March-May in 2011 at 3-6 of the continually recording snow-depth sensor nodes. These sensors were installed under mature forest canopy and stratified as: a) under-canopy, canopy directly overhead; b) open, in a forest-gap at least 2 m from the canopy edge and; c) drip edge, under the canopy edge.

Snow density was determined from gravimetric measurements made in snow pits and standard measurement methods using snow tubes (Church 1912a). Records of mean snow depth and density were also obtained for the Panther Meadow California Cooperative Snow Survey course for 89 years from the California Data Exchange Center (http://cdec.water.ca.gov/snow/); and data for individual snow-course points were compiled from survey notes for the 2007-2011 water years supplied by cooperators. We multiplied snow-tube measurements by a correction factor of 0.9, as determined through comparison with densities in snow pits that were excavated each year at a single location within our sampling grid and sampled at 10-cm intervals. This correction agrees closely with the value of 0.91 determined from other comprehensive gravimetric analysis of the standard federal sampler (Goodison 1978, Farnes et al. 1983). All grid points and sensors were located using a hand held Trimble® GeoXT GNSS receiver mounted with an external Tornado antennae, and post processed to within 1-3 m accuracy to facilitate re-locating grid points and spatial analysis of gathered data (Trimble Navigation Limited, Sunnyvale, CA).

Each node was equipped with an ultrasonic snow-depth sensor, which operates based on the air temperature-corrected return time of an ultrasonic reflectance at a beam width of 22° (Judd Communications, Salt Lake City, UT). There are six sensors at each instrument cluster and one at each met station, mounted with a 4.6-m mast and 95-cm

boom normal to the surface. This arrangement results in an effective observation area of 2.5 m^2. However, the area of observation (A_{obs}) for ultrasonic sensors, mounted as described, becomes smaller with increasing snow depth

$$A_{obs} = \pi[(\tan 11) \times (4.6 - d)]^2 \quad (3)$$

where d is the snow depth observed by the sensor.

Recognized sources of error in ultrasonic depth sensors include instrument error, atmospheric conditions during measurements (e.g. heavy snowfall and riming conditions), boom misalignment due to snow loading and creep that affects the resulting beam angle, snow depth variability within the observation area and variability of ground-cover height due to litter fall and compaction after wetting and loading with seasonal snow. To estimate error we averaged 2-4 manual depth measurements collected under each sensor 2-5 times per water year and compared them to sensor measurements. The resulting RMSE was 10 cm. Hourly snow depths were filtered for erroneous values and gaps less than 6 hours filled by interpolation, or by correlation with the nearest sensor when greater than 6 hours (Moffat et al. 2007). One extreme snowfall event in April 2011 required extrapolation from neighboring sensors when snow depth exceeded some sensor heights. Hourly derivatives of snow depth were calculated to allow separation between accumulation and ablation events. Four major snowfall precipitation events were selected for each of the five years, approximately one in each month December-May, where the majority of the 26 sensors recorded accumulation. Cumulative totals were calculated for each sensor. Sensor nodes were stratified by high and low elevation, separated approximately 400 m in elevation, for a total of 13 sensors from two clusters and one met station at each elevation (Figure 1). The maximum depth from each storm was used to normalize the remaining depth of each sensor to a fraction of maximum. These fractional accumulations were used for analysis with canopy variables.

2.5. Data analysis

To determine which attributes, individually or in combination, had the greatest predictive ability for snow accumulation we conducted linear regression analysis using the canopy variables described in sections 2.2 and 2.3. These included the six LiDAR-derived canopy variables extracted for radii of 2-20 m (9880), integrated SVF for 0-40° (2050), the two estimates of LAI (920) and gap radius (520), where the numbers in parenthesis indicate the number of observations of each variable.

To determine the optimal model we used the six LiDAR-derived canopy variables at radii with the highest predictive power to conduct backwards stepwise regression for the mean snow accumulation of all 20 precipitation events. When selecting independent variables for inclusion or elimination we gave preference to those with the greatest coefficient of determination that demonstrated statistically significant $p < 0.05$ regressions with the greatest number of snowfall events.

We tested our models with a leave-one-out cross validation using the relative accumulation at each node from a single snowfall as validation data, and the remaining accumulation values as the training data. We repeated this procedure for each of the 20 precipitation events until each event was used once as validation data. Finally, the results of all rounds of validation for each model were averaged and compared to determine those with the greatest predictive power.

3. Results

3.1. LiDAR-measured snow depth

Under-canopy snow depth showed distinct patterns between elevation, aspect and forest type (Figure 2). Mean snow depth in the open and under-canopy each demonstrated a steady increase with elevation until approximately 3300 m for the open and 2900 m under-canopy, with the highest covariance below 2100 m, and at the highest elevations (Figure 3a). The fractional canopy cover was 0.45-0.70 below 2600 m, dropping to <0.1 by 3100 m. The fraction of total area with under-canopy LiDAR snow depth retrievals was also greatest below 2600 m, where it remained fairly consistent at 0.18-0.23 (Figure 3b). Below about 2900 m, average under-canopy snow depths were 20-40 cm below

those in the open, increasing to a 100-cm difference at the upper-elevation canopy. Overall, snow depth under the canopy was 12-24% below that in the open, with a coefficient of variation of 0.20-0.42 (Figure 4).

LiDAR-derived snow depths were retrieved from 39% of the total 12 km^2 of under-canopy area, with a range of 31-44% depending on forest type, classified by the dominant species of the corresponding forest alliance (USGS-NPS 2007). Vegetation alliances used in our analysis are listed in parenthesis after each species name. The Western White Pine (*P. monticola*; 3130, 4540) association had the highest fraction of under-canopy retrievals and the Giant Sequoia (S. gigantium; 4020) the least (Figure 4). Classified forests were in fairly contiguous domains, with the exception of Sierra Lodgepole (*P. contorta* var. *murrayana*, 3020), and demonstrated distinct characteristics with respect to under-canopy snow depth. Red fir (*A. magnifica*; 4050) and White fir (*A. concolor*; 4070, 4080) associations were greatest in area with 536 and 318 ha, respectively; all others range from 11 to 86 ha. The greatest coefficients of variation were found with the Jeffry pine (*P. jeffreyi*; 3070) and White fir associations, where some under-canopy melt had likely already occurred, and in the highest-elevation forest association of Foxtail Pines (*P. balfouriana*; 3200, 3540), where wind likely redistributed snow through the small open stands.

The fraction of under-canopy area occupied by the stem, or "trunk", of the tree, that does not accumulate snow, was estimated to range between 0.005, for Ponderosa (*P. ponderosa*) and Jeffry pine, to 0.013, for Giant Sequoia forests (Table 1, Appendix D).

3.2. Snowfall accumulation at sensor nodes

The 20 precipitation events selected for this study were largely prior to snowmelt, with 4 during the early part of snowmelt (Figure 5). They ranged in duration from 5 to 14 hours. The period of record represented dry, normal and wet years, where peak mean snow depth for all sensors in the 2008-2011 water years had a range of 174 cm in 2009 to 392 cm in 2011; these depths were 73 % and 165% of the 30-year-April 1st mean from the Panther Meadow snow course, located between clusters 3 and 4, and within the domain of the grid surveys. Peak snow depth occurred prior to April 1st in 2008 and 2009,

after in 2010 and near April 1st in 2011. The 2010 spring LiDAR acquisition occurred during a settling period, between two precipitation events and just prior to the peak seasonal depth accumulation.

3.3. LiDAR and in-situ canopy characteristics

Node-specific canopy characteristics extracted from the LiDAR data, calculated for radii of 2-40 m around each of the 26 snow-depth sensors, showed the greatest variability between 2 and 20 m (Figure 6). We chose the 2-20 m range of radii to evaluate with mean snow accumulation for all precipitation events, because LiDAR-derived variables demonstrated at least twice the variability at radii <20 m and overlapped less with the corresponding radii of other sensors in the cluster. The minimum distance to canopy >2 m in height was 2-10 m horizontally, where distances $\leq$2 m comprised half of the 26 measurements (Figure 6).

In-situ measurements of canopy closure and effective LAI were made 1.5 m above the ground at 25 and 23 nodes, respectively. Canopy closure from hemiphotos integrated at zenith angles of 0-40° showed significant variability between nodes, e.g. sensor 1_1 and 1_5 (Figure 7a, Appendix C). Sensor nodes 1_1, 1_3, 3_6 and 4_5 had the greatest canopy cover over them, and thus the lowest SVF, and sensors 1_5, 2_5, 3_2 and 3_4 the lowest canopy cover and highest SVF. The integrating zenith angle at each node showed considerable variability as well, with a range >50% in some cases. Mean fractional accumulation demonstrated approximately 1:3 scaling ratio with SVF with 4 exceptions (Figure 7b). Effective LAI, measured using two methods, hemispherical photographs and the Licor LAI-2000, differed significantly in magnitude between the two methods but showed a positive correlation, (R^2 = 0.38, p 0.002) (Figures 7c and d).

3.4. Snow depth and SWE

Comparisons of 2007-2009 synoptic surveys, conducted within 4 days of April 1 from open (10 single snow-course points), forest gaps (104-132 survey points per year), and under-canopy (144 survey points per year) locations showed consistent inter-annual variability (Figure 8). The depth differences between under-canopy and forest-gap

measurements averaged 30-35 cm in all years, despite the nearly double accumulation in 2008 versus 2007. The depth difference between forest-gap and open (snow course) depths averaged 30, 35 and 45 cm in 2007, 2008 and 2009, respectively. The differences in SWE between under-canopy and forest gaps and between forest-gap and open locations averaged 11-14 cm over the 3 years (Figure 8). All of the differences were statistically significant ($p<0.001$).

3.5. Snow density

Mean snow densities in forest gaps and under-canopy were 386 $\pm$60 and 371 $\pm$70 kg m^{-3}, respectively, with slightly lower average densities in the open locations of the snow course (Figure 8). Density differences between these 3 sets of measurements however, were only statistically significant for under-canopy versus forest-gap points in 2009 ($p <0.05$). The coefficient of determination between all forest-gap and under-canopy locations considered for all years was small ($R^2 = 0.19$) but did show a statistical difference ($p = 0.041$). Under-canopy density measurements made 1 m from the tree trunk in the azimuths of north, south, east and west showed the highest densities on the south sides of trunks ($p = 0.019$) (Table 3).

The 2007 snow-course-density values are lower and have a greater range as compared to the 2008-2009 values (Figure 8). Soil moisture measured, at 3-13 locations per year inside the survey area (Appendix F) demonstrated diel melt patterns prior to the survey in 2007 (March 10-27), after the survey in 2008 (April 10 to May 15) and close to the time of the surveys in 2009 (March 25 to April 18), reflecting the thin, variable 2007 snowpack.

The spatial and temporal variability of density at snow-depth sensor nodes in 2010 and 2011 showed a seasonal increase, consistent with the trends observed at nearby snow pillows (Figure 9). The mean of density measurements made during accumulation, prior to March 15th, were 15 kg m^{-3} higher than in the open, which is not significant ($p = 0.17$). In contrast, measurements after March 28 showed 8 kg m^{-3} lower under-canopy densities ($p = 0.20$) (Figure 9). Sensors were also stratified by north versus southeast aspects, and were 38 kg m^{-3} lower on the north aspects ($p<0.001$).

3.6. Regression and modeling.

The highest coefficients of determination between the fractional snow depths for the precipitation events and LiDAR-derived canopy variables were at radii of 8-10 m (Figure 10). The coefficients of determination for SVF demonstrated a broad peak at zenith angles between 2-40°, with the greatest for any event at 16°, and the peak in the highest mean R^2 at about 25^o (R^2 of 0.58) (Figure 10). Due to the broad range in coefficients of determination we chose to use the mean SVF integrated over this range of zenith angles to compare with fractional accumulation (Figures 7b and 11). Mean canopy height, standard deviation, CSR and fractional canopy cover each explained close to half of the variability (Table 2). The single-node variables of both LAI measurements and minimum gap radius were the lowest, with R^2 of 0.25-0.31.

Regression of variables with all storm events showed considerable variation, where mean canopy height, fractional canopy cover, CSR, mean SVF, and minimum gap distance all showed consistent slopes for each storm (Figure 11). Regression of the radius-dependent canopy variables and other attributes versus the fractional snow depth at each of the 20 nodes, with values at each node averaged over the 20 precipitation events, gave R^2 of 0.25-0.58, $p<0.001$ to 0.01 (Table 2) For the LiDAR-derived canopy variables, the highest R^2 values were at radii of 8-10 m. For all variables, it was found that 11-17 of the 26 nodes were significant at $p <0.05$.

Backwards stepwise regression with the fractional means of all precipitation events and LiDAR canopy variables indicated that the most-robust single or multiple-variable regression models included the mean canopy height at 8, 9 or 10 m radii. Multiple regression models with the variables of percent canopy cover, standard deviation of canopy height, and CSR at 8, 9 or 10 m radius slightly improved the coefficient of determination by up to .06 and slightly reduced standard error. The LiDAR-derived canopy variables of maximum canopy height and coefficient of variation, and the in-situ measurements of two effective LAI's showed the lowest regression coefficients and were not included in models. Due to sample sizes and covariance, multicollinearity existed between some variables, for this reason we only selected

variables known to be independent for model inclusion (eg. standard deviation and mean canopy height).

4. Discussion

4.1. LiDAR snow depth

Our methods for classifying under-canopy snow depth using LiDAR altimetry yield direct information in locations where return pulses can be recorded (Figures 2 and 3). However, in our data set less than half of the under-canopy area met these criteria (Figures 3 and 4). We found a 12-24% depth reduction, when compared to canopy gaps, in locations where LiDAR returns were available and expect less snow accumulation under the densest areas of the canopy where no LiDAR returns are available. Thus, we expect this percentage to be lower when considering the total under-canopy area. In the mixed-conifer zone, this represents a 40-cm difference, similar to that observed using continuous depth sensors in the southern Sierra Nevada (Appendix E). Past research has demonstrated the negative correlation between canopy cover and snow accumulation, and typically estimated as a percent reduction referred to as interception efficiency (Schmidt and Gluns 1991, Hedstrom and Pomeroy 1998, Pomeroy et al. 1998a, Storck et al. 1999, Storck et al. 2002, Musselman et al. 2008).

Canopy-surface-area metrics, for quantifying forest structure, have also been identified and named for various purposes. Some examples of these are: roughness, for quantifying canopy effect on atmospheric turbulence Leonard and Federer, (1973); rugosity (standard deviation), to deduce stand development Parker (2004); and rumple to characterize successional stage through the structural complexity of forest canopy (Kane et al. 2010). While each of these methods, and others referred to by Parker and Kane in the above citations, use different metrics to quantify the canopy surface, when coupled with spatial extent, they describe the relationship between the ground and canopy surface area. As a result, each of these measurement methods is subject to scaling uncertainties and limited by its resolution and spatial extent.

Our measurement of CSR is calculated similarly to rumple as defined by Kane (2010) but accounts for greater ground surface area by considering slope, and our

measurement of standard deviation is defined as rugosity by Parker. However, both of these measurements are derived using different spatial extents and granularity.
Snow interception on 3 conifer species was measured and estimated by Schmidt and Gluns (1991) to be 10-50%, primarily dependent on the amount and density of the falling snow and not on leaf morphology. Research in the boreal forests of Canada found that up to 60% of seasonally accumulated snow was intercepted, reaching a species-dependent maximal loading where subsequently up to half of the intercepted snow was sublimated (Pomeroy et al. 1998b). These two examples approximate the range of published interception efficiencies. This process has been characterized as a function of leaf morphology and species specific unloading characteristics of the canopy, coupled with new snow density, the rate of snowfall and the prevailing meteorologic conditions (Hedstrom and Pomeroy 1998).

We expected the variables that most accurately describe the canopy-to-ground surface-area ratio to perform best in single and multiple regressions with relative accumulation. However, the best indicator was not our calculated variable of CSR but mean canopy height and standard deviation of canopy height, followed by CSR and percent canopy cover calculated over radii of 8-12 m from the point of measurement (Table 2, Figure 11). We suspect this is because our mean–canopy-height measurement is the best integrator of canopy surface area and the intra-canopy effects of turbulence on the trajectory of falling snow as it passes through and around the forest canopy.

4.2. Snow depth and SVF

Zenith angles of SVF represent the integrated fraction of sky hemisphere visible at each sensor location. Lower, closer-to-nadir zenith angles are more representative of planer measurement of fractional canopy cover, where higher angles incorporate lateral vegetation and terrain elements (Figure 7a). Hence, we expected more snow to accumulate in locations with greater SVF at lower zenith angles. In the forests of British Columbia, Teti (2003) found zenith angles of 60-80° to be most effective for predicting peak SWE, the product of accumulation and ablation. Further investigations by Varhola (2013) found 45° to be the best predictor of ablation rates. Furthermore, Varhola found

good agreement ($R^2 > 0.6$) between hemiphoto SVF and SVF derived by transforming airborne LiDAR returns to polar coordinates.

Due to lower canopy cover the zenith angles at which SVF has the greatest impact on accumulation should estimate the factors impacting interception efficiency: LAI, canopy density, gap structure, canopy height, and height to canopy base. However, we did not find a discrete relationship between a particular zenith angle integration of SVF and mean fractional accumulation of snow. Instead, we found the highest correlation at zenith angles <40°, with results varying between individual storms, suggesting the influence of factors other than canopy structure such as prevailing weather conditions. The apparent scaling ratio of mean SVF at zenith angles of 1-40° to fractional snow accumulation at individual sensors, seen in figure 7 b, is confirmed by the regression slope of 0.35 shown in figure 11 suggesting an interception efficiency of 35 % slightly lower than findings from the forests of New Mexico (Musselman et al. 2008).

4.3. Forest-stand snow depth, SWE and density

With April 1st synoptic surveys we found the greatest snow depths and SWE in the open snow-course locations and the lowest under-canopy, with forest-gap locations falling in between (Figure 8). The clustering of densities also demonstrated the effect of the final stages of melt on snow density, where water year 2007, the shallowest and earliest melting snowpack of the study period, had the lowest density and widest range of variance. This was likely a result of the advanced melt in some places, as indicated by diel patterns of water flux passing through the soil column, recorded 3 to 5 weeks earlier by soil-moisture sensors collocated with the snow-depth sensors (Appendix F). Densification of the snowpack occurs principally through two processes: i) those affecting porosity, i.e. gravitational settling and metamorphism through crystal sintering and vapor flux, and ii) energetic processes that affect crystal structure and increased liquid-water content (Gray and Male 2004, DeWalle and Rango 2008). The greatest increase in density occurs when the snowpack becomes isothermal and pore space is sufficiently small to retain water between the snow granules. This stage is often referred to as a “ripe” snowpack and precedes daily cycles of melting and freezing. Followed by a

final stage where a shallow snowpack of large granular crystals holds limited liquid water and decreases in density. Thus, we expect to find densities proportional to the cold content of the snowpack in a particular location until the final stages of melt, when density will decrease.

Variability in SWE, the product of snow depth and density, is disproportionately influenced by the heterogeneous distribution of depth rather than the more-homogeneous density (Steppuhn 1976, Sturm and Benson 2004, Sturm et al. 2010). Despite the spatially conservative nature of density it can be affected on small scales by forest canopy through unloading of canopy-held snow and snow melt, (Berris and Harr 1987, Storck et al. 2002) and mediation of the energy budget (Pomeroy and Dion 1996, Pomeroy et al. 2008). The processes of canopy unloading, a function of new-snow density and the rate of snowfall, as observed by Schmidt and Gluns (1991), is decoupled from the under-canopy energy budget, where variability is a function of canopy-mediated radiation. Consistent with our findings, Mussleman (2008) found the proximity to the tree trunk to be a significant factor in the density of under-canopy snow, with the highest densities on the south side of the stem (Table 3). The effect of the trunk also leads to greater ablation. For example, Pomeroy et. al. (2009) observed and quantified the increased temperatures of exposed tree trunks due to shortwave extinction and the resulting increased excitance of long-wave radiation from tree stems.

Our findings also suggest that the observed difference in snow density between under-canopy and open locations is small and primarily influenced by radiative forcing versus unloading or canopy drip. Under-canopy snow density was nearly equal between forest gaps and under canopies in pooled data from April 1st surveys and slightly higher (14 kg m^{-3}, $p = 0.07$) at paired under-canopy and forest-gap measurements made at sensor nodes after March 15th (Figure 9). However, periodic measurements collected in the same locations prior to early March showed under-canopy densities to be (15 kg m^{-3}, $p = 0.17$) higher relative to open locations. Kittredge (1953) found seasonal averages of under-canopy snow density to be approximately 5-25 kg m^{-3} higher than open locations, where the smallest differences were found in the highest-elevation Red Fir forests, which were 400-1000 m lower than the forests in our study. The seasonal shift from higher

under-canopy snow density to values nearly equal to those in forest gaps suggests a crossover point, where seasonal mediation of incoming radiation influences the radiative forcing on the snowpack, causing ripening to occur more rapidly in open locations after mid-March. This is likely a result of canopy mediation of incoming short wave radiation as the sun zenith angle rises and less reaches the forest floor (Pomeroy et al. 2008, Ellis et al. 2010a). Further evidence in support of this are measurements at sensor nodes that collectively show higher densities on the southeast than north and northwest aspects, and higher densities on the south side of trees (Table 3).

Thus, reduced depth due to the interception of falling snow and its subsequent loss due to sublimation in the canopy are the main factors in under-canopy SWE reduction, not densification upon redistribution or drip from canopy melt, which appear to have a minor influence on this process in higher-elevation forests. Additionally, the greater variability in under-canopy locations is likely due to a wider range of energy environments. April 1st forest-stand surveys show that under-canopy snow had greater variance and slightly lower density than snow in adjacent forest gaps (Figure 8). While measurements of density at individual trees in mixed-conifer and sub-alpine forests showed no statistical difference between under-canopy, drip-edge and open locations within 2 m of the canopy edge, they did show differences between under-canopy and forest gaps (Figure 9). Further, LAI, the most common metric used for quantifying under-canopy accumulation efficiency, was measured with two frequently used methods (hemispheric photographs and LAI-2000) that utilize sky-view measurements and uniform transfer models. These measurements explained less than a third of snow accumulation variability and showed low correlation with each other (Figure 7d).

4.4. Effective LAI

Because LAI describes the functional relationship between leaf and surface area it is an intuitive variable for describing interception efficiency (Lundberg and Halldin 2001, Keane et al. 2005, Winkler and Moore 2006, Ellis and Pomeroy 2007). While Pueschel et al. (2012) and others, demonstrate progress in addressing the differences between methods of measuring LAI in practice it remains impractical to directly measure or

extrapolate LAI to specific forests using indirect methods of measurement. In our study we found high levels of uncertainty in correlations between snow depth and LAI^e, demonstrating a limited predictive capacity with respect to snow accumulation.
A comparison of effective LAI measurements at 23 snow-depth sensors, using hemispherical photographs and the Licor LAI- 2000, showed a correlation but also a high level of uncertainty and potential positive bias with the hemiphoto method (Figure 7d). Regression analysis with snowfall precipitation events showed a weak relationship for both methods, with the LAI-2000 performing only slightly better than the hemiphoto method, with a mean R^2 of 0.32. Only one precipitation event had an R^2 of over 0.4 ($P<0.05$) (Figure 10). Extrapolating these measurements to greater spatial scales and interpolating them with other measurements, such as NDVI, would further increase uncertainty with respect to snow accumulation patterns.

5. Conclusions

Direct LiDAR measurements with high return densities (e.g. ≥ 8 m^{-2}) and favorable sensor geometry offer the best opportunity for determining snow depth and distribution over multiple scales. While this analysis provides a basis for developing under-canopy snow depth interpolation strategies for repeat measurement campaigns; multiple flights during the snow covered season are costly and may be operationally impractical. In these locations a viable option for determining under-canopy snow depth is to estimate the fraction lost to canopy interception based on measurements of LiDAR-derived canopy metrics and in-situ snow depth.

In the sub-alpine forests of the Sierra Nevada over half of the local variability in snow accumulation can be explained with LiDAR-derived mean canopy height over a 8-10 m radius, and can be improved with the addition of other canopy variables. The standard deviation of canopy height, percent canopy cover, and CSR also show high predictive capability. LAI, used to estimate interception, had limited predictive ability, due in part to the high uncertainty of indirect measurements of LAI.

We found under-canopy snow density to be 2-5% higher than in forest gaps during the accumulation season; however, this pattern shifted during the ablation season

with under-canopy densities being 2-5% less. Snow density was also greater in locations with greater energy influx such as south-east-facing aspects, and the southerly azimuth from tree trunks. While these differences in density were also small, they were consistently positive during the melt season.

The current high uncertainty in SWE under forest canopy can be reduced using a combination of LiDAR canopy structure, snow-depth altimetry and ground-based instrumentation in forests. The best approach for calibrating LiDAR snow-depth altimetry for SWE retrieval in forested landscapes is a strategy that includes snow-depth measurements in the full range of mean canopy heights and canopy surface areas found in the watershed of interest. Locations for measurement can be estimated using the aforementioned classifications and calculations based on high-resolution LiDAR-derived canopy-height models. In contrast, density, which is more spatially conservative than depth, can be best estimated with distributed measurements across a range of anticipated depths and radiative forcings.

Acknowledgements

Research was supported by the National Science Foundation (NSF), through the Southern Sierra Critical Zone Observatory (EAR-0725097) and NSF grants (EAR-0922307, EAR 1141764, EAR 1032295), a fellowship for the first author from the Southern California Edison Company and a seed grant through Lawrence Livermore National Laboratory (6766). Supplemental support was also provided by T. Painter at the Jet Propulsion Laboratory. We also acknowledge the technical assistance from X. Meng.

References

Anderson, H. 1963. Managing California's Snow Zone Lands for Water. Pacific Southwest Forest and Range Experiment Station, Berkeley, CA.

Andreadis, K. M., P. Storck, and D. P. Lettenmaier. 2009. Modeling snow accumulation and ablation processes in forested environments. Water Resources Research **45**:13.

Bales, R., J. Battles, Y. Chen, M. H. Conklin, E. Holst, K. L. O'Hara, P. Saksa, and W. Stewart. 2011a. Forests and Water in the Sierra Nevada: Sierra Nevada Watershed Ecosystem Enhancement Project. 11.1, Sierra Nevada Research Institute, Merced.

Bales, R. C., K. A. Dressler, B. Imam, S. R. Fassnacht, and D. Lampkin. 2008. Fractional snow cover in the Colorado and Rio Grande basins, 1995-2002. Water Resources Research **44**.

Bales, R. C., J. W. Hopmans, A. T. O'Geen, M. Meadows, P. C. Hartsough, P. Kirchner, C. T. Hunsaker, and D. Beaudette. 2011b. Soil Moisture Response to Snowmelt and Rainfall in a Sierra Nevada Mixed-Conifer Forest. Vadose Zone Journal **10**:786-799.

Bales, R. C., N. P. Molotch, T. H. Painter, M. D. Dettinger, R. Rice, and J. Dozier. 2006. Mountain hydrology of the western United States. Water Resources Research **42**.

Battles, J., D. Saah, T. Robards, S. Cousins, R. A. York, and D. Larson. 2013. Intact Forests, Appendix 9 United States Department of the Interior, Three Rivers, California.

Berris, S. N., and R. D. Harr. 1987. Comparative snow accumulation and melt during rainfall in forested and clear-cut plots in the Western Cascades of Oregon. Water Resources Research **23**:135-142.

Boon, S. 2011. Snow accumulation following forest disturbance. Ecohydrology **5**:279-285.

Chen, J. M., P. M. Rich, S. T. Gower, J. M. Norman, and S. Plummer. 1997. Leaf area index of boreal forests: Theory, techniques, and measurements. J. Geophys. Res. **102**:29429-29443.

Church, J. E. 1912a. Description of Mount Rose Snow Sampler. Scientific American Supplement:152-155.

Church, J. E. 1912b. The Progress of Mount Rose Observatory, 1906-1912. Science **36**:796-800.

DeWalle, D. R., and A. Rango. 2008. Principles of Snow Hydrology. Cambridge University Press.

Ellis, C. R., and J. W. Pomeroy. 2007. Estimating sub-canopy shortwave irradiance to melting snow on forested slopes. Hydrological Processes **21**:2581-2593.

Ellis, C. R., J. W. Pomeroy, T. Brown, and J. MacDonald. 2010. Simulation of snow accumulation and melt in needleleaf forest environments. Hydrology and Earth System Sciences Discussions **7**:1033-1072.

Essery, R., and J. Pomeroy. 2001. Sublimation of snow intercepted by coniferous forest canopies in a climate model. Pages 343-347 Soil-Vegetation-Atmosphere Transfer Schemes and Large-Scale Hydrological Models.

Essery, R., J. Pomeroy, J. Parviainen, and P. Storck. 2003. Sublimation of snow from coniferous forests in a climate model. Journal of Climate **16**:1855-1864.

Farnes, P., B. Goddison, N. Peterson, and R. Richards. 1983. Metrication of manual snow sampling equipment. Westrn Snow Conference, Spokane, Wa.

Floyd, W., and M. Weiler. 2008. Measuring snow accumulation and ablation dynamics during rain-on-snow events: innovative measurement techniques. Hydrological Processes **22**:4805-4812.

Goodison, B. E. 1978. Accuracy of Canadian Snow Gauge Measurements. Journal of Applied Meteorology **17**:1542-1548.

Gray, D. M., and D. H. Male. 2004. Handbook of Snow: Principles, Processes, Management and Use. Blackburn Press.

Hedstrom, N. R., and J. W. Pomeroy. 1998. Measurements and modelling of snow interception in the boreal forest. Hydrological Processes **12**:1611-1625.

Jost, G., R. D. Moore, M. Weiler, D. R. Gluns, and Y. Alila. 2009. Use of distributed snow measurements to test and improve a snowmelt model for predicting the effect of forest clear-cutting. Journal of Hydrology **376**:94-106.

Kane, V. R., R. J. McGaughey, J. D. Bakker, R. F. Gersonde, J. A. Lutz, and J. F. Franklin. 2010. Comparisons between field- and LiDAR-based measures of stand structural complexity. Canadian Journal of Forest Research-Revue Canadienne De Recherche Forestiere **40**:761-773.

Keane, R. E., E. D. Reinhardt, J. Scott, K. Gray, and J. Reardon. 2005. Estimating forest canopy bulk density using six indirect methods. Canadian Journal of Forest Research-Revue Canadienne De Recherche Forestiere **35**:724-739.

Kittredge, J. 1953. Influences of forests on snow in the ponderosa-sugar pine-fir zone of the Central Sierra Nevada. Hilgardia **22**:1-96.

Leonard, R. E., and C. A. Federer. 1973. Estimated and Measured Roughness Parameters for a Pine Forest. Journal of Applied Meteorology **12**:302-307.

Liu, J., R. A. Melloh, C. E. Woodcock, R. E. Davis, T. H. Painter, and C. McKenzie. 2008. Modeling the View Angle Dependence of Gap Fractions in Forest Canopies: Implications for Mapping Fractional Snow Cover Using Optical Remote Sensing. Pages 1005-1019.

Lundberg, A., and S. Halldin. 2001. Snow interception evaporation. Review of measurement techniques, processes, and models. Theoretical and Applied Climatology **70**:117-133.

Meromy, L., N. P. Molotch, T. E. Link, S. R. Fassnacht, and R. Rice. 2012. Subgrid variability of snow water equivalent at operational snow stations in the western USA. Hydrological Processes:n/a-n/a.

Milly, P. C. D., J. Betancourt, M. Falkenmark, R. M. Hirsch, Z. W. Kundzewicz, D. P. Lettenmaier, and R. J. Stouffer. 2008. Climate Change: Stationarity Is Dead: Whither Water Management? Science **319**:573-574.

Moffat, A. M., D. Papale, M. Reichstein, D. Y. Hollinger, A. D. Richardson, A. G. Barr, C. Beckstein, B. H. Braswell, G. Churkina, A. R. Desai, E. Falge, J. H. Gove, M. Heimann, D. Hui, A. J. Jarvis, J. Kattge, A. Noormets, and V. J. Stauch. 2007. Comprehensive comparison of gap-filling techniques for eddy covariance net carbon fluxes. Agricultural and Forest Meteorology **147**:209-232.

Molotch, N. P., P. D. Blanken, T. E. Link, D. F. Levia, D. Carlyle-Moses, and T. Tanaka. 2011. Snow: Hydrological and Ecological Feedbacks in Forests

Forest Hydrology and Biogeochemistry. Pages 541-555. Springer Netherlands.

Molotch, N. P., and S. A. Margulis. 2008. Estimating the distribution of snow water equivalent using remotely sensed snow cover data and a spatially distributed snowmelt model: A multi-resolution, multi-sensor comparison. Advances in Water Resources **31**:1503-1514.

Musselman, K. N., N. P. Molotch, and P. D. Brooks. 2008. Effects of vegetation on snow accumulation and ablation in a mid-latitude sub-alpine forest. Hydrological Processes **22**:2767-2776.

Musselman, K. N., N. P. Molotch, S. A. Margulis, P. B. Kirchner, and R. C. Bales. 2012a. Influence of canopy structure and direct beam solar irradiance on snowmelt rates in a mixed conifer forest. Agricultural and Forest Meteorology **161**:46-56.

Musselman, K. N., N. P. Molotch, S. A. Margulis, M. Lehning, and D. Gustafsson. 2012b. Improved snowmelt simulations with a canopy model forced with photo-derived direct beam canopy transmissivity. Water Resour. Res. **48**:W10509.

Norman, J. M., and G. S. Campbell. 1989. Plant Physiological Ecology Field Methods and Instrumentation. Pages 301-325 *in* P. e. al., editor. Canopy structure. Chapman and Hall, London.

Pomeroy, J., A. Rowlands, J. Hardy, T. Link, D. Marks, R. Essery, J. E. Sicart, and C. Ellis. 2008. Spatial Variability of Shortwave Irradiance for Snowmelt in Forests. Journal of Hydrometeorology **9**:1482-1490.

Pomeroy, J. W., and K. Dion. 1996. Winter radiation extinction and reflection in a boreal pine canopy: Measurements and modelling. Hydrological Processes **10**:1591-1608.

Pomeroy, J. W., D. M. Gray, K. R. Shook, B. Toth, R. L. H. Essery, A. Pietroniro, and N. Hedstrom. 1998a. An evaluation of snow accumulation and ablation processes for land surface modelling. Hydrological Processes **12**:2339-2367.

Pomeroy, J. W., D. Marks, T. Link, C. Ellis, J. Hardy, A. Rowlands, and R. Granger. 2009. The impact of coniferous forest temperature on incoming longwave radiation to melting snow. Hydrological Processes **23**:2513-2525.

Pomeroy, J. W., J. Parviainen, N. Hedstrom, and G. D. M. 1998b. Coupled modelling of forest snow interception and sublimation. Hydrological Processes **12**:2317-2337.

Pueschel, P., H. Buddenbaum, and J. Hill. 2012. An efficient approach to standardizing the processing of hemispherical images for the estimation of forest structural attributes. Agricultural and Forest Meteorology **160**:1-13.

Rice, R., and R. C. Bales. 2010. Embedded-sensor network design for snow cover measurements around snow pillow and snow course sites in the Sierra Nevada of California. Water Resour. Res. **46**:WO3537.

Rice, R., R. C. Bales, T. H. Painter, and J. Dozier. 2011. Snow water equivalent along elevation gradients in the Merced and Tuolumne River basins of the Sierra Nevada. Water Resources Research **47**:11.

Rundel, P., D. T. Gordon, and D. J. Parsons. 1977. Montane and Subalpine Vegetation of the Sierra Nevada and Cascade Ranges.*in* M. G. Barbour, editor. Terrestrial Vegetation of California. Wiley-Interscience, New York.

Schleppi, P., M. Conedera, I. Sedivy, and A. Thimonier. 2007. Correcting non-linearity and slope effects in the estimation of the leaf area index of forests from hemispherical photographs. Agricultural and Forest Meteorology **144**:236-242.

Schmidt, R. A., and D. R. Gluns. 1991. Snowfall interception on branches of three conifer species. Canadian Journal of Forest Research-Revue Canadienne De Recherche Forestiere **21**:1262-1269.

Steppuhn, H. 1976. Areal water equivalents for prairie snowcovers by centralized sampling. Pages 63-68 *in* Proceedings 44th Annual Meeting, Western Snow Conference, Calgary, AB.

Storck, P., T. Kern, and S. Bolton. 1999. Measurement of Differences in Snow Accumulation. Melt. and Micrometeorology Due to Forest Harvesting. Nofihwest Science **73**.

Storck, P., D. P. Lettenmaier, and S. M. Bolton. 2002. Measurement of snow interception and canopy effects on snow accumulation and melt in a mountainous maritime climate, Oregon, United States. Water Resources Research **38**.

Sturm, M., and C. Benson. 2004. Scales of spatial heterogeneity for perennial and seasonal snow layers. Annals of Glaciology **38**:253-260.

Sturm, M., B. Taras, G. E. Liston, C. Derksen, T. Jonas, and J. Lea. 2010. Estimating Snow Water Equivalent Using Snow Depth Data and Climate Classes. Journal of Hydrometeorology **11**:1380-1394.

Teti, P. 2003. Relations between peak snow accumulation and canopy density. Forestry Chronicle **79**:307-312.

The Nature Conservancy, and Environmental Systems Research Institute. 1994. National Vegetation Classification Standard United States Department of Interior United States Geological Survey and National Park Service.

USGS-NPS. 2007. Vegetation mapping program. Sequoia and Kings Canyon National Parks, Three Rivers, California.

Vankat, J. L., and J. Major. 1978. Vegetation Changes in Sequoia National Park, California. Journal of Biogeography **5**:377-402.

Varhola, A., N. C. Coops, Y. Alila, and M. Weiler. 2013. Exploration of remotely-sensed forest structure and ultrasonic range sensor metrics to improve empirical snow models. Hydrological Processes:n/a-n/a.

Varhola, A., N. C. Coops, C. W. Bater, P. Teti, S. Boon, and M. Weiler. 2010. The influence of ground- and lidar-derived forest structure metrics on snow accumulation and ablation in disturbed forests. Canadian Journal of Forest Research-Revue Canadienne De Recherche Forestiere **40**:812-821.

Westerling, A. L., H. G. Hidalgo, D. R. Cayan, and T. W. Swetnam. 2006. Warming and Earlier Spring Increase Western U.S. Forest Wildfire Activity. Science **313**:940-943.

Winkler, R. D., and R. D. Moore. 2006. Variability in snow accumulation patterns within forest stands on the interior plateau of British Columbia, Canada. Hydrological Processes **20**:3683-3695.

Yatheendradas, S., C. D. P. Lidard, V. Koren, B. A. Cosgrove, L. G. G. De Goncalves, M. Smith, J. Geiger, Z. T. Cui, J. Borak, S. V. Kumar, D. L. Toll, G. Riggs, and N. Mizukami. 2012. Distributed assimilation of satellite-based snow extent for improving simulated streamflow in mountainous, dense forests: An example over the DMIP2 western basins. Water Resources Research **48**:18.

Table 1. Sequoia National Park under-canopy basal area by forest type

Forest type	Cover %[a]	Basal area m^2 ha^{-1}	Fractional under-canopy area
Ponderosa pine[b,c]	139[a], 60-80[c]	48, 46	0.48
Jeffery pine[d]	26, 48, 86, 59	31, 38, 42, 62	0.48, 0.79, 1.1, 1.2
White Fir[b]	110[a]	70	0.70
White Fir – sugar pine[c]	60-100[c]	52	0.70
White Fir – Giant Sequoia[b]	115[a]	83	0.82
Giant Sequoia[c]	60-100[c]	101	1.26
Red fir[b]	74	93	1.2, 1.24
Lodgepole pine[b]	55	65	1.17
Western white pine[b]	28	34	1.25
Foxtail Pine[d]	56	32	0.57

[a] Estimated cover % > 100 includes overlapping canopies and is considered 100% canopy cover in basal area calculation

[b] Adapted from (Vankat and Major 1978)

[c] Adapted from Table 1 in (Battles et al. 2013) 60-100% canopy cover was calculated at 80%

[d] Data from (Rundel et al. 1977)

Table 2. Individual canopy variable regression results for precipitation events

Variable	Range	Number of precip. events[a]	Radius or view factor of max R^2	R^2/p
Mean height	0-40 m	17	8 m	0.58/<0.001
Stdev height	0-18 m	17	10 m	0.51/<0.001
CSR	0-13	16	11 m	0.48/<0.001
Frac. cover	0-1	15	8 m	0.45/<0.001
CV height	0-5.6	13	9 m	0.38/<0.001
Max height	0–66 m	11	10 m	0.40/<0.001
Mean SVF	0-100%	12	21°	0.59/<0.001
LAI_{Licor}	1.0-3.2	13	-	0.32/=0.002
LAI_{Hemi}	1.1-3.9	12	-	0.27/=0.01
Gap radius	0-10 m	11	-	0.25/<0.001

[a] number of statistically significant events out of 20 where $p < 0.05$ at radius or view factor with highest R^2

Table 3. Snow density (kg m^{-3}) 1 m from tree trunk

Azimuth	n	Mean[a]	STD[a]	SEM[a]
south	100	399	81	8
north	104	382	69	7
west	107	374	73	7
east	98	366	79	8

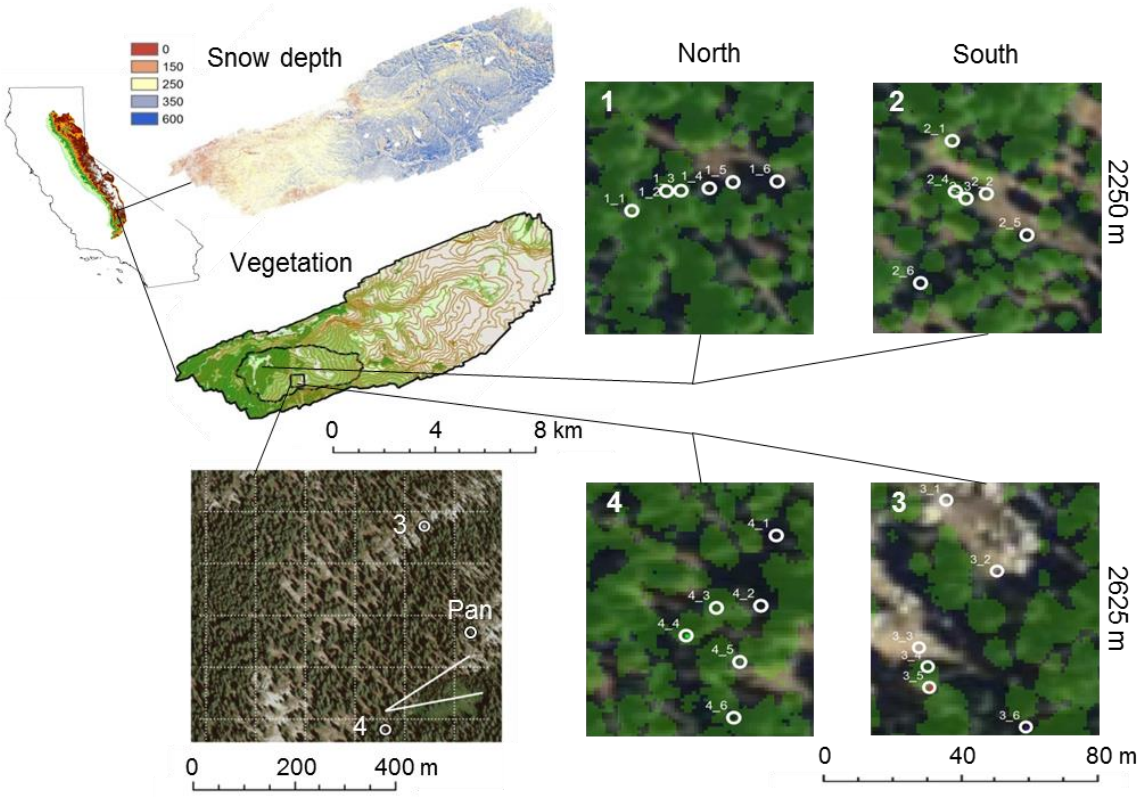

Figure 1. Study area locations. Map in upper left shows Sierra Nevada elevation, with inserts for snow depth and vegetation. On the vegetation insert the darkness of green shading indicating vegetation types, with 50-m elevation contours and locations of Wolverton watershed and Panther study areas also shown. The lower-left digital orthophoto shows locations for upper instrument clusters 3 and 4, Panther met station and snow course transects (lines). The right panels are digital surface models of vegetation height over orthophotos for south-facing (2 and 3) and north-facing (1 and 4) instrument clusters, showing sensor-node locations. The Wolverton met station, approximately 100 m north of site 1, is not shown.

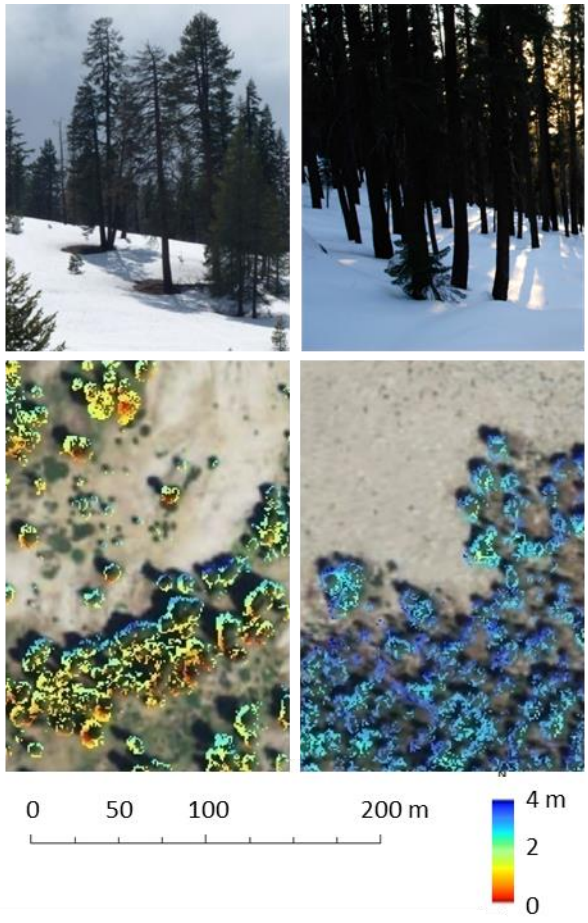

Figure 2. Upper panels: Photographs of typical lower-elevation, south-facing (left) and higher-elevation north-facing (right) forests. Lower panels: Classified LiDAR snow depth under canopy >2 m overlain on orthophotos. Note lack of LiDAR data under densest canopy closest to center of crown for each tree.

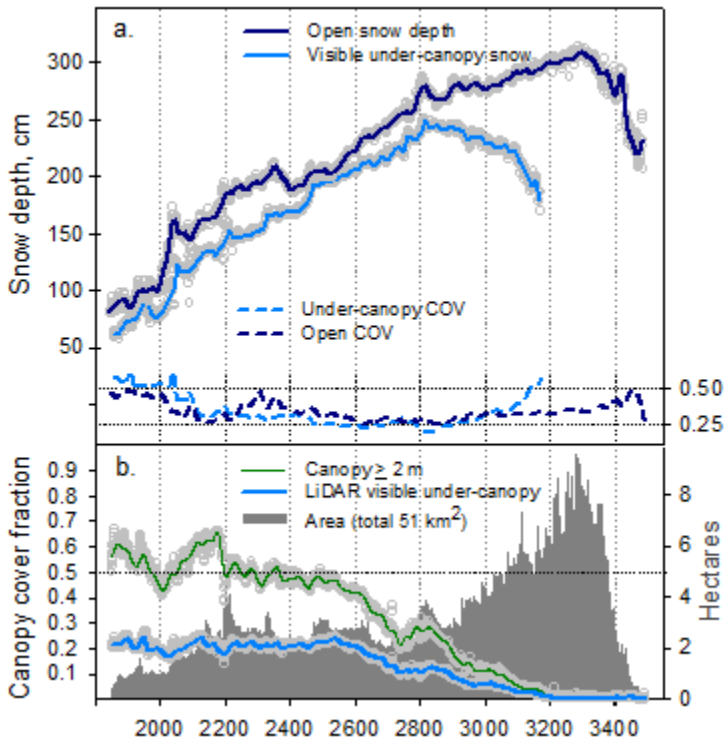

Figure 3. a) LiDAR-derived snow depth by elevation for visible under-canopy and open areas with coefficient of variation. b) Total of area for each 1-m elevation band (dark gray), fraction of area covered by forest canopy over 2 m and fraction of area with under-canopy LiDAR snow-depth retrievals. Colored lines are 16-m running averages and light grey circles are 1-m intervals.

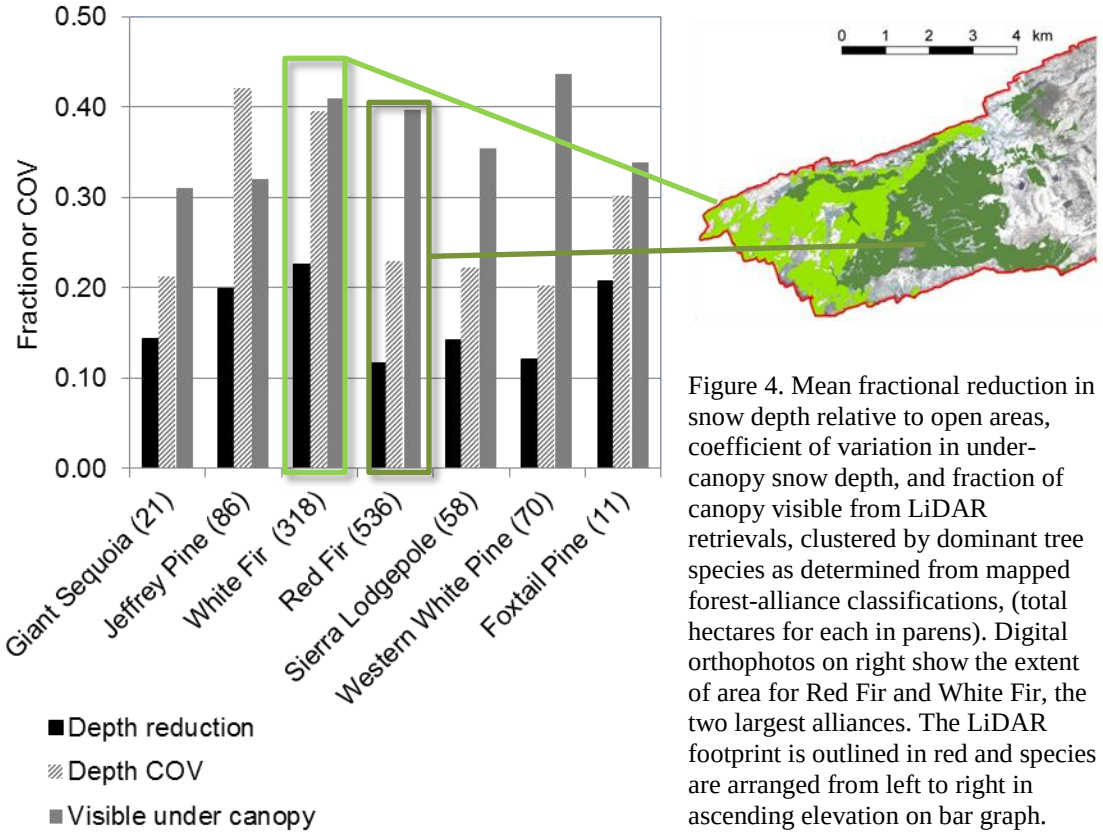

Figure 4. Mean fractional reduction in snow depth relative to open areas, coefficient of variation in under-canopy snow depth, and fraction of canopy visible from LiDAR retrievals, clustered by dominant tree species as determined from mapped forest-alliance classifications, (total hectares for each in parens). Digital orthophotos on right show the extent of area for Red Fir and White Fir, the two largest alliances. The LiDAR footprint is outlined in red and species are arranged from left to right in ascending elevation on bar graph.

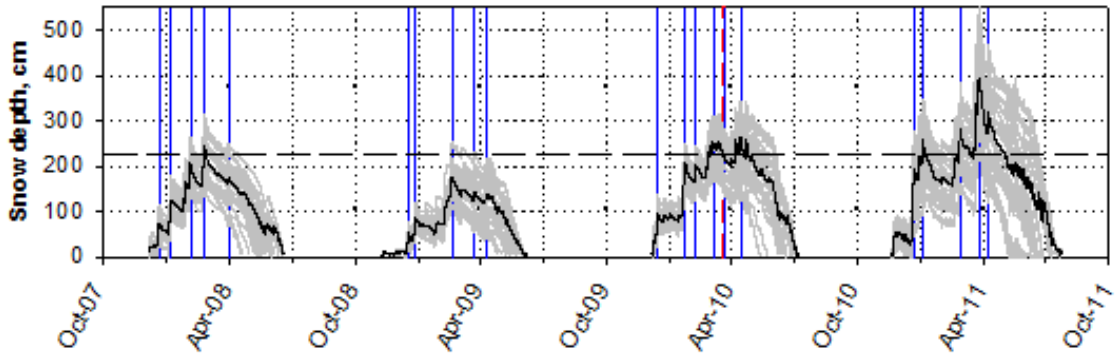

Figure 5. Snow depth for the 26 sensor nodes (gray), with mean depth in black. The vertical blue drop lines mark precipitation events evaluated in this study, dashed red line LiDAR acquisition date and horizontal dashed line 30-year mean snow course depth.

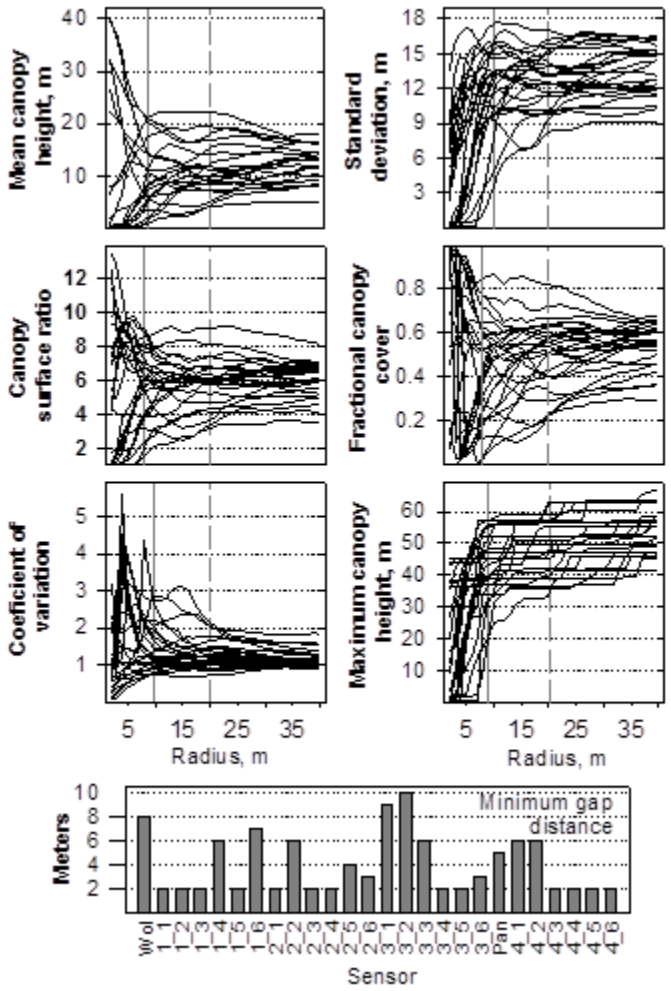

Figure 6. LiDAR-derived canopy metrics from 26 snow-depth sensor nodes. Top panels show mean values at 2 -40 m radii, solid gray lines indicate radii with the highest coefficient of determination with snow accumulation, and dashed line at 20 m is upper range of measurements used for further regression analysis. Lower panel shows distance from node to gap edge (minimum gap radius) at each sensor location.

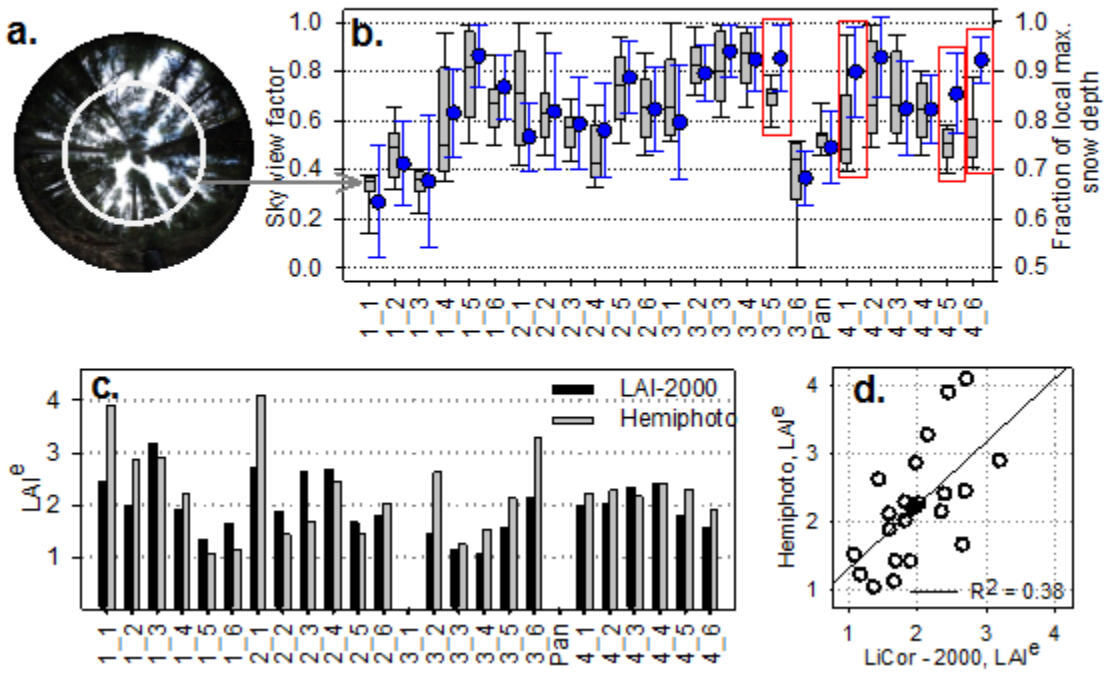

Figure 7. In situ derived canopy metrics for snow depth sensor locations a) hemi-photos represent the range of canopy closure, with open white circle illustrating the 0-40° range shown in each box plot. b) Distribution of integrated SVF for 25 snow-sensors for 0-40° of zenith; note fraction of local maximum snow depth scales to ~1:3 with the exception of 4 outliers in red boxes. c) LAI derived by the two indirect methods at 23 sensor nodes. d) Regression between the two methods of measuring LAI.

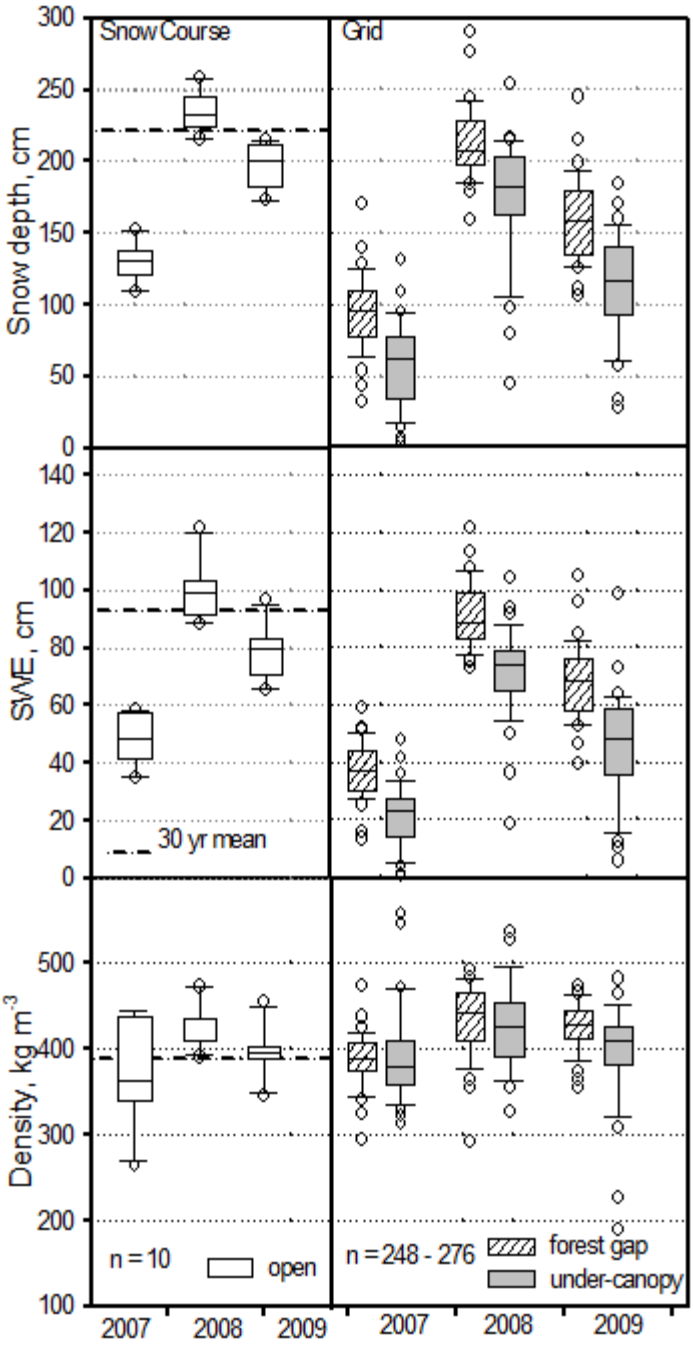

Figure 8. Early April snow depth, SWE and density measurements from Panther Meadow snow course (left) and repeat grid surveys (right); snow course is mostly open and grid samples are under canopy, 1 m from the trunk in each cardinal direction, and in forest gaps, ≥2 m from the canopy edge.

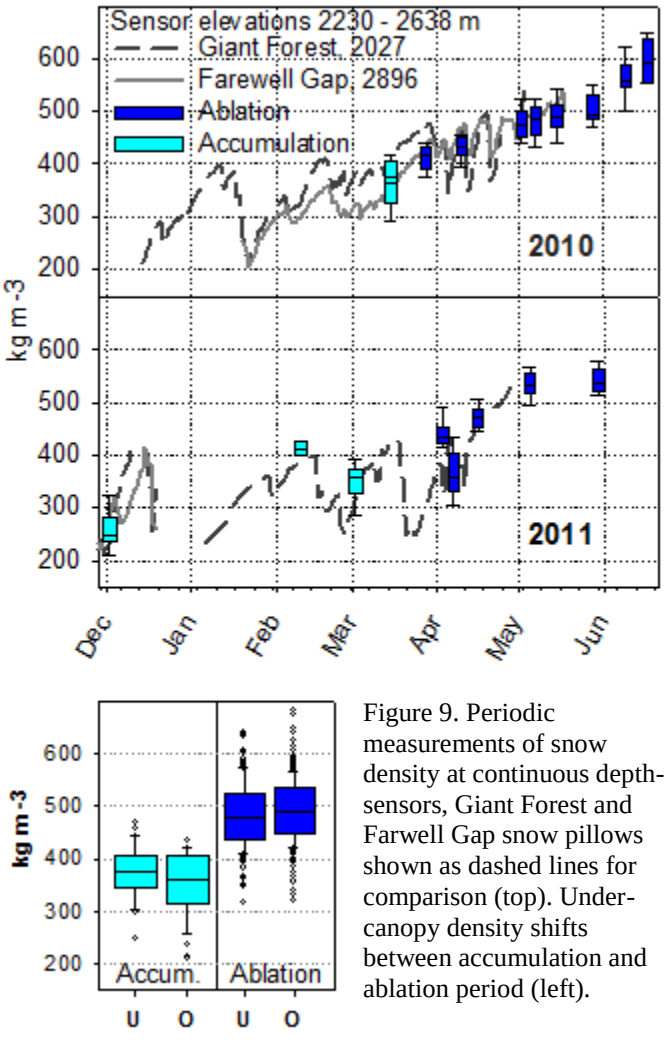

Figure 9. Periodic measurements of snow density at continuous depth-sensors, Giant Forest and Farwell Gap snow pillows shown as dashed lines for comparison (top). Under-canopy density shifts between accumulation and ablation period (left).

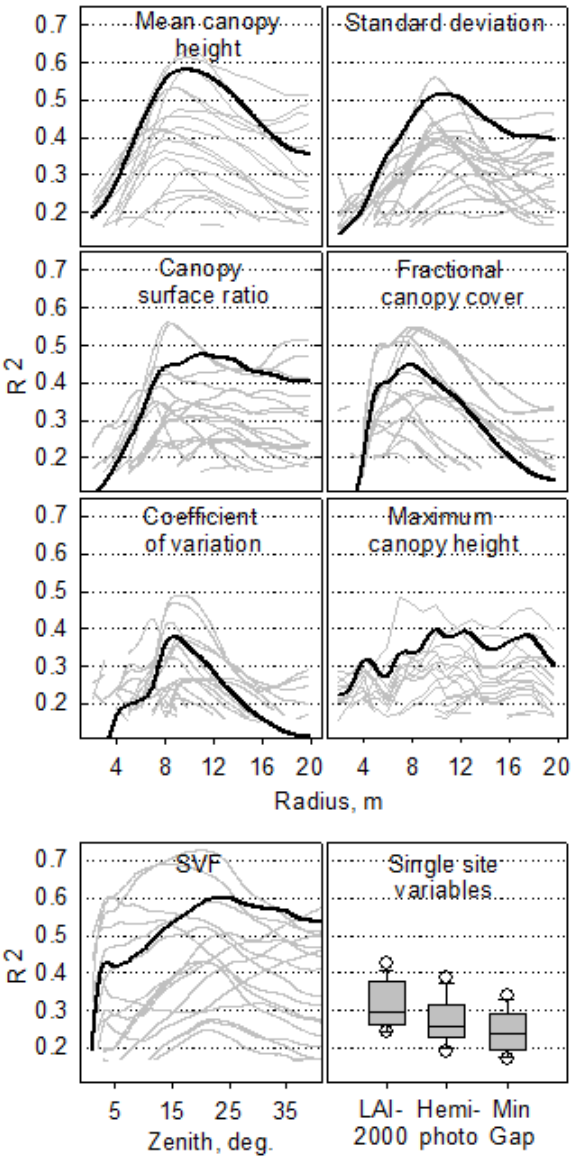

Figure 10. Coefficient of determination for standardized fractional snow accumulation of 20 precipitation events and: six LiDAR canopy parameters over 2 – 20 m radii, grey lines; mean black line (top 6 panels), SVF from 1 to 40º zenith angles (lower left), and single node variables of minimum gap distance, m; LAI^{e} from LAI-2000 and hemiphoto (lower right) all data are $p < 0.05$.

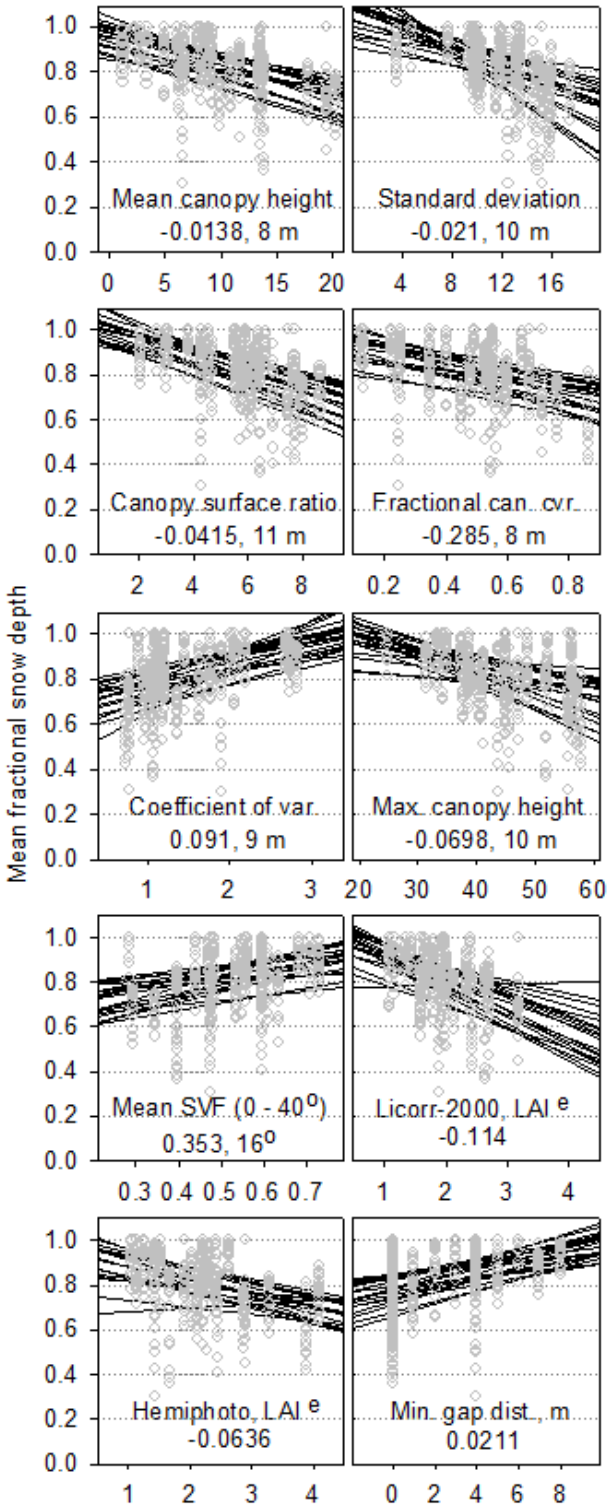

Figure 11. Linear regressions of mean fractional snow depth and: LiDAR canopy variables at 10 m radii, mean SVF and two methods of effective LAI, for 20 precipitation events at 26 sensor locations. Slopes of best-fit radii are listed after variable with highest R^2 area of integration.

CHAPTER 4

CONCLUSIONS

This work was motivated by the need for greater certainty in monitoring and predicting water resource availability from snowmelt in the Mountain West. Due to a climatically uncertain future our current snowmelt water resources monitoring and prediction methods are not adequate to meet the challenge. With the use of emerging technologies, such as airborne LiDAR altimetry and hydrologic observatory sensor networks, new approaches to constraining this uncertainty are now possible. We investigated specific problems of quantifying hydrologic resources for the Mountain West and the southern Sierra Nevada in particular.

1. Elevation and topographic effects on accumulation

We presented research into the distribution of snow over a 1650 m elevation gradient using LiDAR-derived snow-depth altimetry and ground based instrumentation. We found evidence of large-and small-scale trends from orographic processes, mean freezing level, slope, terrain orientation and wind redistribution. Snow-depth increased approximately 15 cm per 100 m elevation from snow line to about 3300 m and, when scaled to the mean regional snow density on the acquisition dates (384 kg m^{-3}), this equaled approximately 6 cm per 100 m elevation SWE. This rate is nearly equal to SWE reconstructions but much higher than the widely used PRISM precipitation data. From 3300 m to our highest measurements at 3494 m, snow-depth decreased approximately 48 cm per 100 m elevation. Both PRISM and SWE reconstructions show reductions at higher elevations as well. Local departures from the trend of linear increase with elevation of +30 to -140 cm were also found in the elevation profile of 1-m elevation bands. The likely causes of these finer-elevation-scale departures are: ablation, terrain orientation, slope and wind redistribution from west to east, reduction in precipitation

from upslope lifting, and or the exhaustion of precipitable water from ascending air masses. These results are presented in chapter 2 and Appendix A and B.

2. Forest canopy effects on accumulation and ablation

Using high-point-density LiDAR-derived snow-depth we measured 31-44% of the under-canopy area, depending on dominant vegetation type. Snow-depth was 40-100 cm (12-24%) lower under-canopy versus in the open, with the highest variability in locations subjected to early season ablation or wind redistribution. The metrics of mean canopy height, canopy-to-ground surface ratio, fractional canopy cover, and canopy-height standard deviation individually explained up to half of the variability (R^2 of 0.45-0.58) and slightly more in combination. The under-canopy differences in snow water equivalent early in the snow season were partially offset by 8-15 kg m^{-3} (2-4%) higher snow density at under-canopy locations. However, under-canopy areas shifted to lower snow densities later during snowmelt, with locations having higher radiative forcing, e.g. south-facing slopes the south azimuth of trees, showing consistently higher snow densities. The combined metrics of cumulative direct-beam solar irradiance and Sky View Factor (SVF), derived from hemispherical photographs, explain most of the SWE ablation-rate variability observed at the plot scale. In the most cloud-free season direct-beam solar irradiance explained 58 % of the variance and in the cloudier snowmelt season SVF explained 87%. These results are presented in chapter 3 and appendices C, D, E and F.

3. Subsurface water partitioning

Diel patterns in soil moisture, measured by collocated snowdepth and soil-moisture sensors, are good indicators of snowmelt timing and duration at the plot scale. When these measurements are distributed over a range of canopy conditions and topography they reveal the variability in melt conditions at broader scales. Measurements made in the top meter of soil showed streamflow response to rainfall and snowmelt above a soil moisture threshold of about 21 cm. After snowmelt soils dried at a fairly uniform rate due to fairly homogeneous soil-texture properties, and the limited

water-holding capacity of the soils in our study areas. However, the timing of melt was offset by up to 4 weeks depending on the location and the timing of the snowmelt. We also found that baseflow and evapotranspiration continued after soil dry down has reached a plateau, suggesting that water continues to be drawn from soil saprolite and saprock at depths greater than our measurements 1 m below the surface. These results are presented in chapter 3 and appendices E and F.

4. Future work

New remote sensing efforts collecting high resolution LiDAR and snow reflectance properties in strategically important watersheds are being conducted in California and Nevada in addition to on-going ground observations and planned modeling efforts (Lin et al. 2011, Buis et al. 2013). Using the findings and methods presented we will address the following objectives.

1.) Prediction of the temporal and spatial variability of snow density using snowpack cold content with radiative forcing as a proxy.

2.) Model development for quantifying under-canopy SWE over a broad range of topography and forest types.

3.) Developing a time series of elevation precipitation gradients and analysis of their response to specific climate circulation patterns and individual events such as atmospheric rivers.

Insights gained from this work may also support research in other fields of earth and ecosystem science. Researchers modeling mountain glacier growth and recession should benefit from the insights of this research into the relationship between snow distribution and geomorphology (Galewsky 2009, Barr and Spagnolo 2013).

Lastly we expect further application of the novel spatial analysis methods we developed, i.e. aspect intensity and canopy surface area, for investigations of ecosystem structure and function. For example, to better understand how the position on the landscape may affect the energy environment of critical zone processes (Chorover et al. 2011).

References

Barr, I. D., and M. Spagnolo. 2013. Palaeoglacial and palaeoclimatic conditions in the NW Pacific, as revealed by a morphometric analysis of cirques upon the Kamchatka Peninsula. Geomorphology **192**:15-29.

Buis, A., S. Cole, and E. Scott. 2013. NASA Opens New Era in Measuring Western U.S. Snowpack. Jet Propulsion Laboratory News.

Chorover, J., P. A. Troch, C. Rasmussen, P. D. Brooks, J. D. Pelletier, D. D. Breshars, T. E. Huxman, S. A. Kurc, K. A. Lohse, J. C. McIntosh, T. Meixner, M. G. Schaap, M. E. Litvak, J. Perdrial, A. Harpold, and M. Durcik. 2011. How Water, Carbon, and Energy Drive Critical Zone Evolution: The Jemez Santa Catalina Critical Zone Observatory. Vadose Zone Journal **10**:884-899.

Galewsky, J. 2009. Rain shadow development during the growth of mountain ranges: An atmospheric dynamics perspective. Journal of Geophysical Research: Earth Surface **114**:F01018.

Lin, H., J. W. Hopmans, and D. d. Richter. 2011. Interdisciplinary Sciences in a Global Network of Critical Zone Observatories. Vadose Zone Journal **10**:781-785.

APPENDIX A

LiDAR-DERIVED SNOWPACK DATASETS FROM MIXED CONIFER FORESTS ACROSS THE WESTERN U.S.

Harpold, A.A., Q. Guo[2], N. Molotch, P. D. Brooks, R. Bales, J.C. Fernandez-Diaz, K.N. Musselman, and T.L. Swetnam, P. Kirchner, M. Meadows, J. Flanagan, R. Lucas

Submitted for review to Water Resources Research, 9/27/2013

1 ***LiDAR-Derived Snowpack Datasets From Mixed Conifer Forests Across the Western U.S.***

2

3 Harpold, A.A.[1], Q. Guo[2], N. Molotch[1,3], P. D. Brooks[4], R. Bales[2], J.C. Fernandez-Diaz[5], K.N.
4 Musselman[6,7], T.L. Swetnam[8], P. Kirchner[2,9], M. Meadows[2], J. Flanagan[2], and R. Lucas[2]

5

6 1. Institute for Arctic and Alpine Research, University of Colorado, Boulder, CO
7 2. Sierra Nevada Research Institute, University of California Merced, CA
8 3. Jet Propulsion Laboratory, Pasadena, CA
9 4. Hydrology and Water Resources, University of Arizona, Tucson, AZ
10 5. National Center for Airborne Laser Mapping, Houston, TX
11 6. Civil and Environmental Engineering, University of California, Los Angeles, CA
12 7. Now at: Centre for Hydrology, University of Saskatchewan, Saskatoon, SK
13 8. School of Natural Resources and the Environment, University of Arizona, Tucson, AZ
14 9. Now at: Joint Institute for Regional Earth System Science and Engineering, University of
15 California, Los Angeles, CA

16

17

18 **Submitted to Water Resources Research**

19 **September 27, 2013**

20 ***LiDAR-Derived Snowpack Datasets From Mixed Conifer Forests Across the Western U.S.***

21 Airborne-based Light Detection and Ranging (LiDAR) offers the potential to measure snow
22 depth and vegetation structure at high spatial resolution over large extents and thereby increase
23 our ability to quantify snow water resources. Here, we present airborne LiDAR data products at
24 four mixed-conifer Critical Zone Observatories (CZO) in the Western U.S.: Jemez River Basin,
25 NM, Boulder Creek Watershed, CO, Kings River Experimental Watershed, CA, and Wolverton
26 Basin, CA. We make publicly available snow depth data products (1-m^2 resolution) derived from
27 LiDAR with an estimated accuracy of <30 cm compared to limited field observations.

28 **1. INTRODUCTION**

29 Seasonal mountain snowpacks are the major source of water for human and natural systems in
30 the semi-arid Western U.S. [*Bales et al., 2006*]. The interactions between vegetation,
31 topography, and climate play a central role in the accumulation, ablation, and partitioning of
32 snowpacks to the atmosphere versus infiltration and runoff. Local canopy structure (i.e. canopy
33 density, canopy height, etc.) at the tree and stand scale strongly controls snowpack accumulation
34 and ablation [*Golding and Swanson, 1986; Molotch et al., 2009, Varhola et al., 2010, Varhola*
35 *and Coops, 2013*]. Airborne-based Light Detection and Ranging (hencefore referred to as
36 LiDAR) datasets are increasingly used to estimate snow depth at high resolution (<1 m^2) at
37 landscape scales (>100 km^2) by differencing 'snow-covered' and 'snow-free' elevation data
38 products [*Hopkinson et al., 2004; Deems et al., 2006; Trujillo et al., 2007; DeBeer and*
39 *Pomeroy, 2010; Grunewald et al., 2013; Varhola and Coops, 2013*]. Widespread application of
40 LiDAR for snowpack monitoring is principally limited by economic constraints, however a lack
41 of standardized protocols for collecting, processing, and reporting LiDAR-derived snow depth
42 products also impedes comparisons across sites and for repeat investigations of a single site
43 [*Hopkinson and Goulden, 2010; Deems et al., 2013*].

44 The goal of this paper is to present high-quality, publicly available LiDAR-derived snow depth
45 data products from four U.S. National Science Foundation's Critical Zone Observatory (CZO)
46 sites across the Western U.S. The CZO sites include forested research catchments where
47 intensive ecological and hydrological measurements are currently being made. The sites
48 represent a gradient of hydroclimate and dominant snow processes.

2. SITE DESCRIPTION

We describe LiDAR data products from four CZO sites in the Western U.S.: Jemez River Basin (JRB), Boulder Creek Watershed (BCW), Kings River Experimental Watershed (KREW), and Wolverton Basin (WLVB). The four LiDAR extents vary in size and land cover (Figure 1), but were generally steep, mixed-conifer forests and alpine areas with seasonal snowpacks. A total of seven catchments were investigated across the four CZO sites; two each in BCW, JRB, KREW, and one from WLVB (Table 1). The BCW site had the largest snow-covered LiDAR extent covering >400 km^2 with forests containing ponderosa pine, subalpine fir, Engelman Spruce, and lodgepole pine to rock and glaciers at elevations >3000 m (Figure 1). The JRB site had a LiDAR extent of 294 km^2, with grasslands at lower elevations, transitioning to mixed conifer forests of Douglas fir, white fir, blue spruce, southwestern white pine, limber pine, and ponderosa pine at higher elevations (Figure 1). The KREW site was 18 km^2 consisting of forests with red fir, white fir, Jeffrey pine, and Lodgepole pine and rocky outcrops at higher elevations (Figure 1). Similar tree species were present in the lower elevation WLVB and KREW sites, but the WLVB snow-covered extent was larger (59 km^2) and extended into alpine areas at higher elevations (Figure 1). Differences in winter climates are typified by the differences in maximum SWE in 2010 and 'winter' (October through April) precipitation (P) and temperature (T) over five years (Table 1). The climate observations suggest wetter (P>80 cm) and warmer (T >4 C) winters at the Sierra Nevada sites (KREW and WLVB) compared to the colder (T <-2 C), drier (P <45 cm) Rocky Mountain sites (BCW and JRB).

3. DATA DESCRIPTION

3.1 LiDAR and Field Data Collection

The objective of the LiDAR flights was to measure near-peak snow accumulation for water balance estimates at each site, however due to logistics all flights occurred after melt had begun (Table 2). Snow-covered flights were made over 1 to 2 consecutive days, with the exception of BCW. The BCW flights were completed over 5/5/2010, 5/9/2010, and 5/20/2010, of which the first and last flights cover the full extent of BCW site. The acquisition procedures resulted in an average of 8 to 11 returns per square meter across the sites (described more in Supplemental

77 Information). The extent of the snow-free LiDAR datasets exceeded snow-covered extent in all
78 cases.

79 Snow depth measurements from ultrasonic snow depth sensors installed perpendicular to the
80 snow surface and configured in open and under canopy positions were used as a verification
81 dataset (see Molotch et al., 2009 for configuration). The average snow depth from 12:00 to
82 13:00 on the day of LiDAR flight was used. Observations from continuous snow depth sensors
83 were within 10 cm of manual measurements at peak snow depth in BCW-Como, but accuracy
84 can vary based on sensor height and snow surface topography. The slope and aspect of the
85 sensor location varied widely across the sites, with flatter sites at BCW-Como, JRB-History, and
86 KREW-P303, and steeper slopes sampled at BCW-Gordon, KREW-P301, and WLVB-
87 Wolverton (Table 2). Negative changes in snow depth (melt, sublimation, and densification)
88 prior to the LiDAR flight was estimated by dividing the snow depth at the time of flight by the
89 peak accumulation depth prior to flight (Table 2). Negative changes in snow depth prior to the
90 flight may be important for future applications (e.g. studies of snow accumulation versus
91 ablation). Negative snow depth changes varied between sites, near 100% at BCW-Gordon,
92 ~30% changes at BCW-Como and KREW-P303, and <20% changes at JRB-History, KREW-
93 P301, and WLVB-Wolverton (Table 2). SWE measurements were made by snow pillows shown
94 in Figure 1.

95 **3.2 LiDAR Data Processing**

96 Development of the point cloud datasets required measurements from the airplane and ground
97 that are detailed in the supplemental information. In addition, each point was classified as ground
98 or non-ground (vegetation, building, etc.) using Terrasolid's TerraScan™(see Supplemental
99 Information). The LAS (version 1.2) tiles for snow-covered and snow-free flights were in UTM
100 NAD1983 projection with NAVD88 geoid and available via OpenTopography
101 (http://www.opentopography.org accessed: 3/22/2013) using the DOI numbers cited below.

102 A simple alternative to the complex LAS point cloud is to collapse the full 3D data into regularly
103 spaced 2.5D grids (x, y, and elevation) that are more easily analyzed. NCALM utilized a Kriging
104 interpolation algorithm available in Golden Software SURFER™ to produce two standard
105 gridded deliverables: a bare-earth digital terrain model (DTM) and a first return (top of canopy)

106 digital surface model (DSM). The DTM and DSM products were delivered in the ESRI grid
107 format [*NCALM, 2010*]. Differencing the snow-free DSM by the DTM produced the canopy
108 height model (CHM) that was used to compare vegetation structure between sites. The snow-
109 depth dataset was the difference between the snow-covered and snow-free DTMs. The result
110 from this differencing procedure was filtered to replace any negative snow depths with zero and
111 remove outliers greater than the largest observed snow depth of 10 m, which is <0.01% of the
112 surface area at all sites. Canopy density and the number of snow surface returns were calculated
113 using FUSION [*McGaughey, 2010*], which were a function of the canopy properties and the
114 LiDAR acquisition capabilities. We also developed a 'mask' layer for locations that did not
115 show a return below a site-specific maximum snow depth that varied from 2 to 5.5 m (see
116 Supplemental Information). Locations in the 'mask' had no direct snow surface elevation
117 information were therefore interpolated from nearby locations (see Supplemental Information).
118 Comparing the mask extent helped us to better evaluate what sites had forest canopy of
119 interfering with LiDAR-derived snow depth accuracy.

120 **3.3 Catchment-Scale Snow and Vegetation Datasets**

121 The seven research catchments were between 1.0 and 5.4 km^2 and were more comparable in
122 terms of elevation and slope than the larger CZO sites (Figure 1 and Table 1). Tree ages and
123 species varied between catchments, but forest cover (area occupied by vegetation >2 m) ranged
124 from 44% to 69% (Table 1). Both forest cover and forest canopy density (fraction of returns >2
125 m) were greatest at KREW-P301 and KREW-P303 (>60% cover and >75% forest density) while
126 the forest canopy was tallest (>17 m) at WLVB-Wolverton. The forest cover was 47% to 53%
127 and forest density was 55% in BCW catchments (Table 1). The JRB catchments were similar,
128 with 44% to 50% forest cover and 66% forest density (Table 1). Average forest height was much
129 shorter in BCW catchments (<6 m) versus the KREW and WLVB catchments (>14 m). It should
130 be noted that canopy height is not equivalent to tree height and is dependent on the surrounding
131 forest cover and canopy density. The percentage of 'masked' area (e.g. no LiDAR returns
132 reached the snow surface) varied considerably across the catchments. Not surprisingly the
133 largest 'mask' areas (>19%) were in the KREW catchments where forest cover and canopy
134 density were greatest; conversely, the smallest mask area (5%) was in BCW-Gordon where
135 forest height and canopy density was lowest (Table 1 and 2).

136 The differences in snow depth between catchments generally reflected differences in amounts
137 and timing of water and energy inputs prior to the 'snow on' flight (Figure 2 and Table 2). For
138 example, KREW and WLVB catchments had roughly double the maximum SWE (>60 cm) of
139 the BCW and JRB catchments (32.5 and 30.4 cm, respectively). Similarly, mean snow depth
140 was greater at KREW and WLVB catchments with snow depth exceeding 97 cm versus average
141 snow depths at the BCW-Como and JRB-History of 59 and 63 cm, respectively. Spatial
142 variability in snow depth was greatest at BCW catchments (coefficient of variation (CV) of 0.69
143 to 1.14), smaller at KREW and JRB (CV of 0.36 to 0.44), and smallest at WLVB (CV of 0.23)
144 (Table 2). In addition, sites with greater negative changes in snow depth prior to the snow-
145 covered flight had shallower snow depths that were more variable. Pre-flight negative changes
146 in snow depth of >32% at BCW catchments corresponded to the shallowest mean snow depths
147 (<97 cm) and greatest variability (CV>0.69). Greater negative changes in snow depth in KREW-
148 P303 versus KREW-P301 (32% and 11%, respectively) corresponded to smaller mean snow
149 depths (97 and 124 cm, respectively) (Table 2).

150 **3.4 Verification of LiDAR-Derived Snow Depth**

151 The errors in the LiDAR-derived snow depth data products, as compared to limited ground-based
152 measurements (Table 2), were similar to those found in other studies [*Hopkinson et al., 2004;*
153 *Geist and Stotter, 2008; Moreno-Banos et al., 2009; Hopkinson et al., 2010; Joerg et al., 2012*].
154 The Root Mean Square Error (RMSE) of the LiDAR-derived snow depths was 23 cm and the r^2
155 was 0.97 ($p<0.0001$) compared to all 60 snow depth sensors (Figure 3). The RMSE varied from
156 7 to 31 cm among the catchments, which had between 5 and 16 snow sensors each (Table 2 and
157 Figure 3). The RMSE was 31 cm at KREW-P303 and only 18 cm at the adjacent, and
158 topographically similar, KREW-P301 catchment (Table 2). Vertical errors below 30 cm were
159 consistent with previous verification efforts in treeless, alpine areas [*Geist and Stotter, 2008;*
160 *Moreno-Banos et al., 2009; DeBeer and Pomeroy, 2010; Joerg et al., 2012*], but similar
161 verification across forested areas are currently lacking [*Hopkinson et al., 2004; Hopkinson et al.,*
162 *2010]*.

163 LiDAR-derived snow depths and RMSE values were larger under-canopy versus open positions
164 (defined as above and below 50% canopy density in the 1-m^2 surrounding the sensor) at all

165 catchments except BCW-Como. For example, in WLVB-Wolverton, RMSE was 26 cm for
166 under-canopy snow depth and 21 cm in open positions, despite similar mean snow depths (267
167 and 260 cm, respectively). Open-canopy snow depths were >20 cm deeper than under-canopy
168 depths on average in KREW-P301 and <20 cm shallower in KREW-P303; however BCW-
169 Como, BCW-Gordon, JRB-History, and WLVB-Wolverton had average open and under-canopy
170 depths within 20 cm of each other (Table 2 and Figure 3).

171 **4. SUMMARY AND CONCLUSIONS**

172 The LiDAR-derived snow depth and vegetation data products presented at four Western U.S.
173 CZO sites were made publicly available
174 (ftp://snowserver.colorado.edu/pub/WesternCZO_LiDAR_data). We showed that the LiDAR-
175 derived snow depths vary considerably among sites as function of climate, snow ablation prior to
176 the flight, and forest canopy structure. This represents one of the most comprehensive
177 verification efforts of LiDAR-derived snow products in forested areas, but lacks verification
178 measurements across the full snow-covered LiDAR extent. The RMSE was 23 cm compared to
179 all 60 snow depth sensors. The greater errors found in under-canopy positions could be due to
180 less LiDAR returns reaching the snow surface, which would have implications for deriving
181 spatially continuous snow depth estimates. For example, the KREW-P303 catchment had the
182 largest under-canopy RMSE values of 33 cm and the largest unsampled area due to the absence
183 of LiDAR returns of 23%. Hence, basin-wide assessments of total snowpack water storage using
184 LiDAR data will have greater uncertainty in KREW-P303. Improved accuracy may be possible
185 using interpolation schemes with *a priori* information on open versus under-canopy snow
186 processes (e.g. Molotch et al., 2009). LiDAR-derived accuracies of 20 to 30 cm can be sufficient
187 for research and practical applications, but our results imply greater caution in areas of shallow
188 snowpacks and/or very dense forest canopy. Waveform LiDAR offers a potential alternative that
189 better penetrates dense forest canopy than discrete LiDAR.

190 The economic and processing limitations of LiDAR data are decreasing rapidly [*Stennett, 2004*]
191 making publicly available LiDAR-derived snow depth and vegetation structure more attractive
192 for managing and researching snow water resources. For example, LiDAR-derived snow depths
193 collected prior to significant ablation can be combined with snow density measurements to

194 estimate SWE for streamflow prediction [*Hopkinson et al., 2012*] and verify distributed snow
195 cover models [*DeBeer and Pomeroy, 2010*]. Snow depth data products have also being used to
196 assess changes in snowpack variability following forest disturbance [*Coops et al., 2009; Harpold*
197 *et al., 2013*]. Better linkages between ground-based observations and LiDAR measurements
198 would help verify LiDAR-derived data products and advance predictions of landscape-scale
199 water and energy fluxes.

200 **Acknowledgements**

201 This research was supported by the National Science Foundation to QG for the collection of the
202 LiDAR data (EAR 0922307), to other co-authors in support of CZO sites (EAR 724960, 725097,
203 724958), and EAR 1141764 and USDA grant 2012-67003-19802. The first author was
204 supported by an NSF EAR Postdoctoral Fellowship (EAR 1144894).

205 **References**

206 Bales R., N.P. Molotch, T.H. Painter, M.D. Dettinger, R. Rice, and J. Dozier (2006) Mountain
207 hydrology of the western United States. Water Resources Research. 42:W08432.
208 DOI:10.1029/2005WR004387

209 Coops, N.C., A. Varhola, C. W Bater, P. Teti, S. Boon, N. Goodwin, M. Weiler (2009)
210 Assessing differences in tree and stand structure following beetle infestation using LiDAR
211 data. Canadian Journal of Remote Sensing. 35:497-508, 10.5589/m10-005.

212 Deems, J. S., S.R. Fassnacht, and K.J. Elder. (2006). Fractal distribution of snow depth from
213 LiDAR data. *Journal of Hydrometeorology*. *7*(2): 285-297.

214 Deems, J.S., T.H. Painter, and D.C. Finnegan (2013) Lidar measurement of snow depth: a
215 review. Journal of Glaciology. 59(215): 467-479. DOI:10.3189/2013JoG12J154

216 DeBeer, C. M. and J. W. Pomeroy (2010) Simulation of the snowmelt runoff contributing area in
217 a small alpine basin. Hydrol. Earth Syst. Sci. Discuss. 7. 971–1003.

218 Geist, T. and J. Stotter. (2008) Documentation of glacier surface elevation change with multi-
219 temporal airborne laser scanner data – case study: Hintereisferner and Kesselwandferner,
220 Tyrol, Austria. Z. Gletscherk. Glazialgeol. 41: 77–106.

221 Golding, D.L. and R.H. Swanson (1986) Snow distribution patterns in clearings and adjacent

forest. Water Resources Research. 22(13): 1931-1940.

Grünewald, T., J. Stötter, J.W. Pomeroy, R. Dadic, I. Moreno Baños, I., J. Marturià, and M. Lehning, (2013). Statistical modelling of the snow depth distribution in open alpine terrain. *Hydrology and Earth System Sciences*. *17*(8): 3005-3021. doi:10.5194/hess-17-3005-2013.

Harpold, A.A., J. Biederman, K. Condon, M. Merino, Y. Korganokar, T. Nan, L.L. Sloat, M. Ross, and P.D. Brooks (2013) Changes in winter season snowpack accumulation and ablation following the Las Conchas Forest Fire. Ecohydrology. DOI:10.1002/eco.1363.

Hopkinson, C., M. Sitar, L. Chasmer, and P. Treitz (2004) Mapping snowpack depth beneath forest canopies using airborne LiDAR. Photogrammetric Engineering & Remote Sensing. 70(3): 323–330.

Hopkinson, C., J. Pomeroy, C. DeBeer, C. Ellis, and A. Anderson. (2010) Relationships between snowpack depth and primary LiDAR point cloud derivatives in a mountainous environment. Remote Sensing and Hydrology. Jackson Hole, Wyoming. IAHS Publ. 352.

Hopkinson, C. and T. Goulden (2010) The forward propagation of integrated system component errors within airborne LiDAR Data. Photogrammetric engineering and remote sensing. 76(5): 589-601.

Hopkinson, C., T. Collins, A. Anderson, J. Pomeroy, I. Spooner (2012) Spatial Snow Depth Assessment Using LiDAR Transect Samples and Public GIS Data Layers in the Elbow River Watershed, Alberta. Canadian Water Resources Journal. 37: 69-87. 10.4296/cwrj3702893

Joerg, P.C., F. Morsdorf, M. Zemp (2012) Uncertainty assessment of multi-temporal airborne laser scanning data: A case study on an Alpine glacier. Remote Sensing of Environment. 127:118-129,.10.1016/j.rse.2012.08.012

McGaughey, R. (2010) FUSION / LDV: Software for LiDAR Data Analysis and Visualization. USDA Forest Service, Pacific Northwest Research Station.

Molotch, N. P., P.D. Brooks, S.P. Burns, M. Litvak, R.K. Monson, J.R. McConnell, and K. Musselman (2009) Ecohydrological controls on snowmelt partitioning in mixed-conifer sub-alpine forests. Ecohydrology. 2: 129–142. DOI: 10.1002/eco.48

250 Moreno-Banos, I., A. Ruiz Garcia, I. Marturia, J. Alavedra, I. Oller, P. Figueras, J. Pina Iglesias,
251 C. Garcia Selles, I. Martinez, P. Figueras, and J. Talaya Lopez (2009) Snowpack depth
252 modelling and water availability from LIDAR measurements in eastern Pyrenees.
253 Proceedings of the International Snow Science Work- shop ISSW Europe. Davos,
254 Switzerland. 202–206, 2009.

255 NCALM. (2010) National Center for Airborne Laser Mapping. CZO Project Mapping Reports.
256 Accessed 2/15/2013: BCW: http://opentopo.sdsc.edu/metadata/BcCZO_project_reports.pdf
257 JRB: http://opentopo.sdsc.edu/metadata/2010_NCALM_CZO_Project_Report_Jemez.pdf
258 KREW and WLVB: https://eng.ucmerced.edu/snsjho/files/MHWG/LiDAR/flight_set_1

259 OpenTopography. The .las files are accessible via DOI numbers at www.opentopography.org.
260 Accessed 2/15/2013. BCW (snow-free): 10.5069/G93R0QR0, JRB (snow-free):
261 10.5069/G9RB72JV, JRB (snow-covered): 10.5069/G9W37T86, KREW and WOLV
262 (snow-free): 10.5069/G9BP00QB, KREW and WOLV (snow-covered):
263 10.5069/G9BP00QB.

264 Stennett, T. A. (2004) Lidar: Strap in tight, and prepare to go vertical. Photogrammetric
265 Engineering and Remote Sensing. 70(5): 545-548.

266 Trujillo, E., J. A. Ramirez, and K. J. Elder (2007) Topographic, meteorologic, and canopy
267 controls on the scaling characteristics of the spatial distribution of snow depth fields. Water
268 Resources Res. 43. W07409. DOI:10.1029/2006WR005317.

269 Varhola A., N.C. Coops, C.W. Bater, P. Teti, S., M. Weiler (2010) The influence of ground- and
270 lidar-derived forest structure metrics on snow accumulation and ablation in disturbed
271 forests. Canadian Journal of Forest Research. 2010. 40: 812-821. 10.1139/X10-008.

272 Varhola, A., and N.C.Coops (2013) Estimation of watershed-level distributed forest structure
273 metrics relevant to hydrologic modeling using LiDAR and Landsat. *Journal of Hydrology*.
274 487: 70-DOI: 10.1016/j.jhydrol.2013.02.032

275

276

277 Table 1. Properties of the snow-covered area for the four CZO sites: Jemez River Basin (JRB),
278 Boulder Creek Watershed (BCW), Kings River Experimental Watershed (KREW), and
279 Wolverton (WLVB) and their corresponding research catchments. Average Winter T and P refer
280 to the period of October 1st to May 1st for water years 2006 to 2010.

Site	BCW, CO		JRB, NM		KREW, CA		WLVB, CA
Snow-covered area (km^2)	261[1], 280[2]		294		18		59
Forest covered (%)	35.0		47.8		57.1		25.0
Forest height (m)	7		11		14		15
Average Winter P (cm)	45.2[a], 27.5[b]		37.1[c]		126.8[e]		84.0[f]
Average Winter T (cm)	-2.7[a]		-2.2[c]		4.2[e]		4.8[f]
Snow-free flight date	8/21-8/26/2010		6/29-7/8/2010		8/5-8/15/2010		8/5-8/15/2010
Snow-covered flight date	5/5[1], 5/20/2010[2]		4/1/2010		3/20/2010		3/21-3/22/2010
2010 max SWE (cm)	32.5[a]		30.4[d]		86.4[e]		59.4[f], 121.8[g]
Catchment	**Como[1]**	**Gordon[2]**	**History**	**Jaramillo**	**P301**	**P304**	**Wolverton**
Area (km^2)	2.42	2.62	2.42	3.05	0.99	1.32	5.40
Elevation (m)	3221	2617	2947	2925	1974	1898	2525
Slope (deg)	12.8	15.4	7.6	8.4	13.8	15.2	21.1
Aspect (deg CW from N)	152	153	125	202	196	230	214
Forest covered (%)	46.9	52.7	49.5	43.7	69.3	60.2	53.1
Forest height (m)	6.4	3.5	10.4	8.9	16.0	14.5	17.1
Forest density (%)	55	54	66	66	75	75	71

[1] refers to 5/5/2010 in Gordon Gulch and [2] to 5/20/2010 in Como Date, and amount of maximum SWE were estimated at a nearby snow pillow at each site (Figure 1): [a] refers to the Niwot SNOTEL, [b] to Sugarloaf NADP site, [c] to VCNP Redondo station, [d] to COSMOS station, [e] to Upper Providence station, and [f] and [g] to the Giant Forest and Farewell Gap CDEC stations

281

Table 2. Properties of the snow-covered flight, measured snowpack properties, and LiDAR-derived snow depths at seven research catchments. Where numbers following the ± symbol refer to standard deviation. The notation # under-canopy (# open) refers to the number of snow sensors, with the number at open positions in parentheses. Under-canopy and open position snow depth refers to snow sensor measurements. RMSE is derived from LiDAR-derived and snow depth sensors. Under -canopy locations had canopy density >50%.

Site	BCW, CO		JRB, NM		KREW, CA		WLVB, CA
Catchment	Como[1]	Gordon[2]	History	Jaramillo	P301	P303	Wolverton
Snow depth (cm)	59 ± 41	7 ± 8	63 ± 26	84 ± 30	124 ± 52	97 ± 43	222 ± 50
Mask area (% of total area)	12.2	5.0	8.4	9.7	19.5	22.8	13.1
# under-canopy (# open)	9(7)	2(3)	7(2)	N/A	6(7)	4(1)	4(8)
Ablation before flight (%)	32 ± 5	96 ± 3	13 ± 15	N/A	11 ± 6	32 ± 19	17 ± 4
Slope of sensors (deg)	1 – 11	16 – 27	0 – 7	N/A	3 – 22	3 – 9	5 – 26
Canopy density at sensors	36	38	21	N/A	48	20	34
Overall RMSE (cm)	27	7	22	N/A	18	31	23
Under-canopy depth (cm)	70 ± 16	0	91 ± 2	N/A	141 ± 63	183	267 ± 82
Under-canopy RMSE (cm)	25	6	24	N/A	18	33	26
Open-canopy depth (cm)	84 ± 15	0	81 ± 21	N/A	197 ± 13	122 ± 63	260 ± 10
Open-canopy RMSE (cm)	29	6	21	N/A	18	31	21

[1] refers to 5/5/2010 in Gordon Gulch and [2] to 5/20/2010 in Como.

311
312
313

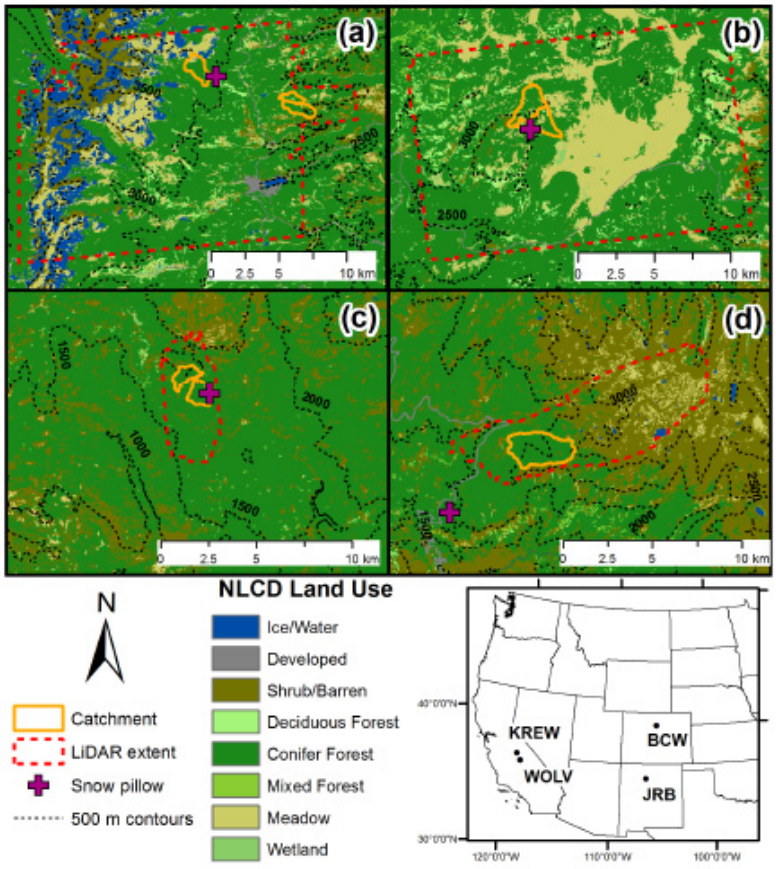

314

315 **Figure 1.** Overview of the snow-covered LiDAR extents for the four study sites showing the
316 research catchments: Boulder Creek Watershed (a), Jemez River Basin (b), Kings River
317 Experimental Watershed (c), and Wolverton Basin (d). The 2001 National Land Cover Database
318 (NLCD) land use classifications are shown. The snow pillows used in Table 1 are also shown.

319

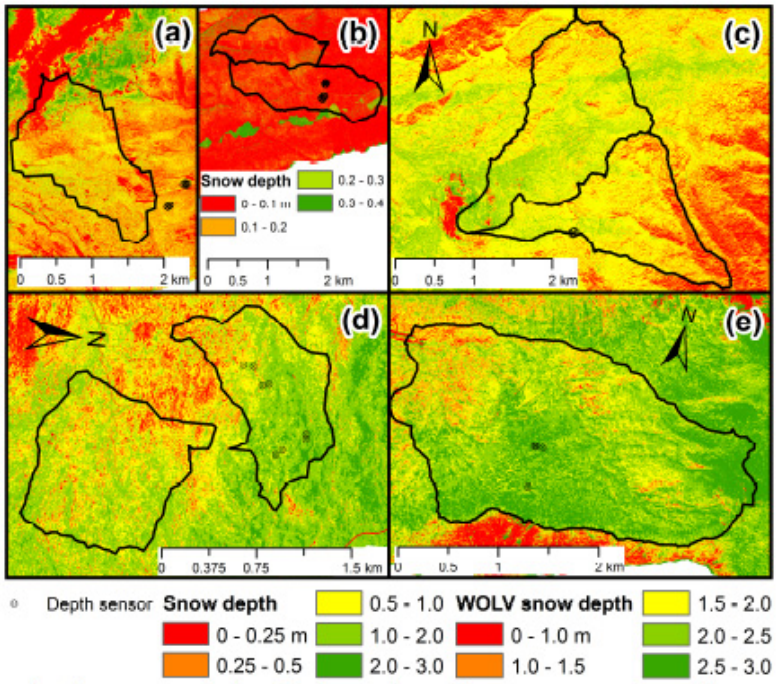

Figure 2. Snow depth at 1-m resolution for the study catchments: BCW-Como (a), BCW-Gordon (b), JRB-Jaramillo and JRB-History (c), KREW-P301 and KREW-P303 (d), and WLVB-Wolverton (e). The locations of the continuous snow depth sensors are also shown. Note the figures have been rotated for ease of display.

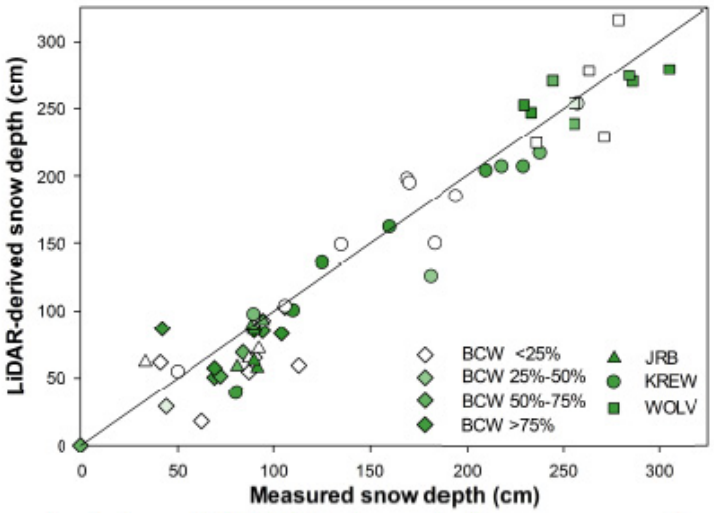

Figure 3. Comparison between LiDAR-derived snow depths versus measured snow depths at the four study sites (represented by different symbols). The color of the symbols refers to the canopy density above the measurement locations. All 60 sensors had a RMSE of 23 cm and r^2 of 0.97 ($p<0.00001$).

APPENDIX B

WOLVERTON BASIN METEOROLOGIC DATA

Meteorologic data collected with the Wolverton Basin Critical Zone Observatory. Metadata, raw data and higher level data can be found at: https://eng.ucmerced.edu/snsjho/files/MHWG/Field/SEKI/Wolverton or by contacting the author. All other meteorologic data sources are cited in main body of text or acknowledgements.

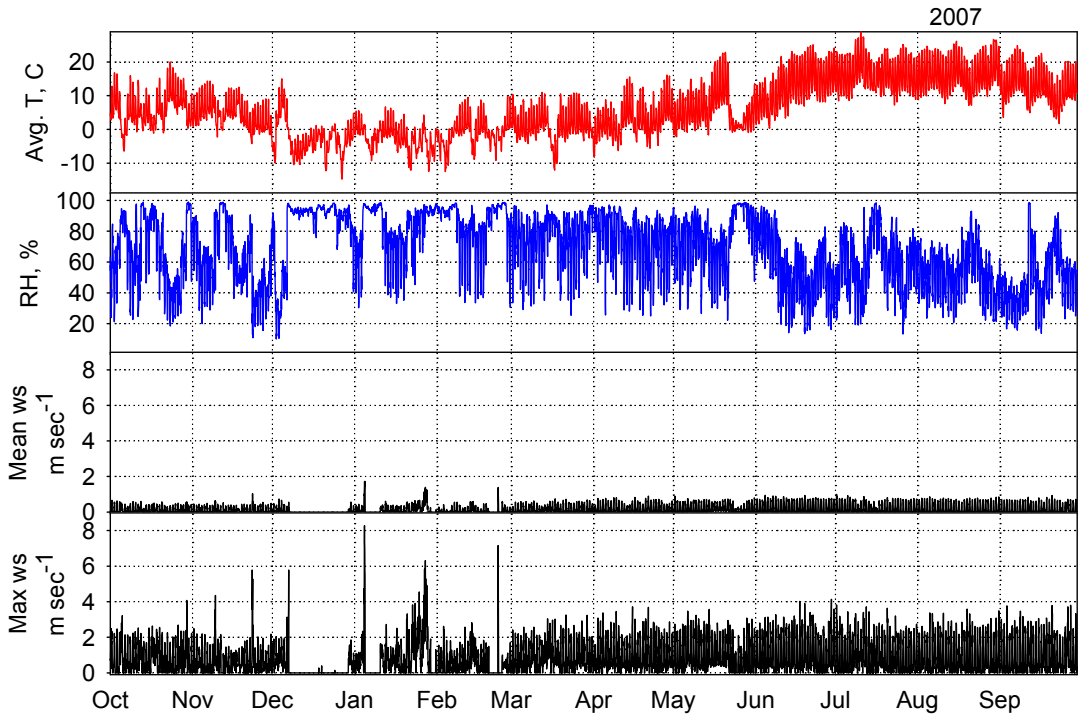

Figure B1: 2007 hourly averages of: mean air temperature, relative humidity, mean wind speed, and maximum wind speed from the Wolverton meteorologic station.

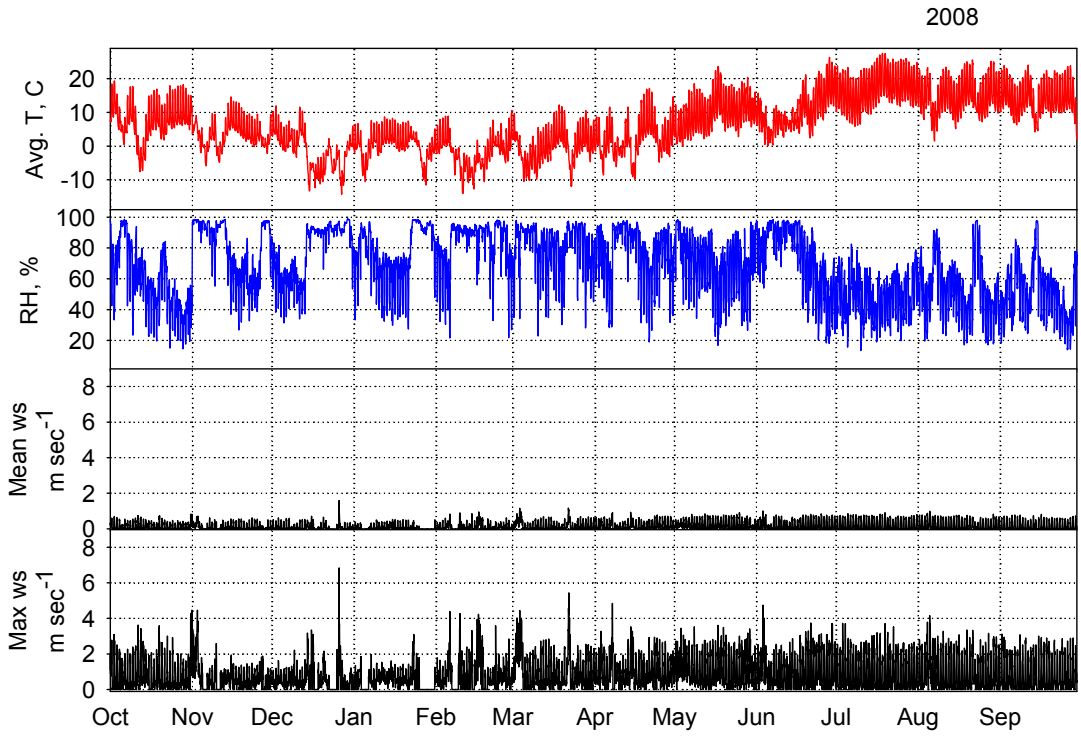

Figure B2. 2008 hourly averages of: mean air temperature, relative humidity, mean wind speed, and maximum wind speed from the Wolverton meteorologic station.

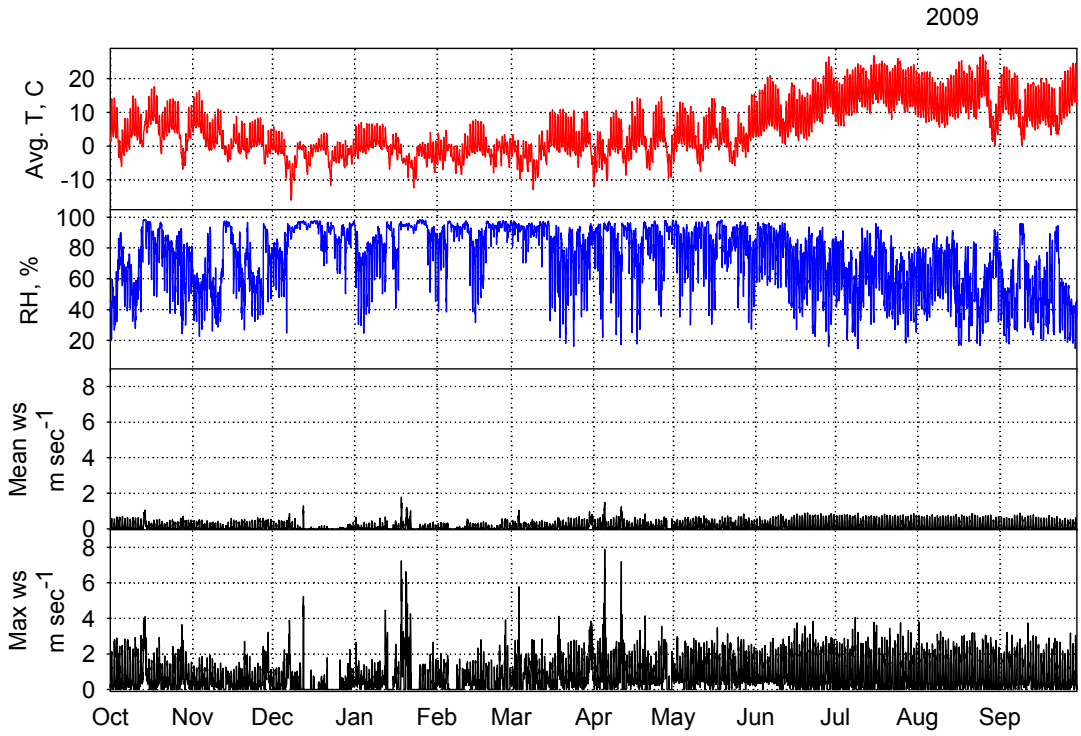

Figure B3. 2009 hourly averages of: mean air temperature, relative humidity, mean wind speed, and maximum wind speed from the Wolverton meteorologic station.

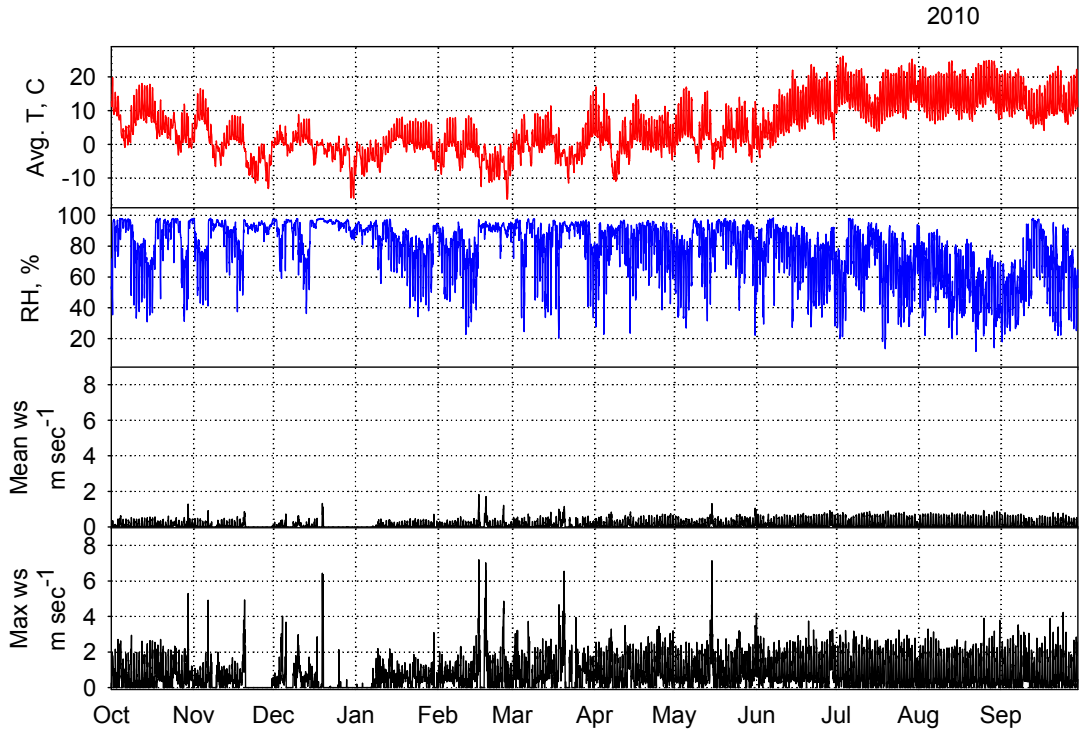

Figure B4: 2010 hourly averages of: mean air temperature, relative humidity, mean wind speed, and maximum wind speed from the Wolverton meteorologic station.

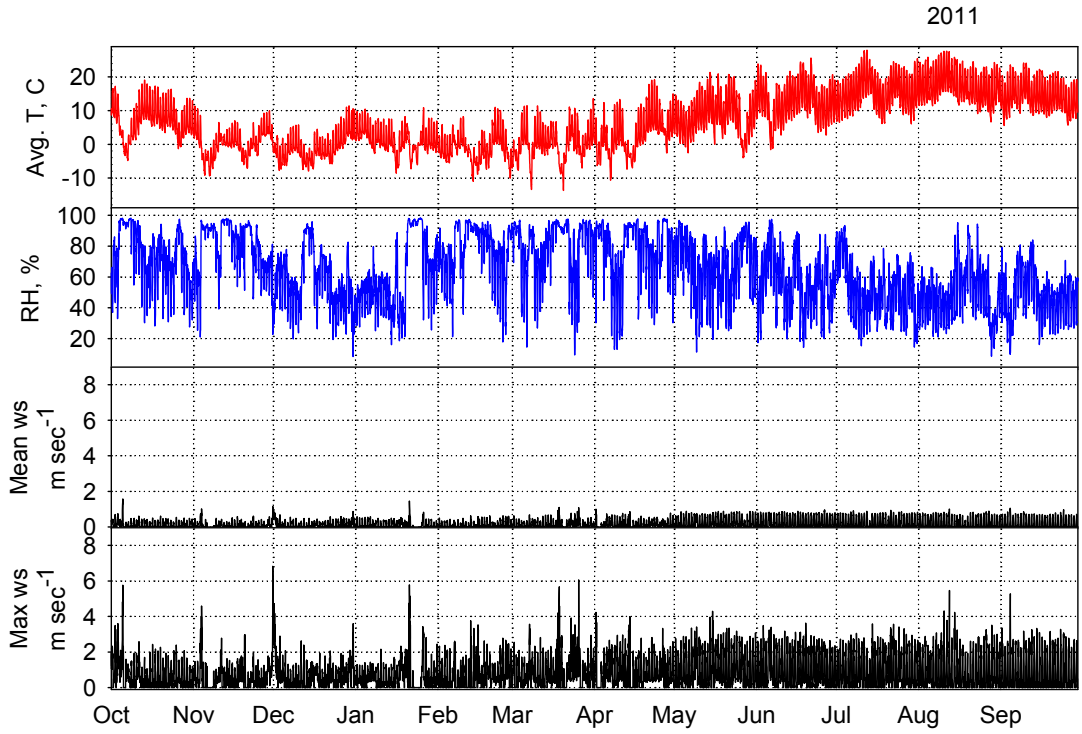

Figure B5. 2011 hourly averages of: mean air temperature, relative humidity, mean wind speed, and maximum wind speed from the Wolverton meteorologic station.

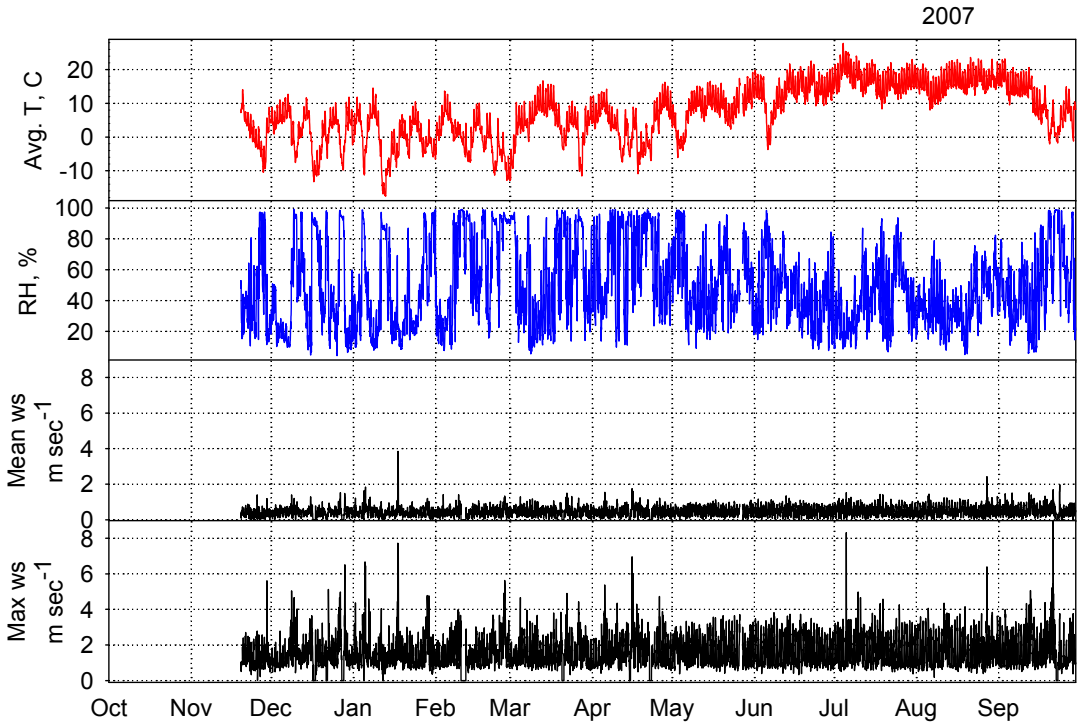

Figure B6. 2007 hourly averages of: mean air temperature, relative humidity, mean wind speed, and maximum wind speed from the Panther Meadow meteorologic station.

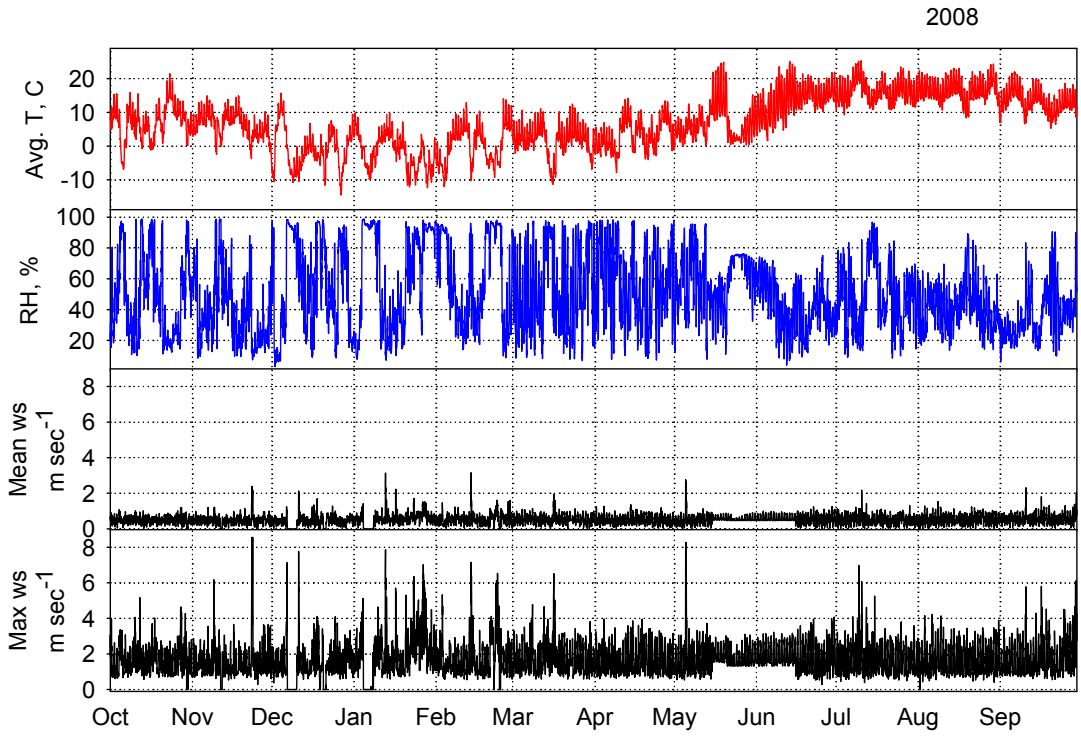

Figure B7. 2008 hourly averages of: mean air temperature, relative humidity, mean wind speed, and maximum wind speed from the Panther Meadow meteorologic station.

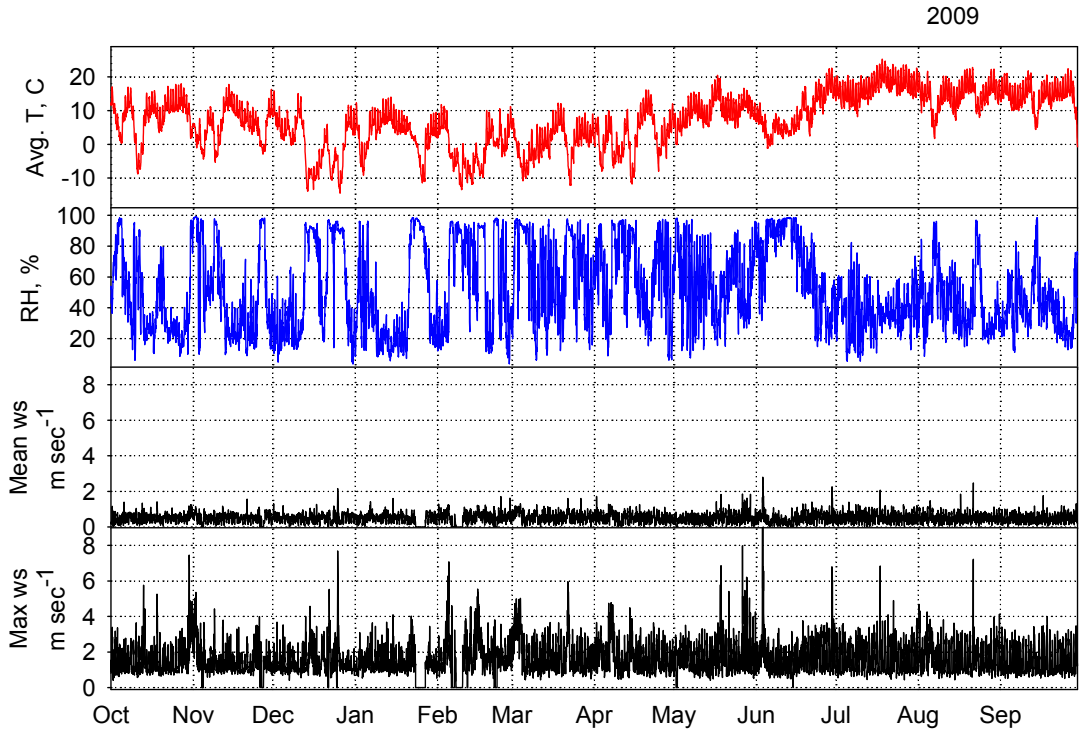

Figure B8. 2009 hourly averages of: mean air temperature, relative humidity, mean wind speed, and maximum wind speed from the Panther Meadow meteorologic station.

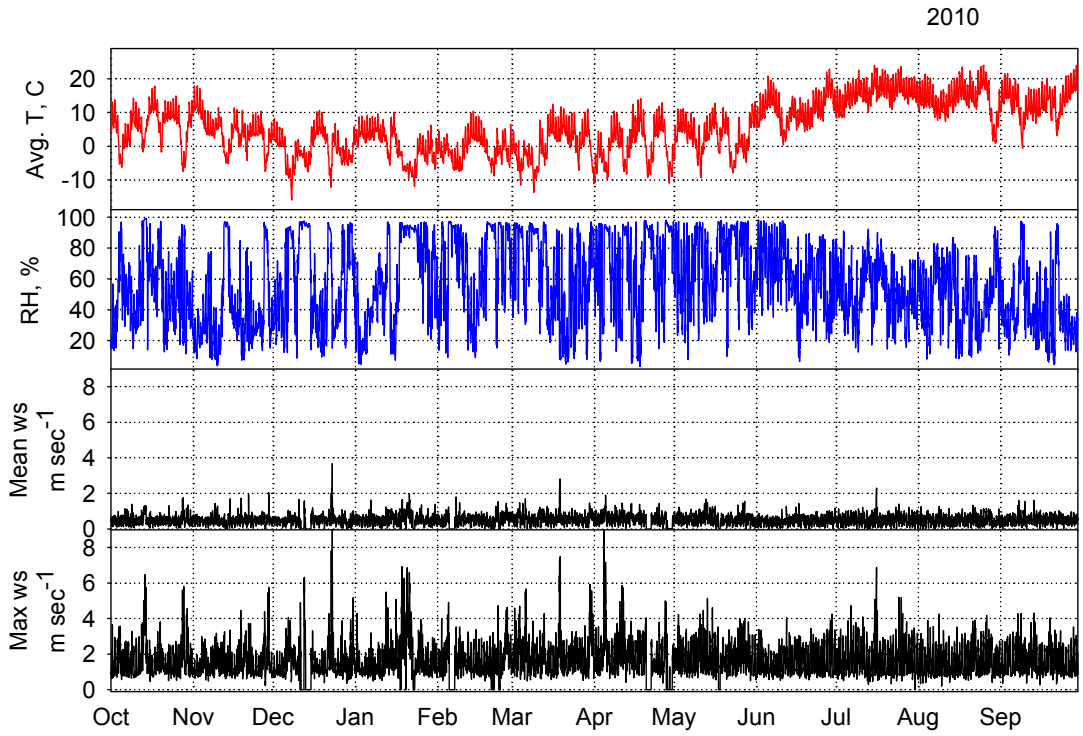

Figure B9. 2010 hourly averages of: mean air temperature, relative humidity, mean wind speed, and maximum wind speed from the Panther Meadow meteorologic station.

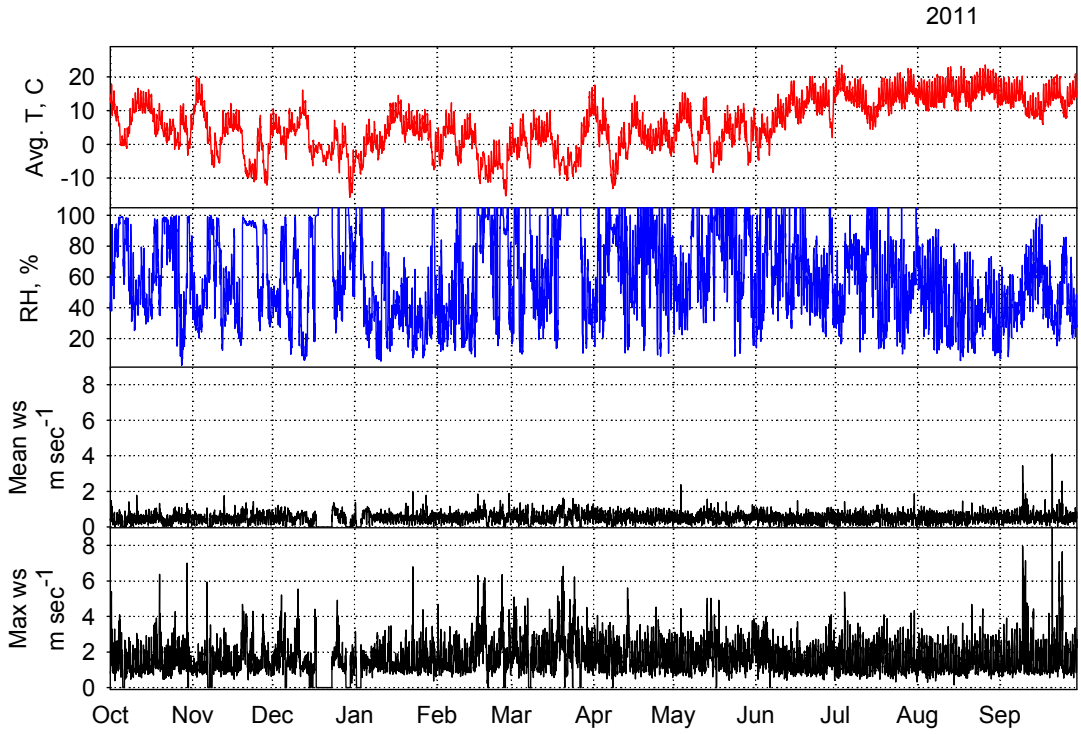

Figure B10. 2011 hourly averages of: mean air temperature, relative humidity, mean wind speed, and maximum wind speed from the Panther Meadow meteorologic station.

APPENDIX C

INFLUENCE OF CANOPY STRUCTURE AND DIRECT BEAM SOLAR IRRADIANCE ON SNOWMELT RATES IN A MIXED CONIFER FOREST

Keith N. Mussleman, Noah P. Molotch, Steven Margulis, Peter B. Kirchner, Roger C. Bales

Agricultural and Forest Meteorology 161 (2012) 46-56
doi: 10.1016/j.agformet.2012.03.011

The published journal article is available at: elsevier.com/locate/agformet

APPENDIX D

FOREST ALLIANCE CLASSIFICATION

Forest alliances used to determine dominant species forest type in chapter 2, adapted from USGS - NPS (2007)

Sierra Lodgepole Pine Forest Alliance (3020)

This forest alliance is mapped on a wide range of sites from gentle canyon bottoms to steep high slopes and ridges between 2028 -- 3523 m. Forests and woodlands included in this alliance are characterized by a closed to moderately open tree canopy that is dominated by *Pinus contorta var. murrayana*. *P. contorta ssp. murrayana* occupies a broad array of habitats in the Sierra Nevada, and this is reflected in the diverse range of associations it characterizes. Stands may be even- or multi-aged depending on geographic location, edaphic characteristics, and local fire history. Shrub and herbaceous layers may be present or absent depending on tree canopy characteristics and local site conditions. Stands are characterized by upland, palustrine, and seasonally flooded hydrology. Soils are well drained sands, loams, and sandy loams.

Ponderosa Pine Forest Alliance (3050)

This forest alliance is mapped on gentle to steep primarily south to southwest-facing slopes between 1165 -- 2125 m. The open tree canopy is often dominated by *Pinus ponderosa*, with *Abies concolor, P. lambertiana, Quercus chrysolepis, and Q. kelloggii* often occurring as co-dominants and *Calocedrus decurrens* sometimes contributing low

cover. The shrub layer can be sparse or dense and may contain *Arctostaphylos patula, A. viscida, Ceanothus cordulatus, C. integerrimus var. californicus, Chamaebatia foliolosa,* and/or *Chrysolepis sempervirens* as
important species. The herbaceous layer is characteristically sparse. The hydrology is upland. Soils are well drained sandy loams.

Giant Sequoia Forest Alliance (4020)

This forest alliance is mapped on gentle to steep slopes of varying aspect between 1371 -- 2426 m on the western slope of the Great Western Divide. The tree canopy is dominated by a mixture of montane conifers, including *Abies concolor, Calocedrus decurrens,* and *Pinus lambertiana,* which provide a matrix within which *Sequoiadendron giganteum* provides an important component. A secondary layer of *Cornus nuttallii* is frequently present. The shrub layer is generally open and contains scattered patches of *Ceanothus integerrimus, Chrysolepis sempervirens, Corylus cornuta var. californica,* and young conifers. The herbaceous layer is generally sparse but can be locally well developed depending on microsite characteristics; it frequently includes *Adenocaulon bicolor, Draperia systyla, Galium spp., Lupinus polyphyllus var. burkei,* and *Pteridium aquilinum.* The hydrology is upland. Soils are moderately well drained sandy loams.

California Red Fir Forest Alliance (4050)

This forest alliance is mapped on gentle to steep slopes of varying aspect between 2003 -- 3275 m. The tree canopy of associations in this upper montane alliance is dominated by *Abies magnifica*. Other trees in the canopy may include *A. concolor, Pinus contorta var.*

murrayana, P. jeffreyi, P. lambertiana, and *P. monticola*. The shrub layer ranges from absent to well developed, and most frequently includes *Acer glabrum, Arctostaphylos nevadensis, A. patula, Artemisia tridentata, Ceanothus cordulatus, Chrysolepis sempervirens, Holodiscus discolor, Ledum glandulosum, Phyllodoce breweri, Prunus emarginata, Ribes spp.,* or *Symphoricarpos mollis*. The herbaceous layer is characteristically sparse to absent, with *Apocynum androsaemifolium, Arabis spp., Aster breweri, Carex rossii, Elymus elymoides, Hieracium albiflorum, Lupinus latifolius var. columbianus, Monardella odoratissima, Pedicularis semibarbata, Pteridium aquilinum, Pyrola picta*, and *Senecio triangularis* among the most frequently encountered species. The hydrology is upland. Soils are moderately well drained to well drained sandy loams.

California Red Fir-White Fir Forest Alliance (4070)

This forest alliance is mapped on gentle to steep slopes of varying aspect between 1703 -- 3077 m. The tree canopy of associations in this montane alliance is dominated by a mixture of *Abies magnifica* and *A. concolor*. Other trees in the canopy may include *Juniperus occidentalis var. australis, Pinus contorta var. murrayana, P. jeffreyi, P. lambertiana,* and *P. monticola*. The shrub layer ranges from absent to well developed, and most frequently includes *Acer glabrum, Arctostaphylos patula, Ceanothus cordulatus, Chrysolepis sempervirens, Prunus emarginata, Ribes spp.,* or *Symphoricarpos spp.* The herbaceous layer is characteristically sparse to absent, with *Apocynum androsaemifolium, Arabis platysperma, Aster breweri, Elymus glaucus, Hieracium albiflorum, Lupinus spp., Monardella odoratissima, Pteridium aquilinum*, and

Pyrola picta among the most frequently encountered species. The hydrology is upland. Soils are well drained sandy loams.

White Fir-Sugar Pine Forest Alliance (4080)

This forest alliance is mapped on gentle to steep slopes of varying aspect between 1109 -- 2897 m. This forest alliance includes some of the most extensive montane forests mapped in the two parks, including stands of what is frequently referred to as the 'mixed conifer' forest. The tree canopy is dominated by a mixture of *Abies concolor* and *Pinus lambertiana*, with *Calodedrus decurrens* important on lower elevation sites. Other trees in the canopy frequently include *P. jeffreyi, P. ponderosa*, and/or *Quercus kelloggii; P. contorta var. murrayana* may also occur in colder air drainages. The shrub layer is dominated by regeneration of the coniferous overstory and may also contain *Arctostaphylos patula, Ceanothus cordulatus, Chamaebatia foliolosa, Chrysolepis sempervirens, Cornus nuttallii, Corylus cornuta var. californica, Prunusemarginata,* or *Ribes spp*. depending on site conditions. The herbaceous layer is characteristically sparse, but frequently includes *Adenocaulon bicolor, Apocynum androsaemifolium, Draperia systyla, Galium sparsiflorum, Hieracium albiflorum,* and/or *Pteridium aquilinum* in addition to young conifer seedlings. The hydrology is upland. Soils are well drained sandy loams.

Western White Pine-Sierra Lodgepole Pine (4540)

This forest mapping unit is an aggregation of the *Pinus monticola - Pinus contorta var. murrayana* woodland association (3132) and the *Abies magnifica-Pinus monticola-Pinus contorta var. murrayana* woodland association (4055). The aggregated mapping unit is

mapped on gentle to steep slopes of varying aspect between 2383 -- 3278 m. The open to moderately dense tree canopy is dominated by a mixture of *Pinus monticola* and *P. contorta var. murrayana*, with *Abies magnifica* important in lower elevation stands. *P. albicaulis,* and *P. balfouriana ssp. austrina* are also often present at low cover. The shrub layer is absent to well developed; when present, it is frequently dominated by *Arctostaphylos nevadensis A. patula, Chrysolepis sempervirens, ,* various *Ribes spp.* and/or *Holodiscus microphyllus.* The herbaceous layer is sparse to absent, with *Arabis spp., Aster breweri, Elymus elymoides, Pteridium aquilinum, Carex exserta, C. rossii, Juncus parryi* and *Senecio triangularis* most common. The hydrology is upland. Soils are well drained sands or sandy loams.

Reference

USGS-NPS. 2007. Vegetation mapping program. Sequoia and Kings Canyon National Parks, Three Rivers, California.

http://science.nature.nps.gov/im/inventory/veg/docs/Veg_Inv_12step_Guidance_v1.1.pdf

APPENDIX E

SOIL MOISTURE RESPONSE TO SNOWMELT AND RAINFALL IN A SIERRA NEVADA MIXED-CONIFER FOREST

Roger C. Bales, Jan W. Hopmans, Anthony T. O'Geen, Mathew Meadows, Peter C. Hartsough, Peter Kirchner, Carolyn T. Hunsaker, Dylan Beaudette

Vadose Zone Journal, Vol. 10:786-799 (2011)

doi: 10.2136/vzj.2011.0001

The published journal article is available at: VadoseZoneJournal.org

APPENDIX F

WOLVERTON BASIN SOIL MOISTURE DATA

Volumetric water content data collected with the Wolverton Basin Critical Zone Observatory. Metadata, raw data and higher level data can be found at:
https://eng.ucmerced.edu/snsjho/files/MHWG/Field/SEKI/Wolverton
or by contacting the author.

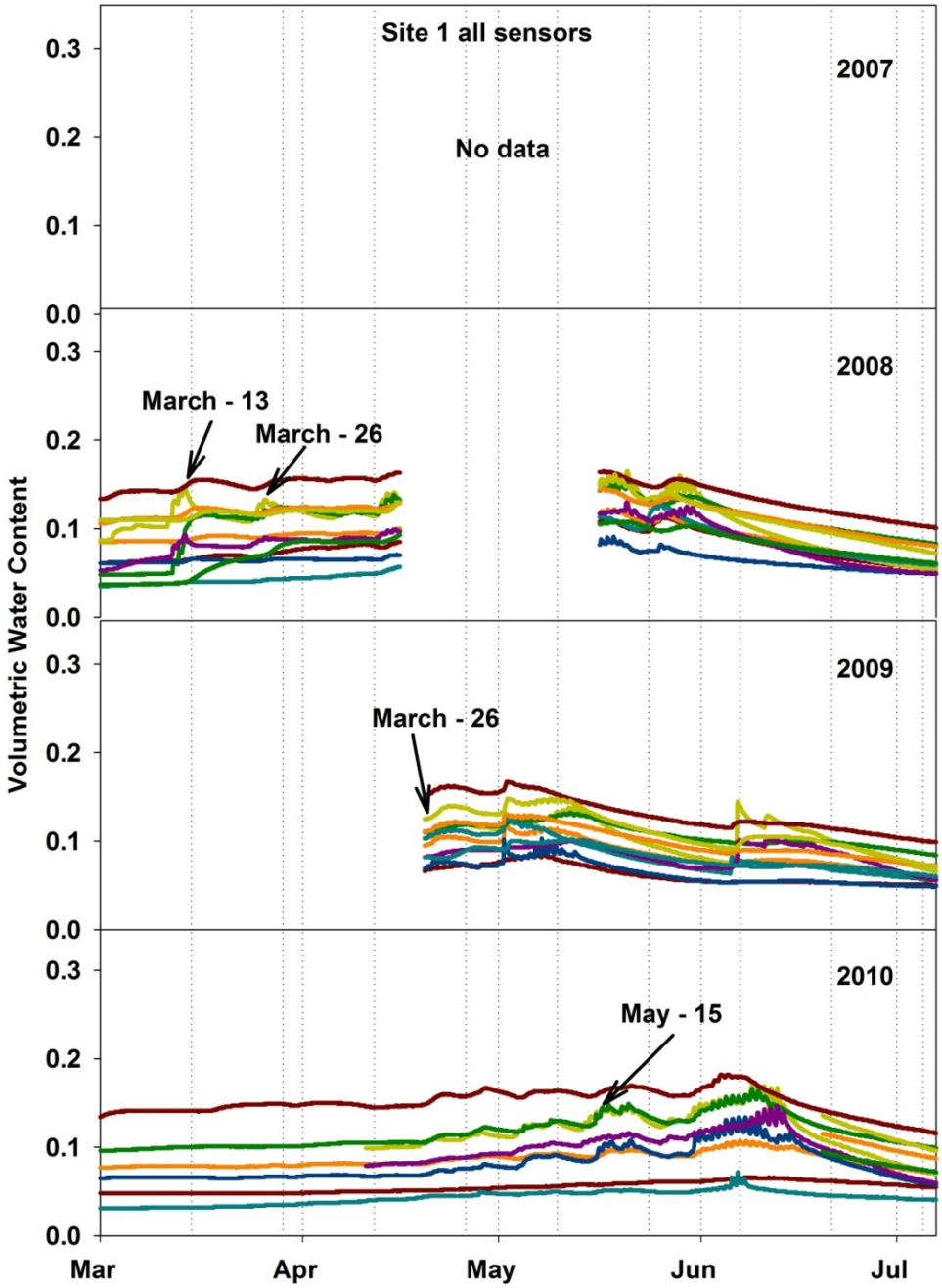

Figure F1. All sensor soil moisture over four annual melt seasons from low elevation north-facing site-1 sensor-cluster.

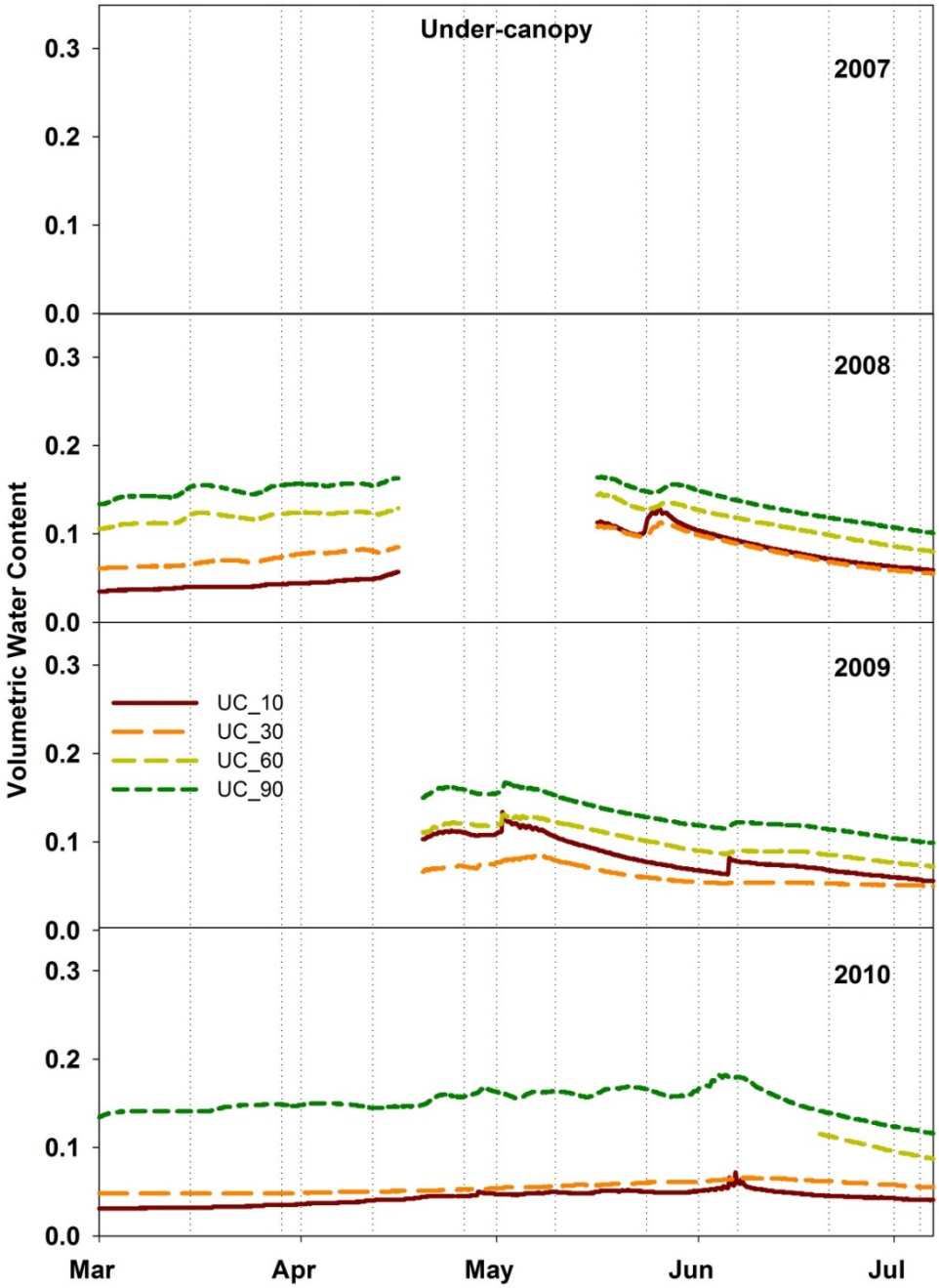

Figure F2. Open soil moisture over four annual melt seasons from low elevation north-facing site-1 sensor-cluster.

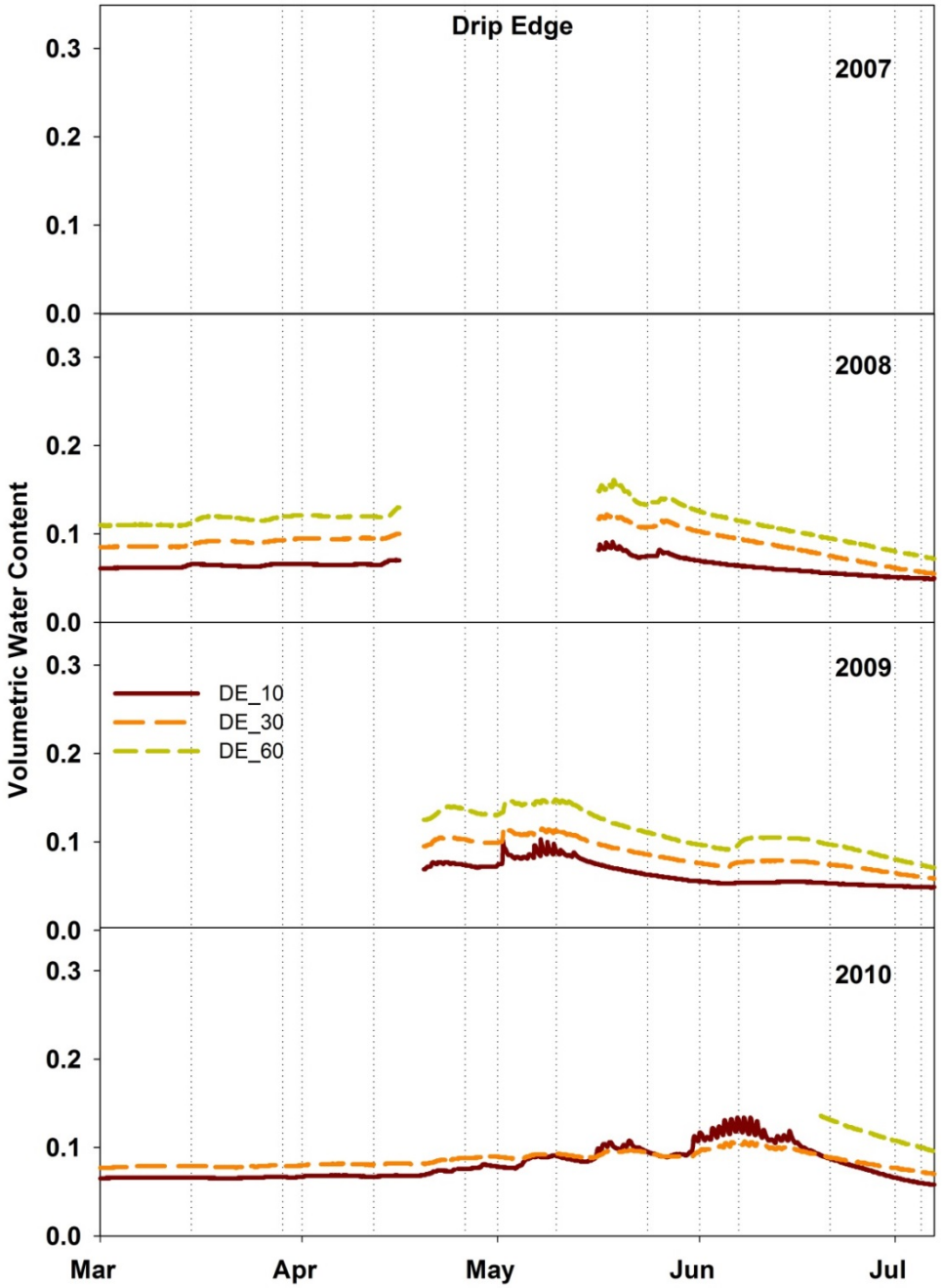

Figure F3. Drip-edge soil moisture over four annual melt seasons from low elevation north-facing site-1 sensor-cluster.

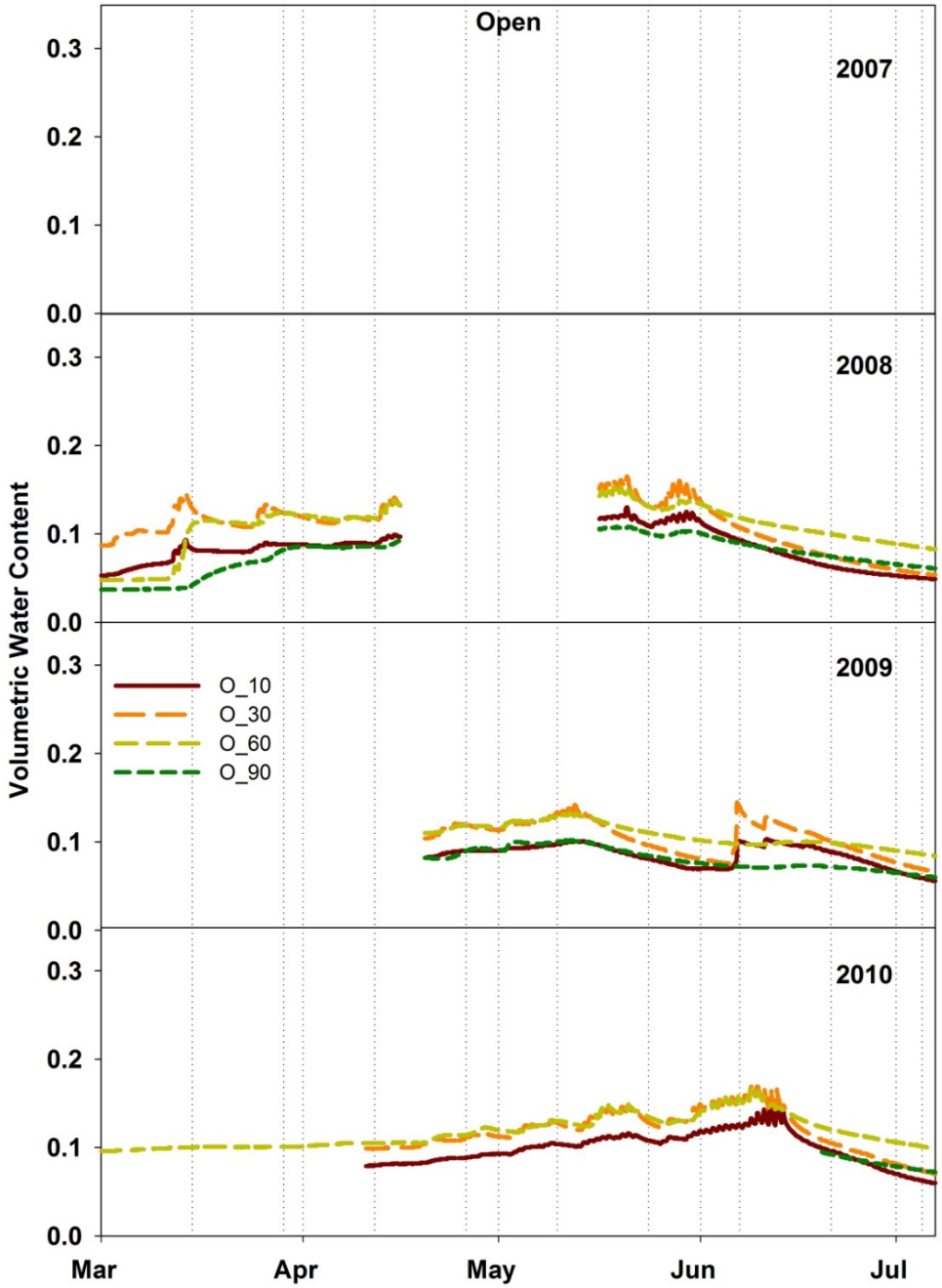

Figure F4. Under-canopy soil moisture over four annual melt seasons from low elevation north-facing site-1 sensor-cluster.

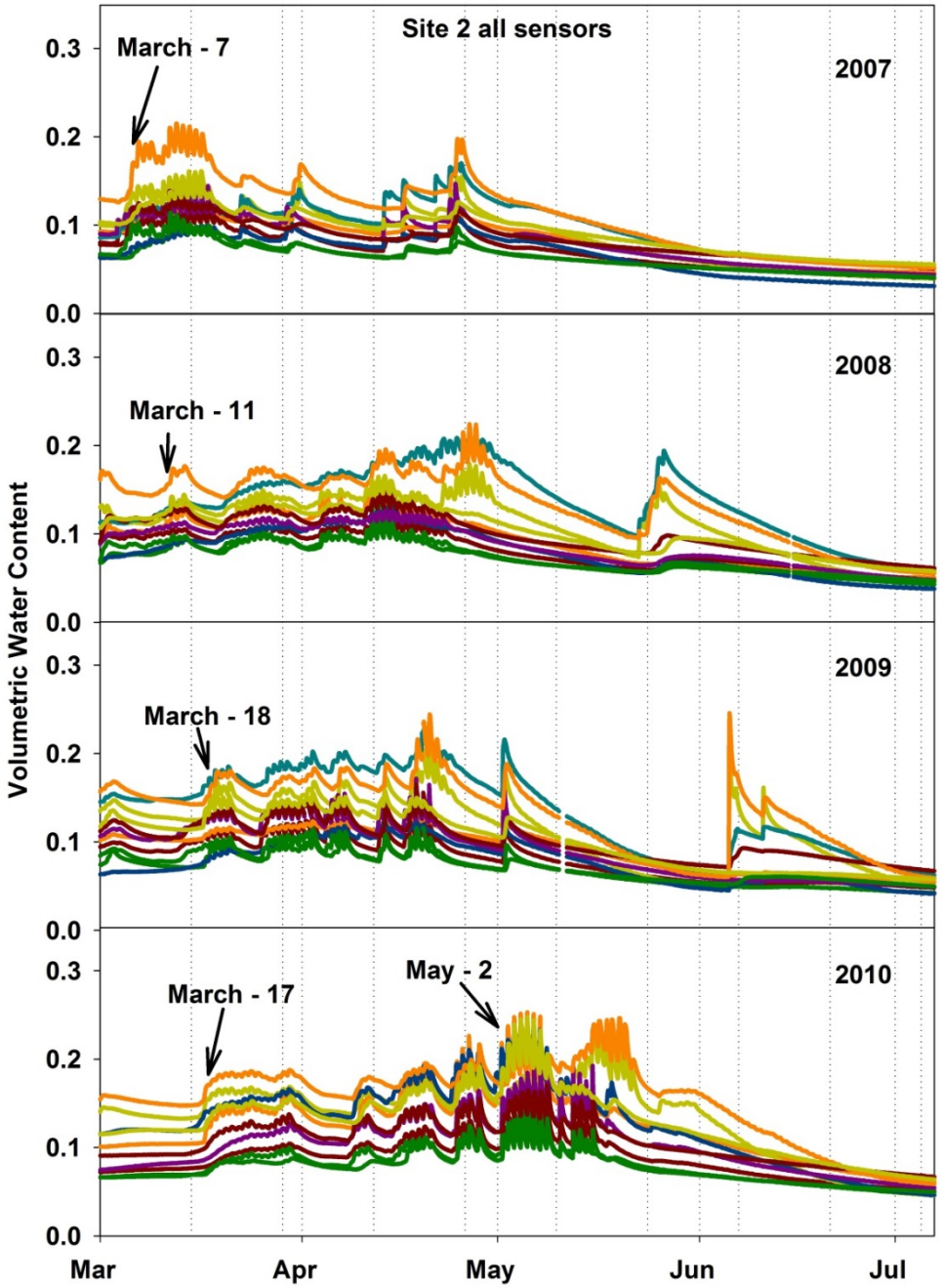

Figure F5. All sensor soil moisture over four annual melt seasons from low elevation southeast-facing site-2 sensor-cluster.

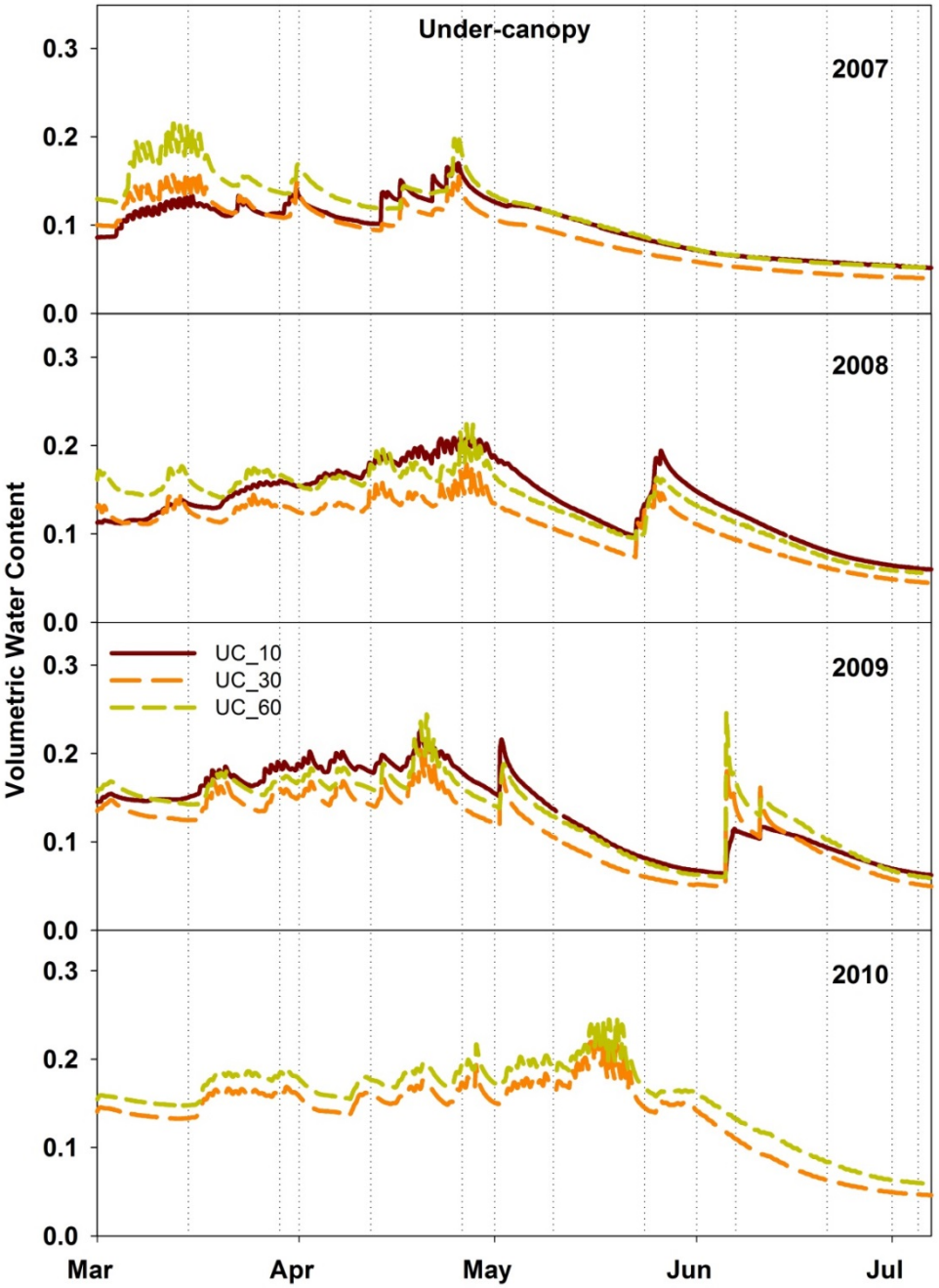

Figure F6. Open soil moisture over four annual melt seasons from low elevation southeast-facing site-2 sensor-cluster.

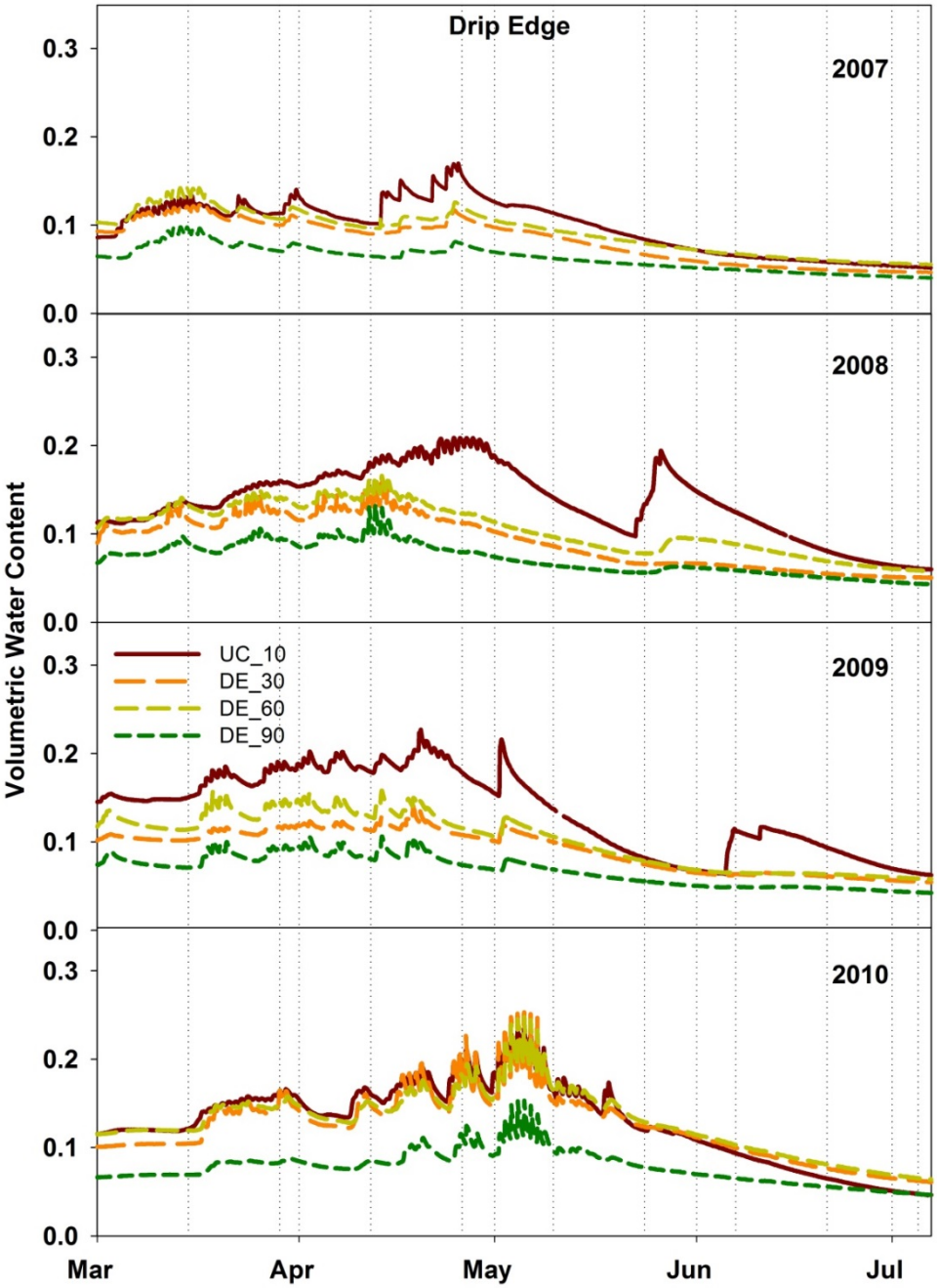

Figure F7. Drip-edge soil moisture over four annual melt seasons from low elevation southeast-facing site-2 sensor-cluster.

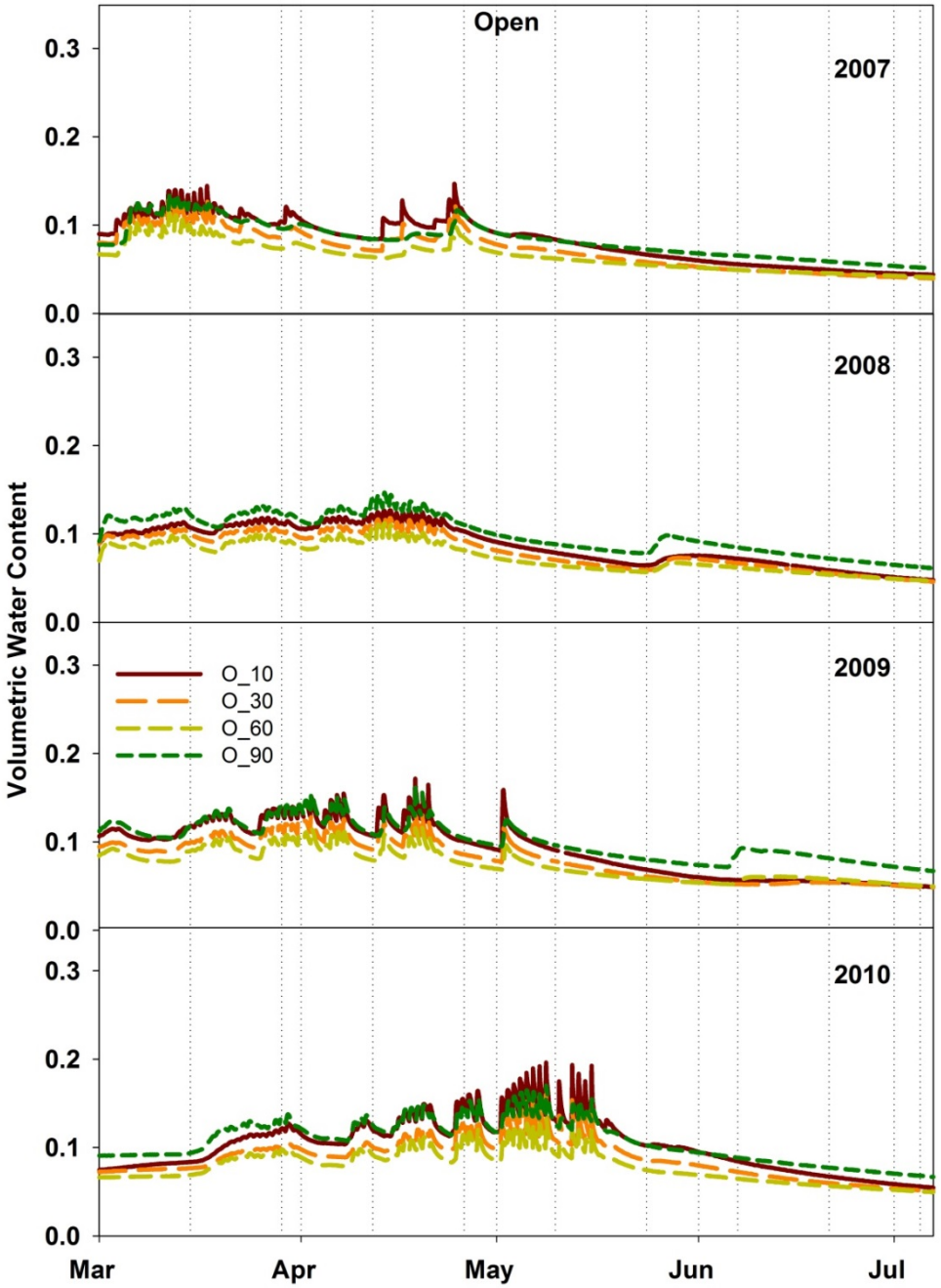

Figure F8. Under-canopy soil moisture over four annual melt seasons from low elevation southeast-facing site-2 sensor-cluster.

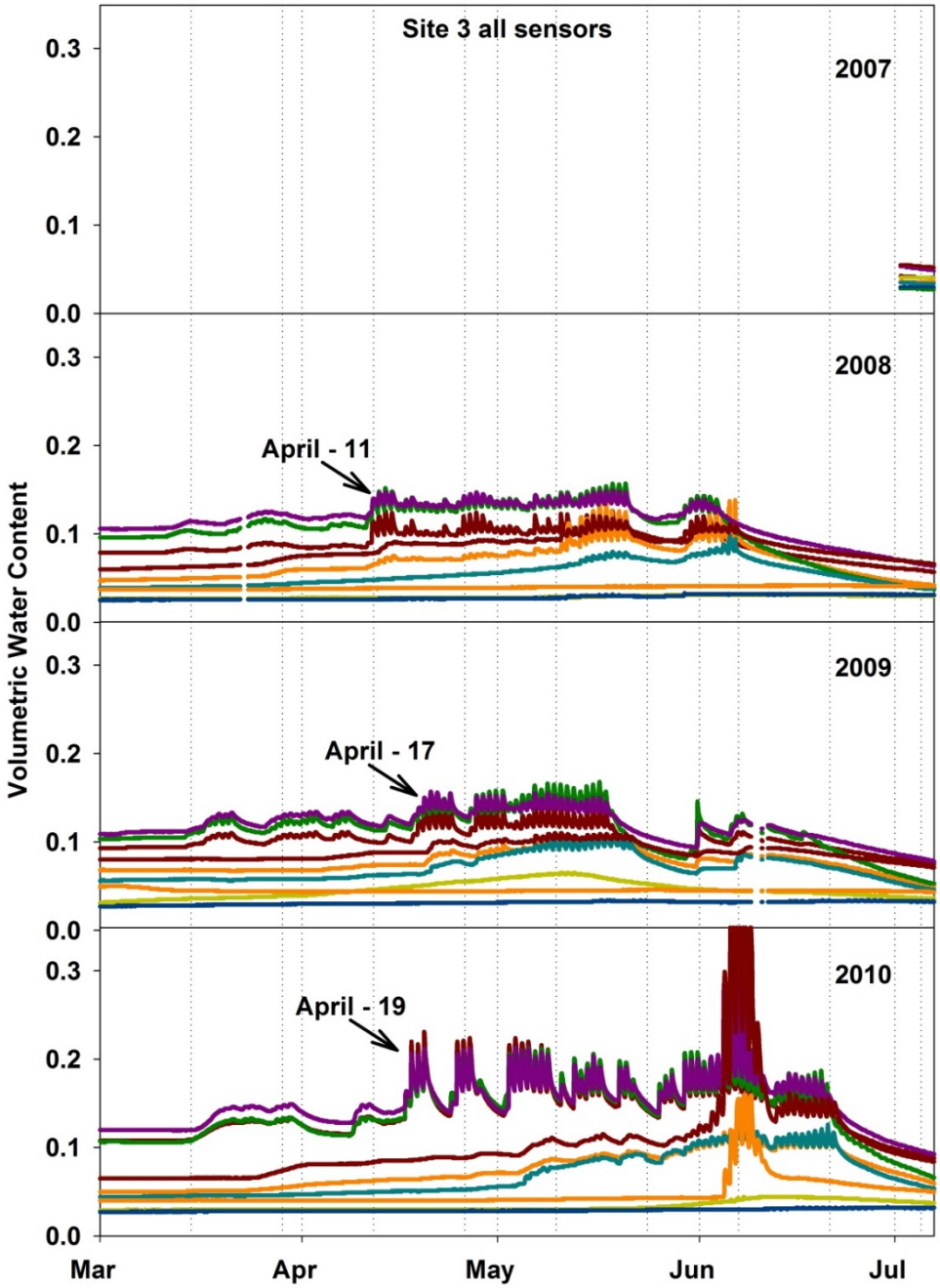

Figure F9. All sensor soil moisture over four annual melt seasons from high elevation southeast-facing site-3 sensor-cluster.

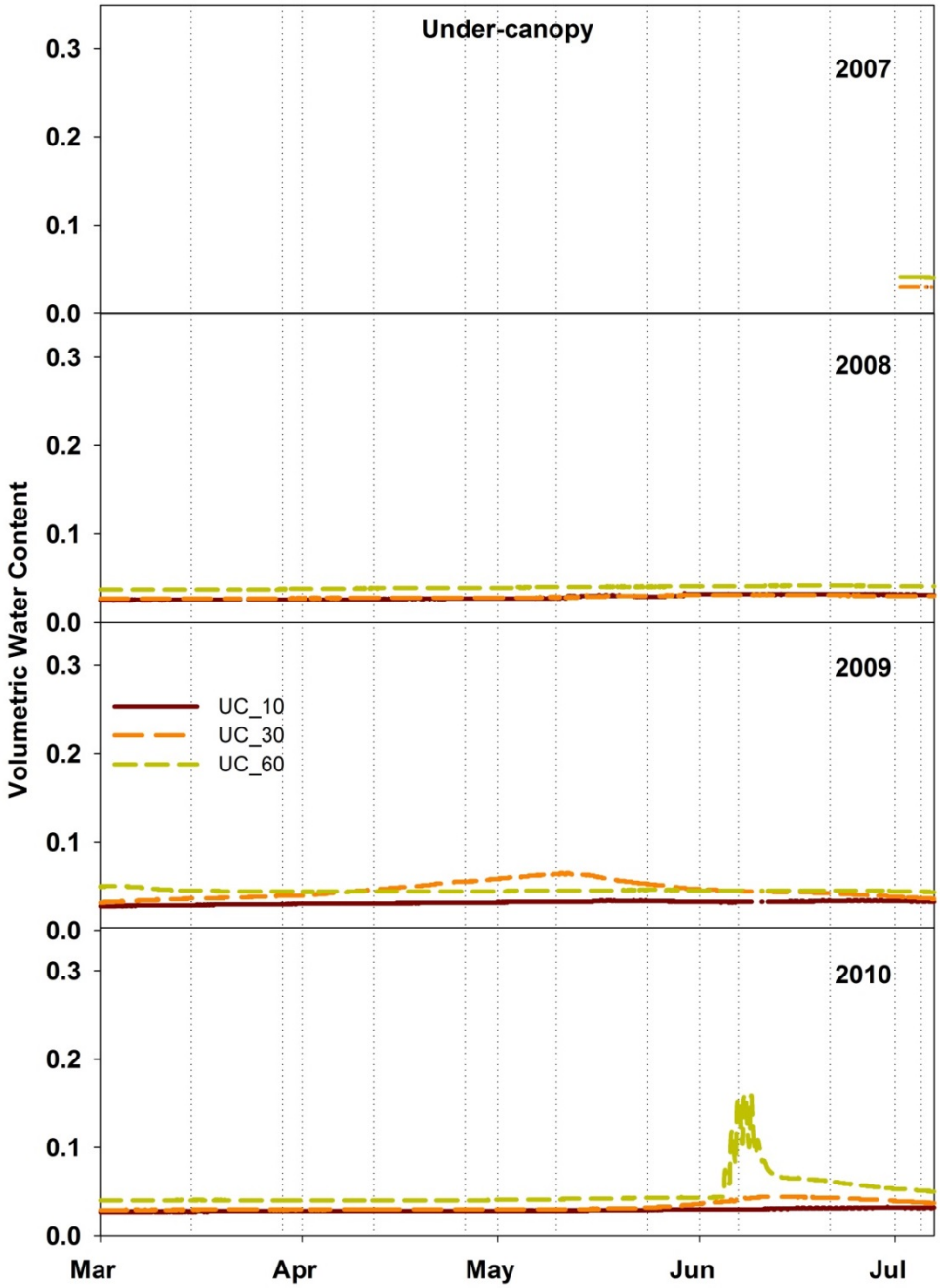

Figure F10. Open soil moisture over four annual melt seasons from high elevation southeast-facing site-3 sensor-cluster.

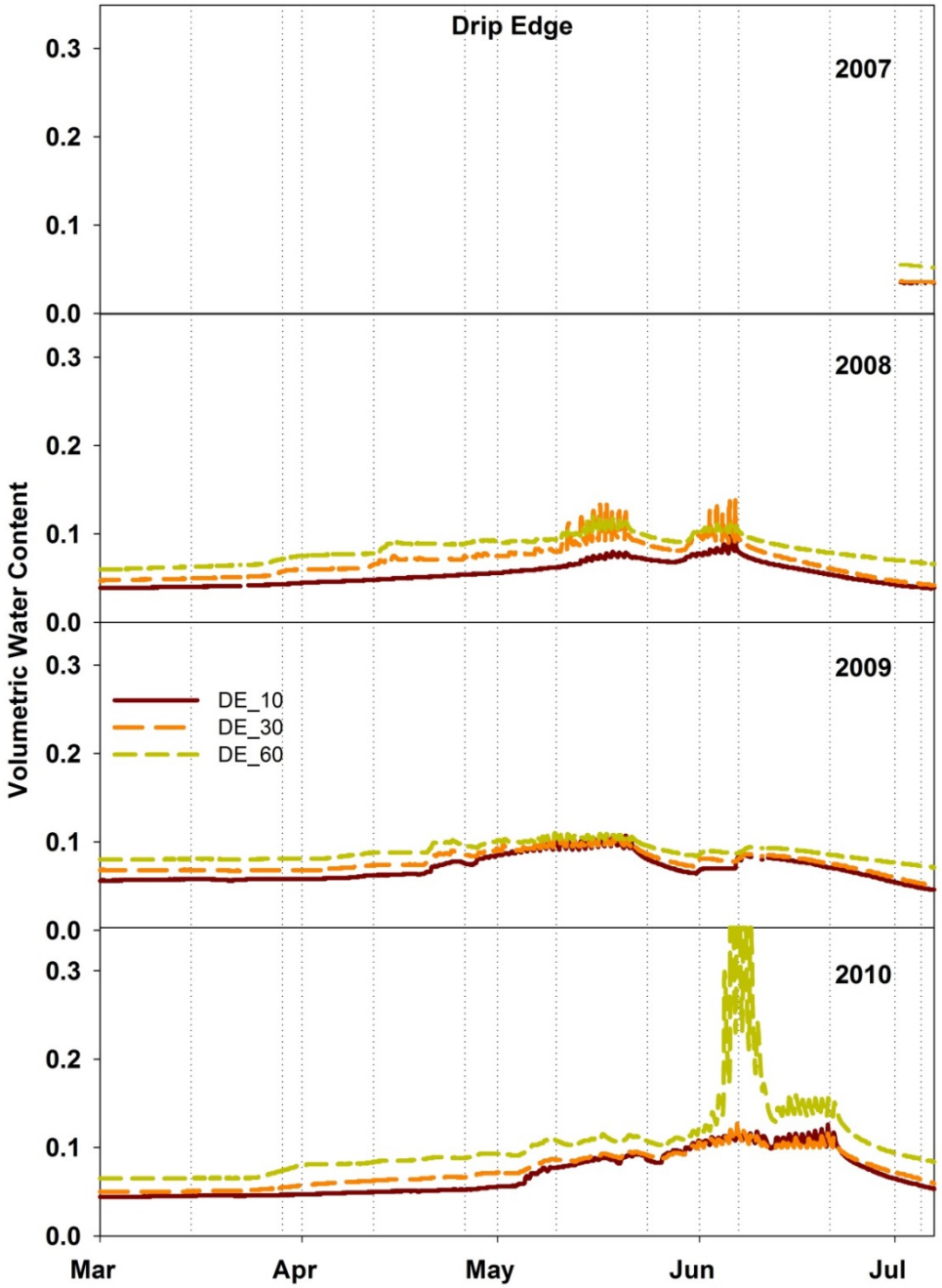

Figure F11. Drip-edge soil moisture over four annual melt seasons from high elevation southeast-facing site-3 sensor-cluster.

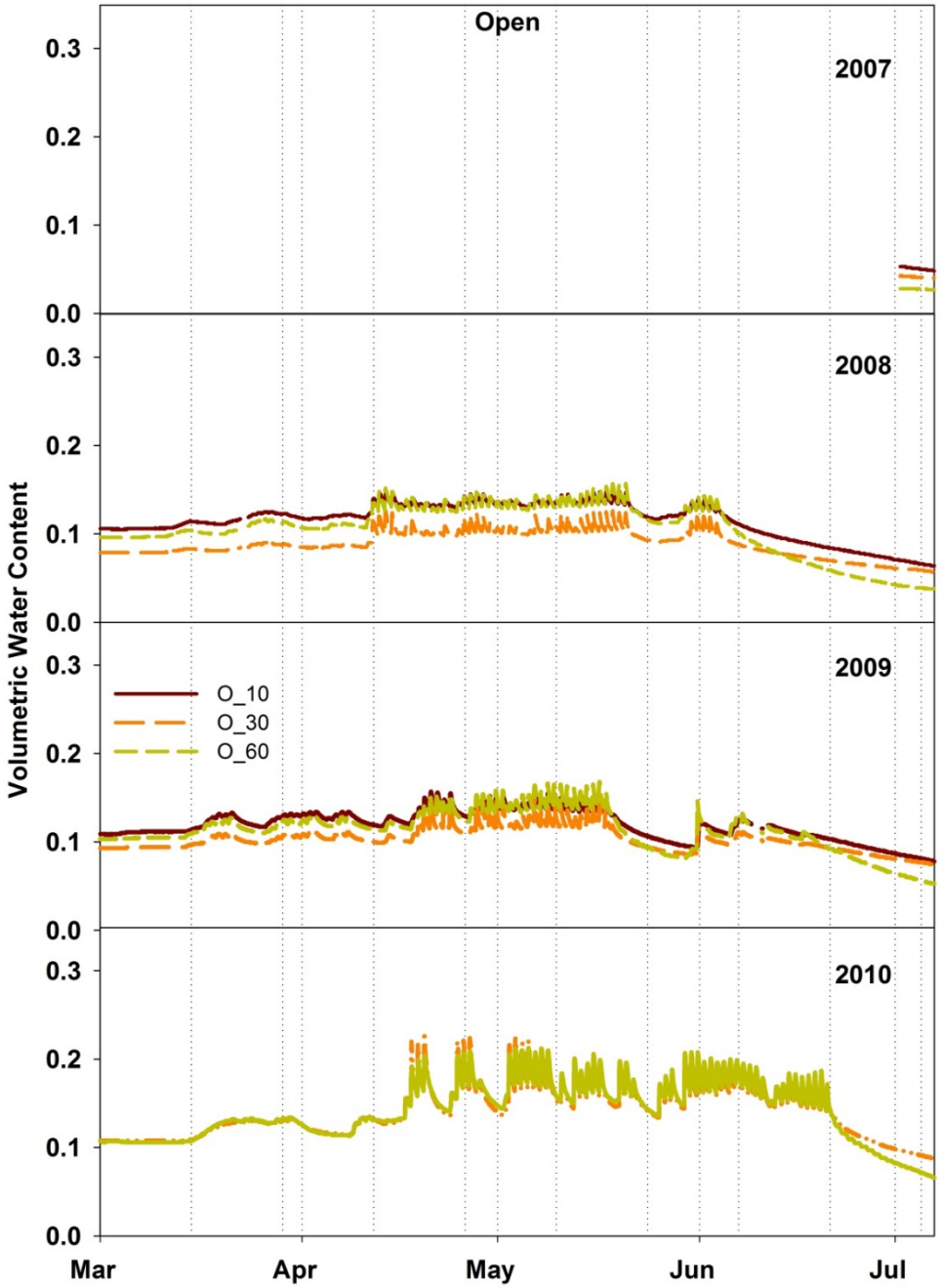

Figure F12. Under-canopy soil moisture over four annual melt seasons from high elevation southeast-facing site-3 sensor-cluster.

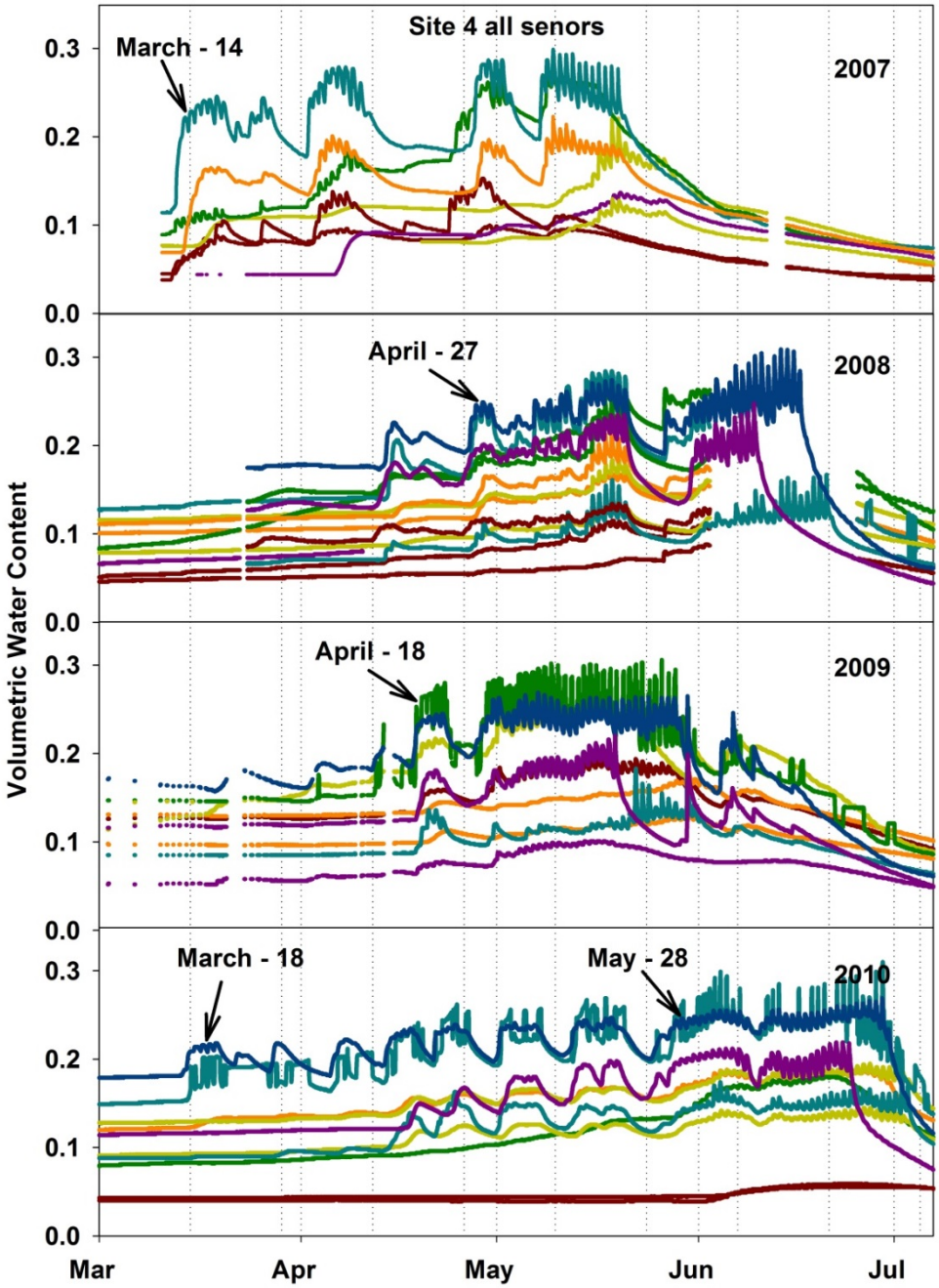

Figure F13. All sensor soil moisture over four annual melt seasons from high elevation north-facing site-4 sensor-cluster.

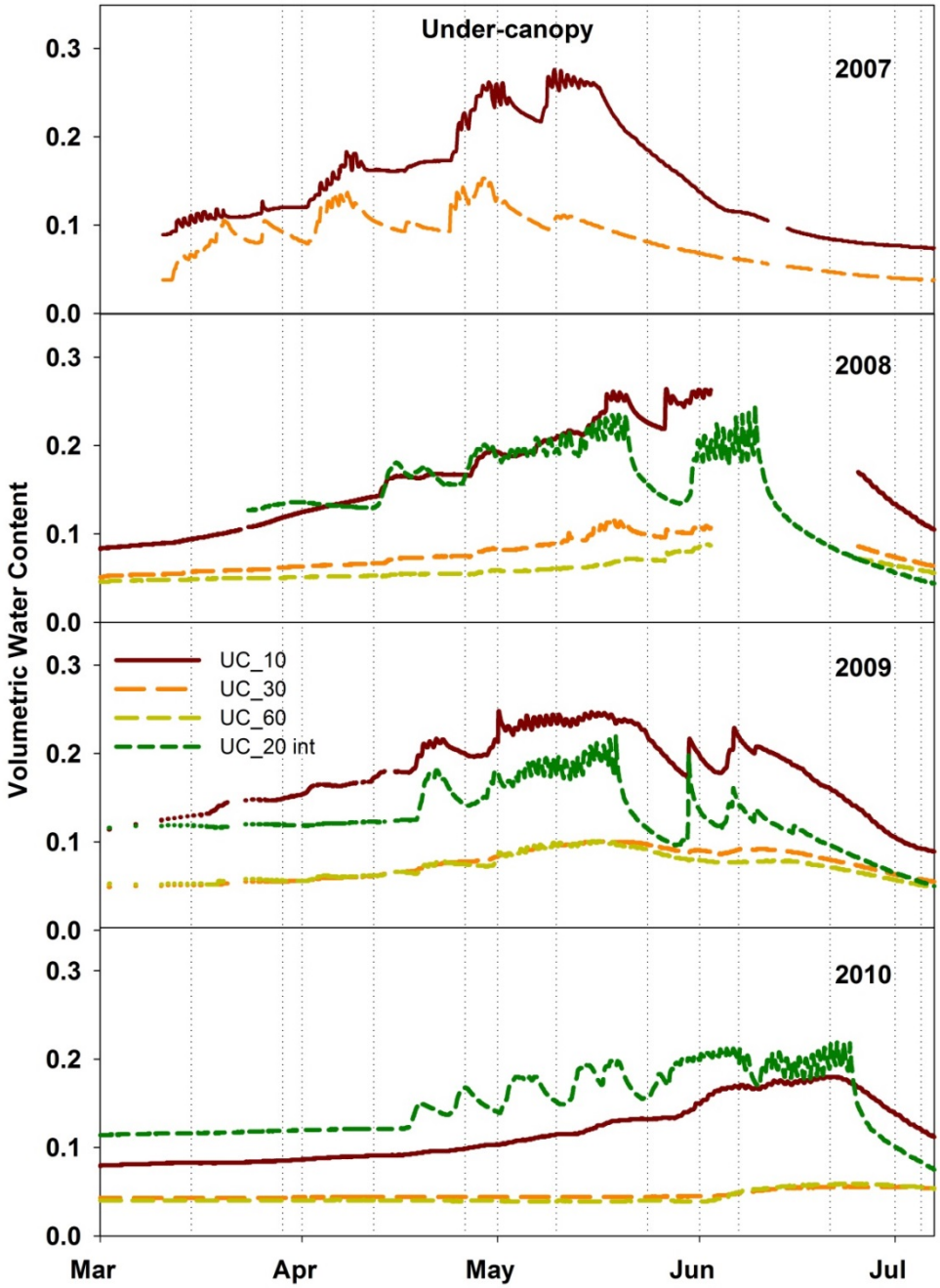

Figure F14. Open soil moisture over four annual melt seasons from high elevation north-facing site-4 sensor-cluster.

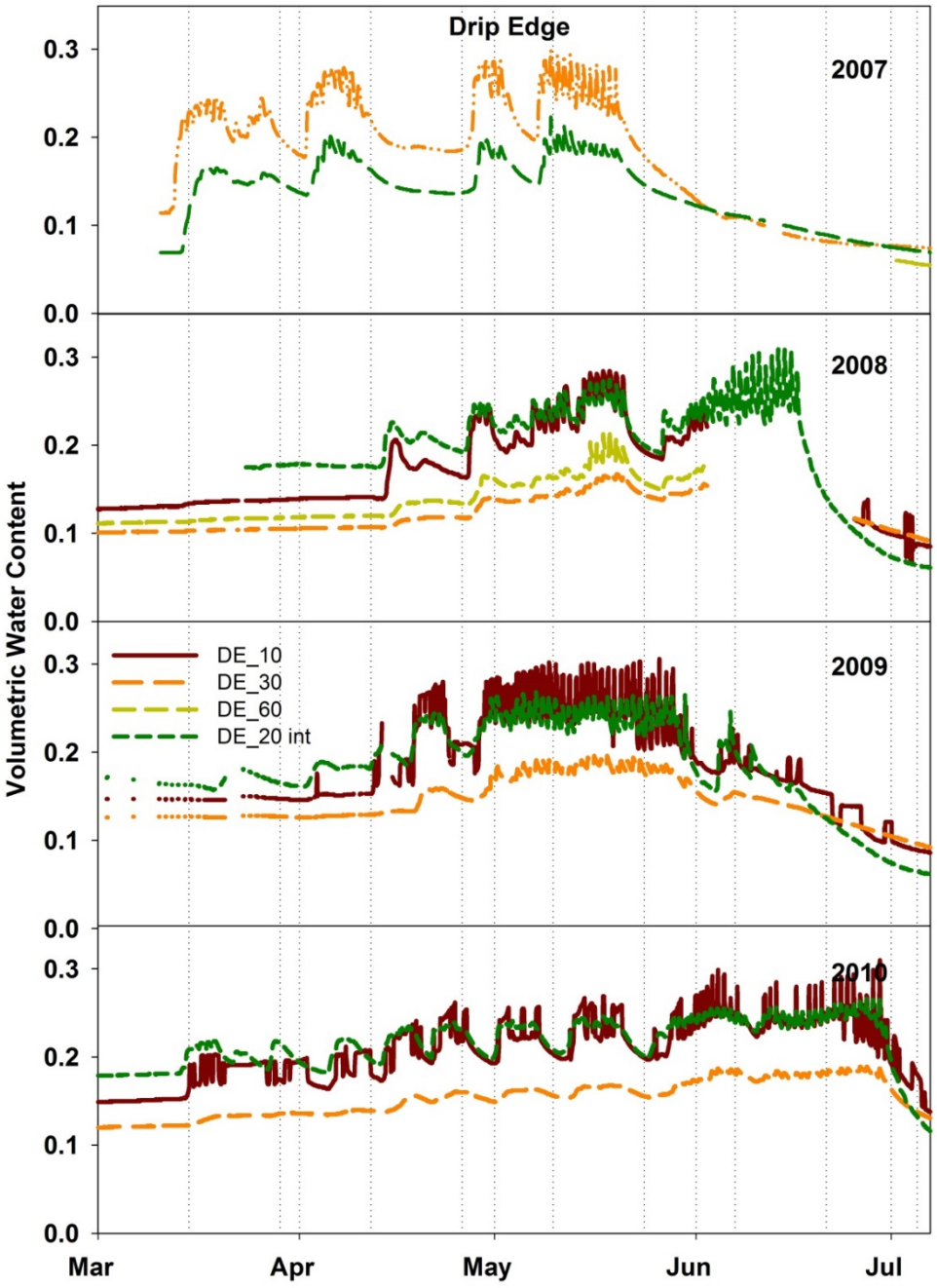

Figure F15. Drip-edge soil moisture over four annual melt seasons from high elevation north-facing site-4 sensor-cluster.

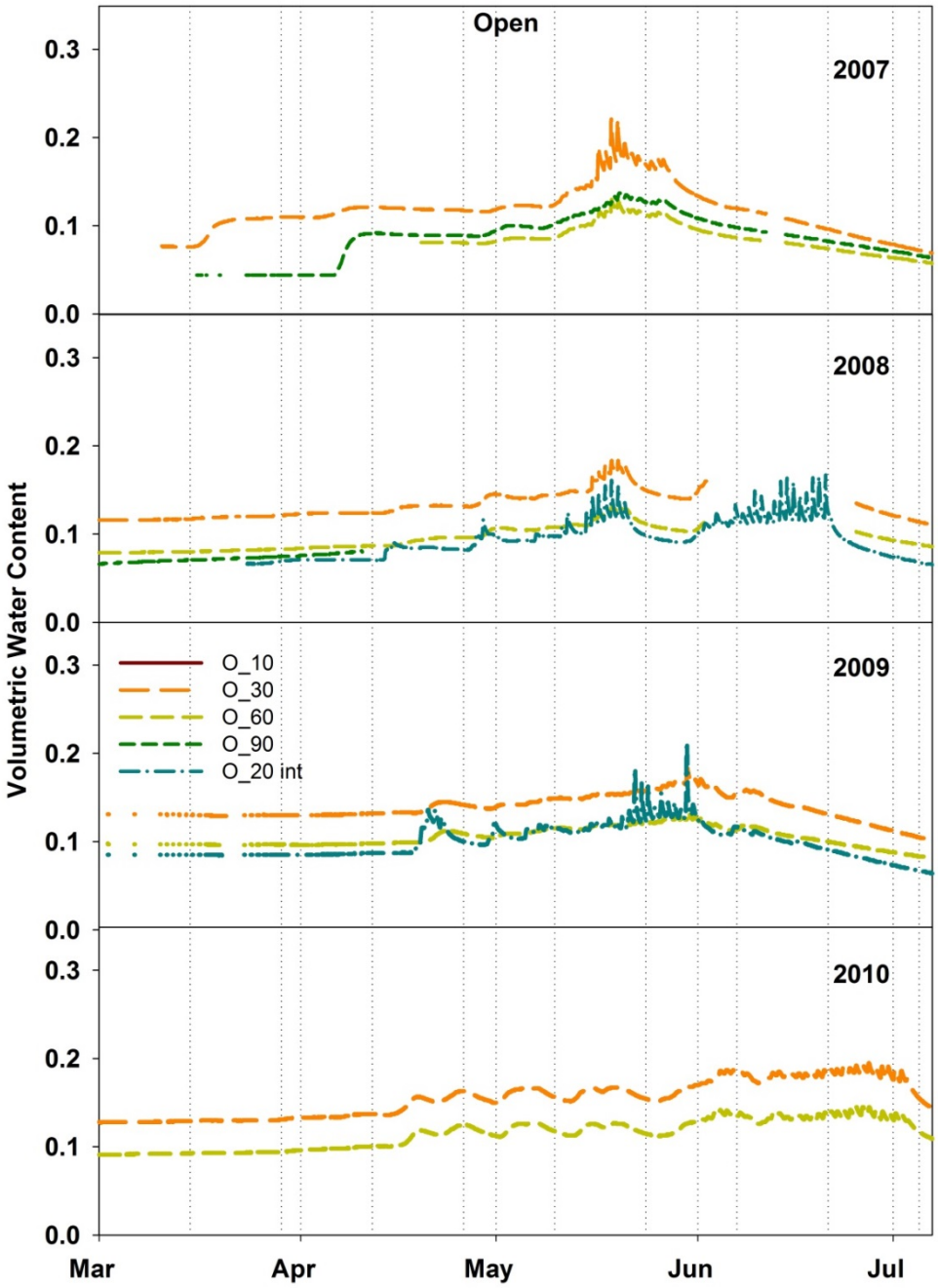

Figure F16. Under-canopy soil moisture over four annual melt seasons from high elevation north-facing site-4 sensor-cluster.